



AMERICAN UNIVERSITY OF BEIRUT

POLYMERIC NANOMATERIALS FOR  
FLUORESCENT-BASED THERMAL SENSING AND  
CONTROLLED DRUG DELIVERY

by  
SARRIAH ALI HASSOUN

A project  
submitted in partial fulfillment of the requirements  
for the degree of Master of Science  
to the Department of Chemistry  
of the Faculty of Arts and Sciences  
at the American University of Beirut

Beirut, Lebanon  
February 2021

AMERICAN UNIVERSITY OF BEIRUT

POLYMERIC NANOMATERIALS FOR  
FLUORESCENT-BASED THERMAL SENSING AND  
CONTROLLED DRUG DELIVERY

by  
SARRIAH ALI HASSOUN

Approved by:

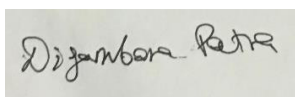


[Signature]

---

Dr. Pierre Karam, Associate Professor  
Chemistry

Advisor

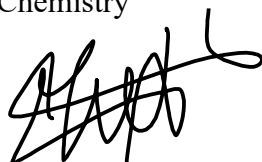


[Signature]

---

Dr. Digambara Patra, Full Professor  
Chemistry

Member of Committee



[Signature]

---

Dr. Mohamad Hmadeh, Associate Professor  
Chemistry

Member of Committee

Date of thesis defense: February 11, 2021

# AMERICAN UNIVERSITY OF BEIRUT

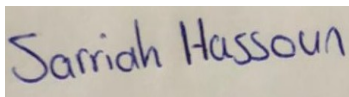
## PROJECT RELEASE FORM

Student Name:

\_\_\_\_\_ HASSOUN \_\_\_\_\_ SARRIAH \_\_\_\_\_ ALI \_\_\_\_\_  
Last First Middle

I authorize the American University of Beirut, to: (a) reproduce hard or electronic copies of my project; (b) include such copies in the archives and digital repositories of the University; and (c) make freely available such copies to third parties for research or educational purposes:

- As of the date of submission
- One year from the date of submission of my project.
- Two years from the date of submission of my project.
- Three years from the date of submission of my project.



February 22, 2021

---

Signature

Date

## ACKNOWLEDGEMENTS

I would like to express my gratitude to my advisor Dr. Pierre Karam for imparting his knowledge and expertise in this study.

I thank the committee members Dr. Patra and Dr. Hmadeh for their huge efforts and highly appreciable feedbacks.

I am overwhelmed in all humbleness and gratefulness to acknowledge my debt to all those who have helped me to finish this exhausting work, especially my friends, Tamara Abou Matar, Rida Farhat, Nisrine Assaad, Denise Rueegger, and Ali Shamseddine. This journey wouldn't have been possible without their support. I'm really blessed to have them in my life.

I acknowledge the technical support and overall help of the CRSL team, Ms. Rania Shatila, Mr. Joan Younes, and Mr. Chady Assaf, and technician Mr. Simon Al-Ghawi.

I would like to express my greatest gratitude to Dr. Samira Korfali for her continuous support and encouragement throughout the years.

Finally, to my caring, loving, and supportive family, your encouragement when the times got rough are much appreciated. This work is wholeheartedly dedicated to my mother who has been a source of inspiration and gave me strength when I thought of giving up.

# ABSTRACT OF THE THESIS OF

Sarriah Ali Hassoun

for

Master of Science

Major: Chemistry

Title: Polymeric Nanomaterials for Fluorescent-Based Thermal Sensing and Controlled Drug Delivery

Temperature is a critical parameter that controls many physical and chemical phenomena in various fields. Nonetheless its importance, we still lack a powerful tool to accurately measure its variations at the nano-scale. In this work we aim to develop fluorescent based thermal probes to map temperature in lipid membranes and thin polymer films. As well, we aim to take advantage of the thermal sensitivity of a polymeric material to develop a controlled drug delivery system. Subsequently, temperature variations at the nanoscale when the drug is being released can be studied with high spatial resolution using the thermal probe. In turn, this will help in unraveling the underlying mechanisms related to drug delivery at the nanoscale level.

In the first project, we report the development of a ratiometric thermal fluorescent probe. This probe is based on the Förster resonance energy transfer (FRET) between a lipid-embedded conjugated polyelectrolyte and a lyophilic acceptor dye. The probe showed a thermal response within the body physiological temperature. The FRET pair was stable under multiple cycling and pH variations.

In the second project we report on the ratiometric thermal sensitivity of conjugated polyelectrolyte based thermal probe when complexed with PVP copolymers (co-vinyl acetate (VA) and co-polystyrene (PS)) in solution. The thermal sensitivity was then assessed when the mixture was spin coated on quartz slides and mixed with Rhodamine B. The signal was quantified with the change in temperature using a DSLR camera.

In the third project we took advantage of the thermal sensitivity of a hydrogel to develop magnetic agarose nanocarriers for controlled curcumin release. In this work the heat generated on the MNP surface is degrading the agarose polymeric network along with mechanical deformation caused by the MNP vibrations when subjected to an alternating magnetic

# TABLE OF CONTENTS

ACKNOWLEDGEMENTS.....	1
ABSTRACT .....	2
ILLUSTRATIONS .....	7
TABLES .....	11
1. INTRODUCTION .....	12
1.1 Importance of Thermal Mapping.....	13
1.1.2 Conventional Thermometry Limitations .....	15
1.2 Fluorescent-based Nano-thermometry .....	15
1.2.1 Förster Resonance Energy Transfer .....	16
1.2.2 Limitations.....	19
1.3 Conjugated polyelectrolytes .....	19
1.3.1 Conjugated Polyelectrolyte Biocompatibility .....	20
1.3.2 Conjugated polyelectrolyte sensing mechanisms .....	21
1.4 Role of Temperature at the cellular level. ....	22
1.4.1 Role of temperature in drug delivery.....	23
1.5 Objectives.....	24
2. MATERIALS AND METHODS .....	26
2.1 Fluorescent Thermal Sensing using Conjugated Polyelectrolytes lipid membrane .....	26

2.1.1	Materials .....	26
2.1.2	Methods .....	26
2.2	Fluorescent Thermal Sensing using Conjugated Polyelectrolytes in Thin Polymer Films 28	
2.2.1	Materials .....	29
2.2.2	Methods .....	30
2.2.3	Solution Preparations.....	30
2.2.4	Characterization and Measurements.....	31
2.3	Magnetic Responsive Agarose nanoparticles as Potential Vehicles for Controlled Curcumin Release.....	34
2.3.1	Materials .....	34
2.3.2	Methods .....	34
3.	<b>FLUORESCENT-BASED THERMAL SENSING IN LIPID MEMBRANES.....</b>	<b>38</b>
3.1	Introduction .....	38
3.2	Results and Discussion .....	42
3.2.1	Thermal Sensing.....	42
3.2.2	Reversibility and Cycling .....	43
3.2.3	pH stability .....	43
3.2.4	Dynamic Light Scattering (DLS) .....	43
3.2.5	Förster Resonance Energy Transfer Pair .....	44
3.2.6	MPS-PPV thermal sensitivity.....	45
3.2.7	FRET-based Thermal Sensor .....	48
3.2.8	Thermal Response at Different Lipid Viscosities.....	52
3.2.9	MPS-PPV Signal Dependency on Membrane Positioning.....	57




3.2.10 Thermal Response Reversibility.....	57
3.2.11 pH stability of the Thermal Probe .....	58
3.3 Conclusion.....	62
<b>4. FLUORESCENT THERMAL SENSING USING CONJUGATED POLYELECTROLYTES IN THIN POLYMER FILMS .....</b>	<b>63</b>
4.1 Introduction .....	63
4.1.1 Polyvinylpyrrolidone (PVP).....	66
4.2 Thermal Sensing.....	69
4.3 Reversibility and Cycling .....	70
4.4 Results and Discussion.....	70
4.4.1 Absorbance Spectra.....	70
4.4.2 Titrations.....	71
4.4.3 Thermal Sensing.....	72
4.4.4 Relative Sensitivity.....	77
4.4.5 Reversibility and Cycling .....	79
4.4.6 Thin Polymer Film Assembly .....	81
4.5 Conclusion.....	87
<b>5. MAGNETIC RESPONSIVE AGAROSE NANOPARTICLES AS POTENTIAL VEHICLES FOR CONTROLLED CURCUMIN RELEASE .....</b>	<b>88</b>
5.1 Introduction .....	88
5.2 Results and Discussion.....	90
5.2.1 Dynamic Light Scattering (DLS) .....	90

5.2.2	Thermogravimetric Analysis (TGA) .....	91
5.2.3	Curcumin loading and release evaluation.....	92
5.2.4	Heating by induction versus heating in waterbath.....	94
5.2.5	Curcumin release using Higher MNP concentration.....	97
5.2.6	Microscopy Imaging.....	100
5.3	Conclusion.....	102
6.	CONCLUSION AND FUTURE WORK.....	103
7.	REFERENCES .....	105

# ILLUSTRATIONS

## Figure

- 1.1. Distance dependence of FRET efficiency. The Forster theory shows that efficiency  $E$  varies as the inverse sixth power of the distance between the two molecules (denoted by  $r$ ) (Reprinted with permission from Schlattner *et al*)... 17
- 1.2. Cell viability determined by CellTiter-Blue assay for PVP-55k, MPS-PPV, and MPS PPV/PVP-55k and at different concentrations of MPS-PPV (0.1X, 0.5X, 1X, 5X, and 10X) incubated for 4 h with HeLa and HEK cells. Data are expressed as percentage of fluorescence relative to controls (untreated cells). The error bars represent the standard deviation of three replicates. (Reprinted with permission from Abou Matar *et al*).....20
- 3.1. Chemical structures of Poly[5-methoxy-2-(3-sulfopropoxy)-1,4-phenylenevinylene] potassium salt solution (MPS-PPV), 1,1'-dioctadecyl-3,3,3',3'-tetramethylindodicarbocyanine perchlorate (DiD), and schematic representation of the FRET-based thermal probe.....42
- 3.2. Normalized absorbance of MPS-PPV and normalized fluorescent emission of DiD when embedded in a DPPC liposomes. Measurements were done in 10 mM HEPES buffer pH=7.3 and 150 mM NaCl and emission spectra were acquired upon excitation at 457nm.....44
- 3.3. (A) Fluorescence emissions of DPPC/MPS-PPV measured between 20.0 °C and 50.0 °C at a 5.0 °C increments. (B) Normalized integrated fluorescent intensity extracted from A at different temperatures. The lines connecting the experimental points are for visual aid. Measurements were done in 10 mM HEPES buffer pH=7.3 and 150 mM NaCl and emission spectra were acquired upon excitation at 457 nm.....45
- 3.4. (A) Fluorescence emission of DPPC-DiD/MPS-PPV between 20.0 and 50.0 °C n a 5.0 °C increments. (B) Calculated FRET at different temperature. The lines connecting the experimental points are for visual aid. Measurements were done in 10 mM HEPES buffer pH= 7.3 and 150 mM NaCl and emission spectra were acquired upon excitation at 457 nm.....46
- 3.5. (A) Thermal response of DiD embedded in DPPC between 20 and 50 °C. (B) Relative change in fluorescent emission for three trials. Lines connecting the experimentapoints are for visual aid only. Experiment was performed in 10 mM HEPES with 150 mM NaCl (pH= 7.3) buffer solution... 46
- 3.6. Fluorescence emissions of DOPC-DID/MPS-PPV between 20 and 50 °C in a 5 °C increments. Excitated at 457 nm and collected between 490 and 780 nm. Lines connecting the experimental points are for visual aid only. Experiment was

performed in 10 mM HEPES with 150 mM NaCl (pH= 7.3) buffer solution.....	53
3.7. Fluorescence emission of (A) DOPC/MPS-PPV and (B) DOPC/DiD between 20 and 50 °C. Measurements were done in 10 mM HEPES buffer pH= 7.3 and 150 mMNaCl.....	54
3.8. Calculated changes in FRET with increasing temperature as a function of cholesterol percentage in DPPC-DiD/MPS-PPV liposomes. Measurements were done in 10 mM HEPES buffer pH=7.3 and 150 mM NaCl and emission spectra were acquired upon excitation at 457nm. The lines connecting the experimental points are for visual aid.....	55
3.9. Calculated FRET 10 % Chol-DOPC and POPC and DOPC at different temperatures. Measurements were done in 10 mM HEPES buffer pH=7.3 and 150 mM NaCl and emission spectra were acquired upon excitation at 457 nm .....	57
3.10. Fluorescence enhancement of MPS-PPV upon the addition of preformed liposomes of DPPC and 20 % Chol-DPPC over time. At the 30 min mark, the solution was heated to 50.0 °C above the DPPC transition temperature.....	58
3.11. Reversibility of the calculated FRET signal upon heating DPPC-DiD/MPS-PPV liposomes between 20.0 °C and 50.0 °C. Measurements were done in 10 mM HEPES buffer pH= 7.3 and 150 mM NaCl and emission spectra were acquired upon excitation at 457 nm. The lines connecting the experimental points are for visual aid.....	59
3.12 (A) Thermal response of DPPC-DID/MPS-PPV at pHs 5.2, 7.3 and 9.0. (B) Emissions of MPS-PPV in basic (9.2), neutral (7.3) and acidic (5.0) mediums. Measurements were done in 10 mM HEPES buffer pH=7.3 and 150 mM NaCl and emission spectra were acquired upon excitation at 457 nm. The lines connecting the experimental points are for visual aid .....	61
4.1. Schematic representation of the chemical structure referring to the short anionic conjugated polyelectrolyte poly (phenylene ethynylene) carboxylate with 7 repeating monomer-units (PPE-CO <sub>2</sub> -7).....	66
4.2. Schematic representation of the complexation between PVP and PPE-CO <sub>2</sub> -7 (  ) at low and high temperature. (Reprinted with permission from <i>Ghenwa et al.</i> ) .....	68
4.3. Schematic and chemical structure of the amphiphilic polymers (A) poly(vinylpyrrolidone)-co-vinyl acetate (PVP-VA) and (B) polyvinylpyrrolidone polystyrene (PVP-PS).....	69
4.4. (A) Chemical Structures of poly (phenylene ethynylene) with 7 repeating units on average (PPE-CO <sub>2</sub> -7), poly(vinylpyrrolidone)-co-vinyl acetate (PVP-VA) and	

- poly(1-vinylpyrrolidone-co-styrene) (PVP-PS). (B) Absorbance spectra of PPE-CO<sub>2</sub>-7 (■), PPE-CO<sub>2</sub>-7/PVP-VA (●) and PPE-CO<sub>2</sub>-7/PVP-PS .....71
- 4.5. Fluorescent Emission Spectra of PPE-CO<sub>2</sub>-7 (5 μg/mL) upon addition of incremental amounts of (A) PVP-VA and (B) PVP-PS acquired at 20.0 °C in 10 mM HEPES and 150 mM NaCl when excited at 420 nm..... 73
- 4.6. (A) Thermal response of PPE-CO<sub>2</sub>-7 (5 μg/mL) in complexation with PVP- VA (6.17 μg/mL) prepared in 10mM HEPES with 150 mM NaCl (pH=7.3) buffer solution, upon exciting at 420nm acquired between 15.0 °C and 70.0 °C, with 5°C increment. (B) Average Integrated Fluorescent ratio, Q, of the blue region before (I<sub>blue</sub>), to the green region (I<sub>green</sub>) after the iso-emission point at 500 nm versus the temperature acquired between 20.0 °C and 70.0 °C - 5.0 °C increment three independent thermal measurements.....75
- 4.7. (A) Thermal response of PPE-CO<sub>2</sub> (5 μg/mL) in complexation with PVP- PS (19.45μg/mL) prepared in 10mM HEPES with 150 mM NaCl (pH=7.3) buffer solution, upon exciting at 420nm acquired between 15.0 °C and 70.0°C,with 5 °C increment. (B) Average Integrated Fluorescent ratio, Q, of the blue region before (I<sub>blue</sub>), to the green region (I<sub>green</sub>) after the iso-emission point at 500 nm versus the temperature acquired between 20.0 °C and 70.0 °C - 5.0 °C increment three independent thermal measurements..... 76
- 4.8. The relative sensitivity (% S) calculated from the thermal response ratio I<sub>blue</sub>/I<sub>green</sub> of (A) PPE-CO<sub>2</sub>-7/PVP-VA and (B) PPE-CO<sub>2</sub>-7/PVP-PS ..... 78
- 4.9. Cycling PPE-CO<sub>2</sub>-7 (5 μg/mL)/PVP-VA (6.17 μg/mL) between 20.0 °C and 70.0 °C). Lines connecting the experimental points are for visual aid only. The experiment was performed in 10 mM HEPES with 150 mM NaCl (pH=7.3) buffer solution, and the solution was kept to stabilize for 5 min before each measurement..... 79
- 4.10. Cycling of PPE-CO<sub>2</sub> -7 (5 μg/mL)/PVP-PS (19.45 μg/mL) between 20.0°C and 70.0 °C, with its respective fluorescent emission spectra. Lines connecting the experimental points are for visual aid only. The experiment was performed in 10 mM HEPES with 150 mM NaCl (pH=7.3) buffer solution and the solution were kept to stabilize for 5 min before each measurement.....80
- 4.11. (A) Sequential images acquired using a DSLR camera upon exciting a film of PPE-CO<sub>2</sub>-7/PVP-VA using a UV lamp when placed on a Peltier heater. The circle highlights the analyzed region of interest. (B) Average fluorescent intensity obtained by dissecting the images in (A) into their RGB components and plotting the blue channel intensity versus the measured temperature.....82
- 4.12. Sequential images acquired using a DSLR camera upon exciting a film of PPE-CO<sub>2</sub>-7/PVP-VA + Rhodamine B using a UV lamp when placed on a Peltier heater. The circle highlights the analyzed region of interest. (B) Average fluorescent intensity obtained by dissecting the images in (A) into their RGB components and plotting the

red and blue channel intensities versus the measured temperature. (C) The ratio of the average intensities of the two channels plotted in (B) versus the measured temperature.....	84
4.13. Thermogravimetric analysis for (A) PVP-VA, PVP-VA/ PPE-CO <sub>2</sub> -7, and PVP-VA/ PPE-CO <sub>2</sub> -7/Rhodamine B and (B) PVP-PS, PS/PPE-CO <sub>2</sub> -7.....	86
5.1. Chemical structures of (A) Curcumin, (B) Agarose, and (C) schematic representation of Curcumin-Agarose-MNP complex.....	90
5.2. Thermogravimetric analysis for Agarose, Agarose-Curcumin, and Agarose-Curcumin-MNP.....	92
5.3.(A) Fluorescent emission spectra of free curcumin remained in supernatant at 20.0 °C. (B) Calibration curve obtained for calculating the amount of Curcumin loaded and released With $R^2 = 0.982$ and $y = 265.35x + 848$ . The emission spectra were acquired in ethanol after excitation at 420 nm. The lines connecting the experimental points are for visual aid.....	93
5.4 The release of curcumin form magnetic agarose after being exposed to an external magnetic field. The emission spectra were acquired in ethanol after excitation at 420 nm. The lines connecting the experimental points are for visual aid.....	95
5.5. Comparison between the fluorescence intensities of curcumin released when heated by induction and in waterbath. The histograms represent the average fluorescent value of 3 independent trials at RT and 45° C. Error bars were calculated from the standard deviations of the 3 independent measurements. The emission spectra were acquired in ethanol after excitation at 420 nm .....	96
5.6. Comparison between the fluorescence intensities of curcumin released when different amount of MNPs (A) 0.2778 g/ mL and (B) 0.5556 g/ mL, upon heating by induction. The lines connecting the experimental points are for visual aid.The emission spectra were acquired in ethanol after excitation at 420 nm .....	98
5.7. Emission spectra of maximum fluorescence intensities of curcumin released with stirring at 1150 rpm ( ▲ ) and without stirring ( ● ). Measurements were done at room temperature and after heating in waterbath.Emission spectra were acquired upon excitation at 420 nm in ethanol.....	99
5.8. Fluorescent microscopy images of agarose gel before (A) and after (B) exposure to an alternating magnetic field (C) Integrated fluorescence intensity using ImageJ software before and after exposure to an alternating magnetic field .....	101

## TABLES

### Table

3.1. Hydrodynamic radius for the prepared liposomes measured using NanoPlus HD .....	43
5.1. Hydrodynamic radius for the prepared particles of Agarose-Curcumin-MNP measured using NanoPlus HD.....	91

# CHAPTER 1

## INTRODUCTION

Temperature is the most important and fundamental parameter in a broad range of physical, chemical, and biological activities[1, 2], it exquisitely affects many physiological processes, such as enzyme reaction[3], gene expression[4], cell division[5], and metabolism[6]. Moreover, it plays a significant role in, catalysis and electronic devices operation. Scientists have always been trying to study the effect of temperature on such aspects. For instance, any minimal change at the cellular level from the optimum value would launch a cascade of biochemical reactions[7]. Cells use these biochemical reactions to preserve the optimum temperature for biomolecular dynamics and enzymatic operations[8]. Furthermore, any metabolic activity would lead to temperature variations. For example, cancer cells carry replicative divisions higher than normal cells. The increased rate of cell division in cancer cells require metabolic pathways to be redesigned, which increase their metabolic rate; hence the mutant cell temperature would augment[9]. Thus, in medicinal science cancer alongside other pathogens are characterized by extraordinary heat production.



## 1.1 Importance of Thermal Mapping

Cells that are the basic unit of life constitute many various number of chemicals and organelles that appear to have a unique role in physiochemical mechanisms. For instance, mitochondria are the organelles where cells store and release energy in the form of a molecule called adenosine triphosphate (ATP)[10]. Each cell organelle is held accountable for various physiological and pathological events, that is reflected by variations in intracellular temperature [11].

Uchiyama *et al.* recently has reported that each organelle within the cell has its own optimum temperature. To prove his statement he developed a polymer-based fluorescent thermometer. He reported that the observed intracellular temperature distribution of the nucleus and the centrosome of COS7 cell were significantly different than that of the cytoplasm and that the cell cycle affects the temperature gap between the nucleus and the cytoplasm. The heat production from mitochondria was also observed. These results showed that this new intracellular thermometry could determine an intrinsic relationship between the temperature and organelle function [12].

Therefore, temperature distributions inside a living cell can aid in determining the thermodynamics and functions of cellular components. Consequently, intracellular temperature mapping of living cells would enhance our understanding of cellular events, and aid in the establishment of novel diagnoses and therapies on the pathogenesis of cancer and other diseases.

Notably, temperature is a vital parameter to regulate cell function and biochemical reactions within a cell, which in turn will influence the intracellular temperature. In this context, it is really fundamental to measure cellular temperature to provide sufficient information to fully understand life science. Temperature being a fundamental parameter

is not only limited to life science but also its importance is observed in technology. One important example is the effect of self-heating in integrated electronics where power dissipation in form of heat has become a limiting factor [12]. Thermal fluctuations in micro-electronics and MEMs appeared to have a major and limiting effects on their performance and reliability[13]. Monitoring and determining these variations enable the study of heat transfer and generation, as they help scientists in understanding and exploring the underlying thermophysical processes. The ability to study temperature and thermal conductivity distributions in nanosystems, and electronic systems open broad dimensions for the development of future energy conversion and computing devices[14].

Note that, it's crucial to map temperature at the nanoscale level since many physical properties related to thermodynamic change drastically at the nanoscale levels. Understanding these effects holds great promises for fundamental discoveries in the field of electron-phonon interactions, as they are relevant for the development of low power electronics and efficient thermoelectric energy harvesting systems[15].

To sum up, temperature being the most important and common physical parameter plays a key function in diverse scientific fields. Tracking and characterizing its variations is of high importance in the field of industry nanotechnology and biomedical sciences.

### ***1.1.2 Conventional Thermometry Limitations***

Traditional thermometers are limited by their low resolution (down to 10  $\mu\text{m}$ ) and their inability to function within cells. These limitations and the integral role temperature plays in various fields has forced scientists to develop and implement new strategies and methods to map thermal fluctuations with high spatial resolution down to few nm. The earliest developed method was the micro-calorimeter, but also it was limited by its low temporal resolution. Another example is infrared thermography that has been widely used since it's non-contact, non-destructive and high-throughput properties; however the efficiency of this method is highly dependent on the properties of material being studied. Moreover it does not yield absolute temperature values so calibration is prerequisite for all measurements [16, 17].

Ideal thermosensitive techniques are expected to satisfy multiple criteria, such as in high spatial resolution, minimal signal calibration over time, non-invasive, reproducible, and high-throughput properties. The inability to satisfy these features has been a challenge to intracellular temperature mapping.

## **1.2 Fluorescent-based Nano-thermometry**

Fluorescent based thermal sensing appeared to be the most prominent and promising method; as it allowed scientists to map temperature down to the molecular level with high spatial resolution

Several types of luminescent nano-thermometers have been utilized into the scientific fields. Examples on the diverse systems are the organic dyes[18, 19] organic-inorganic hybrid nanoparticles[20], polymer nanoparticles[20], quantum dots (QDs)[21], polymer dots (PDs),[22] fluorescent proteins [30] and lanthanide ions ( $\text{Ln}^{3+}$ )[23, 24]. Their signal relies on their fluorescent properties specifically their thermo-sensitive

physical properties. For examples, intensity of fluorescence[25, 26], band-shape of fluorescence[27], bandwidth of fluorescence[28], fluorescence lifetime[12] and fluorescence polarization anisotropy[29].

The developments in fluorescence spectroscopy allow the measurement with single molecule precision and unprecedented spatial resolution.

Generally, fluorescence based sensors adopt three different strategies: (a) fluorescence quenching (turn-off), (b) fluorescence enhancement (turn-on), and (c) fluorescence resonance energy transfer (FRET).

FRET is an important physical phenomenon with considerable interest for the understanding of biological systems and with potential applications in optoelectronic and thin film device development.

### ***1.2.1 Förster Resonance Energy Transfer***

Fluorescence Resonance Energy Transfer (FRET) is a physical phenomenon that was first proposed by Theodor Förster over 50 years ago. This radiationless transmission process is highly dependent on distance between the donor and acceptor moieties, besides that the transmission is through non-radiative dipole-dipole coupling. The occurring transfer of energy between the chromophores leads to the reduction in donor's intensity and its excited state lifetime; however there is an enhancement in the acceptor fluorescence intensity. The efficiency of FRET is dependent on the inverse sixth power of intermolecular separation (Equation 1.1).

$$E_{FRET} = \frac{1}{1 + \left(\frac{R}{R_0}\right)^6} \quad \text{Equation 1.1}$$

Where  $R$  is the distance between donor and acceptor and  $R_0$  is the characteristic distance at which 50% energy is transferred.

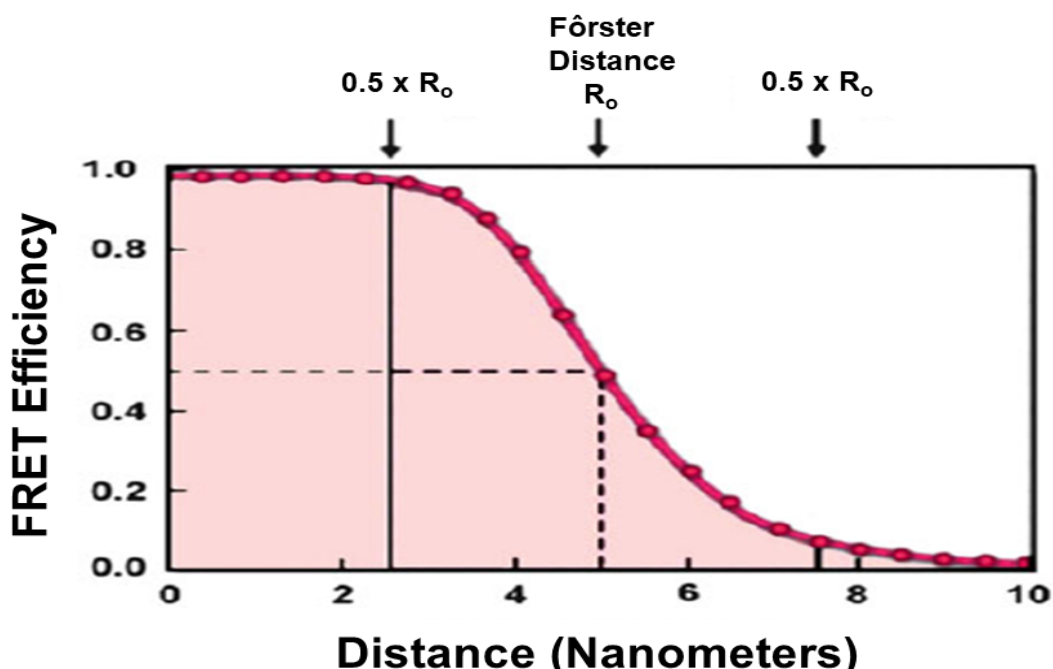


**Figure 1.1:** Distance dependence of FRET efficiency. The Forster theory shows that efficiency  $E$  varies as the inverse sixth power of the distance between the two molecules (denoted by  $r$ ) (Reprinted with permission from Schlattner *et al*)[30]

$R_o$  is calculated by the following equation:

$$R_o^6 = \frac{9000(\ln 10)\Phi_D K^2 J(\nu)}{128\pi^5 N_A n^4} \quad \text{Equation 1.2}$$

Where  $\Phi_D$  is the quantum yield of the donor molecule,  $N_A$  is Avogadro's number,  $n$  is the index of refraction of the medium,  $K^2$  is an orientation factor and  $J(\nu)$  is the normalized spectral overlap of the donor emission and the acceptor absorption. FRET yields accurate measurements and is highly efficient if the donor and acceptor are positioned within the Förster radius (the distance at which half the excitation energy of the donor is transferred to the acceptor)(Figure 1.1)

The utilization of guest induced-fluorescence resonance energy transfer (FRET) system having simplicity, sensitivity and dynamic range ought to be as a productive way to deal with ratiometric fluorescent probes[31].

### **1.2.2 Limitations**

Fluorescence signal is limited, by its sensitivity to many external factors. In which they might affect the thermometric response. Probes with ratiometric signals minimize such errors produced by the light source fluctuations, the optical setup, and, the detector instability as well as changes in the fluorophore concentration [32, 33]. They often consist of two subunits each with a different thermal response property. Any fluctuation in the excitation source is then eliminated by the subunits ratio.

To map and characterize intracellular temperature distribution with high precision, the thermometers should simultaneously satisfy many requirements: proper detection range; high-temperature resolution; high spatial resolution; real-time capability; functional independence from environmental changes in pH, ionic strength, and surrounding biomacromolecules; a concentration-independent output, and high repeatability [34, 35].

Conjugated polyelectrolytes, being a class of polymer with exceptional optoelectronic properties and high brightness, appeared as likely prospects at this stage.

### **1.3 Conjugated polyelectrolytes**

Conjugated polyelectrolytes are a versatile class of semiconducting polymers with alternating single-double bonds functionalized with charged side chains to enhance their solubility in aqueous media. These organic macromolecules are classified into cationic, anionic, and zwitterionic CPEs. Therefore, their physical, chemical and electronic properties are not only determined by their hydrophobic backbone but also by their ionic side chains[36].

The interest in these conjugated polyelectrolytes stems from their sensitivity to their microenvironment and the effect of their structural conformation on their unique set of photophysical properties. Extensive scientific effort have been implemented in understanding such properties including  $\pi$ -electron polarization, exciton and charge transport, variable bandgap for light absorption and emission, and chemical sensitivity. CPEs are characterized by their high quantum yield, rapid transport of charge carriers, high extinction coefficient, and delocalization of backbone electrons and efficient through the bond- and through space energy transfer.

Their useful optical and electronic properties make them excellent candidates to be used in various applications such as in optoelectronic devices, optical sensors (chemo- and biosensors), and biological imaging.

### ***1.3.1 Conjugated Polyelectrolyte Biocompatibility***

Conjugated polyelectrolyte possesses several important characteristics to make them a robust tool for biological applications. For instance, Liu's group studied the cytotoxicity of P14-Gd on MCF-7 cells. The obtained P14-Gd NPs showed successful internalization to the cellular cytoplasm of MCF-7 cells. Most importantly they showed extremely low in vitro cytotoxicity against cells, even at 70 times the concentration used in cellular imaging. The obtained study revealed that P14-Gd can serve as an excellent dual-modal fluorescence and MR imaging probe with high photostability and low in vitro and in vivo toxicity[37]. Another example of the biocompatibility of conjugated polyelectrolytes for cell imaging application was reported by Wu *et al.* PPE, PFPV, PFBT, and MEH-PPV conjugated polymer dots were used as fluid phase marker of pinocytosis in macrophages cells[38]. The images show that CP dots crossed the cell



membrane. CP dots showed no cytotoxicity under the loading concentration and the incubation time.

Furthermore, Abou Matar *et al.* has reported the high cellular uptake of MPS-PPV in both HEK and HeLa cells. The negatively charged conjugated polyelectrolyte showed no cytotoxicity when added to both cells line. In addition, the usage of the higher concentrations confirmed that the CPE doesn't compromise the membrane that leads to cellular death within the tested period (Figure 1.2) [39].

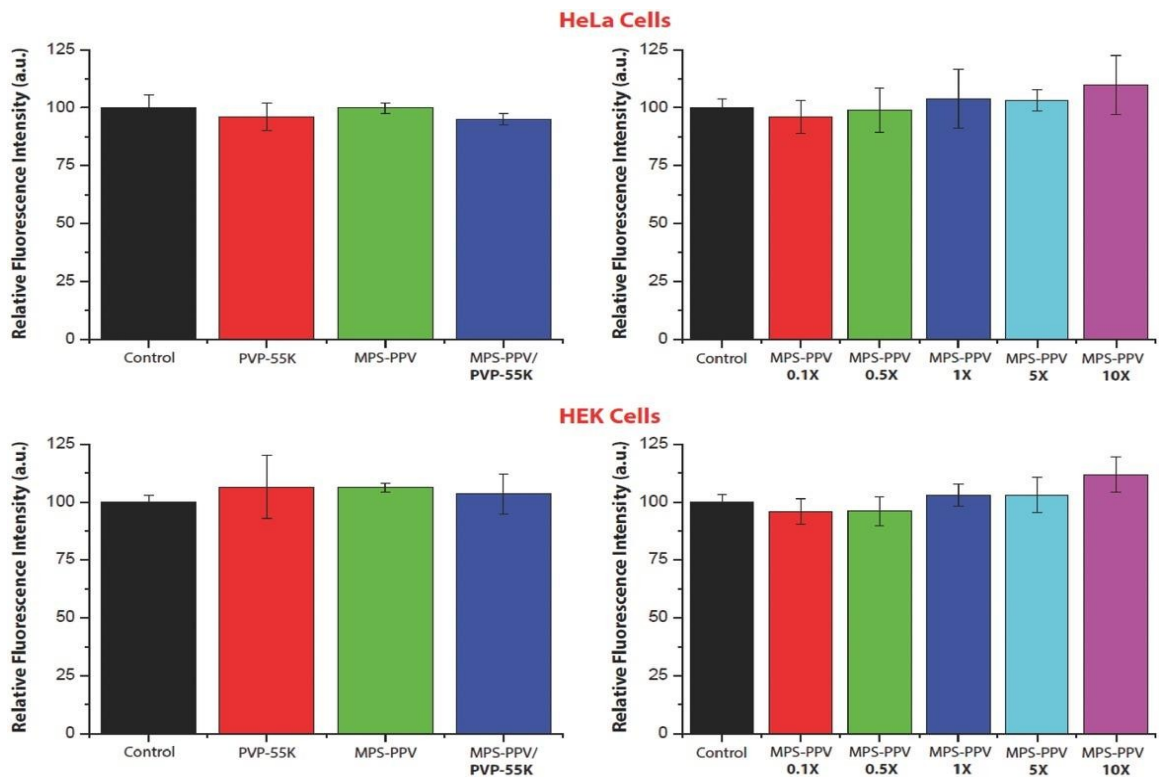


**Figure 1.2:** Cell viability determined by CellTiter-Blue assay for PVP-55k, MPS-PPV, and MPS-PPV/PVP-55k and at different concentrations of MPS-PPV (0.1X, 0.5X, 1X, 5X, and 10X) incubated for 4 h with HeLa and HEK cells. Data are expressed as percentage of fluorescence relative to controls (untreated cells). The error bars represent the standard deviation of three replicates. (Reprinted with permission from Abou Matar *et al.*) [39]

Therefore, the biocompatibility of CPEs and their optoelectronic properties resulted in a great breakthrough in many biological and chemical sensing applications.

### ***1.3.2 Conjugated polyelectrolyte sensing mechanisms***

One common sensing mechanism in CPE is changes in its photophysical properties mediated by conformational changes of the conjugated backbone. Interactions between the analyte and the CPE would lead to a significant conformational changes in the CPE backbone and results in altering its absorption and/or emission properties[40]. Another important mechanism is amplified quenching mechanism that has attracted a great deal of attention. Such behavior has been referred to in the literature as the “molecular wire effect,” which was first described by Swager’s group[41]. These polymers are considered as poly-receptors wired in series and due to the delocalized electronic structure in CPs, there is an efficient energy migration over large distances. For instance some molecules (or ions) can act as quenchers enabling direct sensing of the targets. However this mechanism is limited and not selective toward specific targets. In addition to what was mention above fluorescence resonance energy transfer (FRET) is another type of sensing mechanisms [42]. CPEs are considered an excellent sensors due to their high extinction coefficients, high fluorescence quantum yields and efficient exciton migration.

### **1.4 Role of Temperature at the cellular level.**

Briefly temperature at the single cell level is under constant fluctuations due to the many biochemical reactions that take place within the cell. Cellular thermal sensing will be beneficial not just to understand the biochemical reactions inside the cells but also to exploit the influence of external environment to cells. For example, in the field of hyperthermia therapy, tumor cells are killed by heating at temperatures higher than 40 °C. Hyperthermia is a critical procedure since the inability to exactly monitor change in

temperature due to this procedure, would damage the healthy tissues around tumors[43]. Consequently, temperature sensing of living cells would provide not only insight into various cellular biochemical events, but also a grasp of cellular pathological state, allowing the development and implementation of diagnostic and therapeutic techniques for some diseases

#### ***1.4.1 Role of temperature in drug delivery***

Temperature plays a robust role in the field of drug delivery, for instance stimuli-sensitive drug delivery is a promising strategy for achieving on-demand release of drugs. External and internal stimuli, including temperature, pH, ultrasound, ionic strength, and magnetic field, can all be utilized to control and regulate the release of drugs rate and amounts in the desired location.[44] Among them, temperature has been commonly used as a stimulus to trigger drug release due to the fact that local body temperature can fluctuate in response to ambient conditions and diseases in some cases. So far, various materials with thermosensitive properties have been developed and implemented in the field temperature-sensitive drug delivery. For example poly(N-isopropylacrylamide) (poly-NIPAAm) and its derivatives, biodegradable polymers such as poly(lactic-co-glycolic acid) (PLGA) and poly(ethylene glycol) (PEG)[45].

As such the effect of drug at the cellular level can be exploited and can aid in an unraveling the underlying interactive mechanism between the drug and the cells at the nanoscale, by just observing the inter and intracellular temperature variations with high spatial resolution upon drug cellular uptake, this represents a breakthrough in disease therapy.

## 1.5 Objectives

Thermal mapping at the cellular level paves the way for significant advancement in establishing novel diagnoses and therapies on the pathogenesis of cancer and other diseases. It is experimentally proven that a solid correlation between complex biochemical processes and the functioning of biomolecules in living cells at high precision can be established by monitoring the temperature fluctuations. Furthermore, the advancement in microelectronic and MEMS, made it important to map thermal fluctuations due to the vital role it plays in their operation. Furthermore, being able to characterize temperature at such a low level would significantly aid in advancement in the field of nanotechnology, life science, and medicinal science.

In this work, we aim to develop a nanothermometer that enables thermal mapping with a high spatial resolution based on a chromophore complex between a conjugated polyelectrolyte and a lyophilic dye. Moreover, Polymeric probes suffer from hysteresis as they cycle between relaxed configuration at high temperatures and a collapsed state at lower temperatures. This can lead to irreversibility in the reported fluorescent signal with the change in the CPE microenvironment. As such the polymeric probe will be cycled multiple times to make sure that our probe doesn't suffer from such a drawback. In addition various probes have shown instability when subjected to different pHs, consequently this limit their applications to only under controlled conditions, therefore, the sensitivity of the nanothermoemter will be assessed under different pHs.

In the second project we aim to develop a probe to map thermal variations in thin polymer films through reporting on a novel fluorescent-based thermal sensor. In this work the stability and thermal sensitivity of the PPE-CO<sub>2</sub>-7 based nanothermometer when complexed with PVP copolymers will be exploited in solution and when spun casted on

quartz. Consequently the film thickness will be assessed since various thicknesses may affect the recorded sensitivity,

Controlled drug delivery has the ability to influence the therapeutic agent performance such as absorbance, circulation time, cellular penetration, simply by altering their concentration, location, duration, coating, and size. Therefore, it provides a promising way to minimize side effects and increase therapeutic efficacy. Chapter 5 describes the development and characterization of a new nanoparticle-based drug carrier with controlled release properties.

In this work we aim to develop magnetic agarose carriers for controlled curcumin release. The release efficiency will be assessed under alternating magnetic field and in water bath to determine if the increase in temperature is the only factor affecting the release.

## CHAPTER 2

### MATERIALS AND METHODS

In this chapter we present a summary of the materials used and the methodologies followed in the reported experiments of chapters 3, 4 and 5.

#### ***2.1 Fluorescent Thermal Sensing using Conjugated Polyelectrolytes lipid membrane.***

##### ***2.1.1 Materials***

HEPES, and Poly[5-methoxy-2-(3-sulfopropoxy)-1,4-phenylenevinylene] potassium salt solution 0.25 wt. % in H<sub>2</sub>O (MPS-PPV) were purchased from Sigma-Aldrich. 1,1'-dioctadecyl-3,3,3',3'-tetramethylindodicarbocyanine perchlorate (DID) was purchased from Invitrogen. Cholesterol and 1,2-dipalmitoyl-sn-glycero-3-phosphocholine (DPPC), 1,2-dioleoyl-sn-glycero-3-phosphocholine (DOPC), 1-palmitoyl-2-oleoyl-glycero-3-phosphocholine (POPC), were purchased from Avanti polar lipids.

##### ***2.1.2 Methods***

###### ***2.1.2.1 Liposomes Preparation***

DPPC powder was dissolved in chloroform to a final concentration of 10 mg/mL. The sample was then evaporated using a stream of nitrogen while rotating the vial to create a thin lipid film on its walls. The dried film was hydrated to a final lipid concentration of 21.5 mM with MPS-PPV (1.6mM in monomer concentration) in 10mM HEPES-150 mM NaCl pH=7.33. The resulting suspension was subsequently vortexed and sonicated at T=50.0 °C for 10 min. The liposome solution was then extruded 15 times

above the lipid transition temperature through a 200 nm pore size polycarbonate membrane using a mini-extruder. For liposomes containing cholesterol, the procedure was the same except that different amounts of cholesterol were added to DPPC before the addition of chloroform, to give 10, and 20 mole % cholesterol.

#### 2.1.2.2 Number of lipid molecule per liposome:

In order to know the number of lipids per liposome, the surface area of a liposome ( $4\pi r^2$ ) is divided by the area of DPPC lipid head group estimated as  $0.82 \text{ nm}^2$ . Since the liposome is made up of 2 lipid layers then the number of lipid molecules per liposome

$$\left(\frac{2 \times 125664 \text{ nm}^2}{0.82 \text{ nm}^2}\right) = 306496$$

#### 2.1.2.3 Number of dye molecules per liposome

At a DID:DPPC 1/3403 mole ratio, the number of DID molecules per liposome is

$$\left(\frac{306496}{3403}\right) \approx 90$$

#### 2.1.2.4 Liposomes concentration

The stock concentration of DPPC prepared is 21.5 mM. Each liposome is made up of 360496, thus the liposomes stock concentration is:

$$\begin{aligned} &= \frac{\text{Concentration of DPPC}}{\text{number of DPPC molecules per liposome}} \\ &= \frac{21.5 \text{ mM}}{306496} \\ &= 70.1 \text{ nM} \end{aligned}$$

#### 2.1.2.5 DPPC final concentration is as follows

$$\begin{aligned} &= \text{stock concentration} \times \left( \frac{\text{volume added}}{\text{final volume}} \right) \\ &= 21.5 \text{ mM} \times \left( \frac{50 \mu\text{l}}{2050 \mu\text{l}} \right) \\ &= 5.24 \times 10^{-4} \text{ mM} \end{aligned}$$

#### 2.1.2.6 Liposomes final concentration

$$\begin{aligned} &= 70.1 \text{ nM} \times \left( \frac{50 \mu\text{l}}{2050 \mu\text{l}} \right) \\ &= 1.71 \text{ nm} \end{aligned}$$

#### 2.1.2.7 Absorption Measurements

Absorption spectra were measured using a Jasco, V-57UV/VIS/NIR spectrophotometer in double beam mode and air as the baseline. Throughout the measurements the analyzed samples/reference/blank were placed in a 1 cm x 1 cm quartz cuvettes, and the total volume was kept constant and equal to 2 mL. The reference sample consists of 10 mM HEPES-150 mM NaCl (pH=7.33) buffer while that of the sample, contains additionally 11  $\mu\text{L}$  of MPS-PPV.

#### 2.1.2.8 Steady State Fluorescent Spectroscopy Thermal Measurements

Steady-state fluorescence spectroscopy was carried out using a Thermo Fisher Lumina spectrometer equipped with a temperature controller unit (T3 Quantum Northwest)

The analyzed samples contain: 10 mM HEPES-150 mM NaCl mixture, with either 50  $\mu\text{L}$  of DPPC-DID/MPS-PPV with varied amounts of cholesterol (0, 10, 20 mole %) or 50  $\mu\text{L}$  of DOPC-DID/MPS-PPV, or 50  $\mu\text{L}$  of POPC-DID/MPS-PPV.



The control samples contain: 10 mM HEPES-150 mM NaCl mixture, of either 50  $\mu$ L DPPC/MPS-PPV or 50  $\mu$ L DPPC-DID or 50  $\mu$ L DOPC-DID.

Throughout the measurements the analyzed samples/reference/blank were placed in a 1 cm x 1 cm quartz cuvettes, and the total volume was kept constant and equal to 2 mL.

#### 2.1.2.9 Characterization of the Prepared DPPC Liposomes

The average diameter of the prepared liposomes was estimated using dynamic light scattering. The hydrodynamic radius was measured for both DPPC and DPPC-DID/MPS-PPV samples. Samples were diluted then suspended in cuvettes containing 2 mL deionized water.

## **2.2 Fluorescent Thermal Sensing using Conjugated Polyelectrolytes in Thin Polymer Films**

### *2.2.1 Materials*

The following materials have been used for our thermal sensing project: Poly (phenylene ethynylene) carboxylate, PPE-CO<sub>2</sub>-7, with 7 repeating units were synthesized as previously described by our group and others[39, 46]; Poly (1-vinylpyrrolidone-co-vinyl acetate), PVP-VA, Mw= 50K (Aldrich); Poly (1-vinylpyrrolidone-co-styrene), PVP-PS, 38 % emulsion in H<sub>2</sub>O, <0.5  $\mu$ m particle size (Aldrich); Rhodamine B isothiocyanate, C<sub>29</sub>H<sub>30</sub>ClN<sub>3</sub>O<sub>3</sub>S, Bio-Reagent, mixed isomers, suitable for protein labeling (Aldrich); Fluorescein 5(6)-isothiocyanate, C<sub>21</sub>H<sub>11</sub>NO<sub>5</sub>S,  $\geq$ 90 % (Aldrich); Ammonium hydroxide, NH<sub>4</sub>OH, ACS reagent, 28-30 % solution in water (Acros); Hydrogen Peroxide, H<sub>2</sub>O<sub>2</sub>, puriss., meets analytical specification of Ph. Eur., BP, USP, 30-31 % (Aldrich); HEPES solution: N-(2-Hydroxyethyl) piperazine-N'-(2-ethanesulfonic acid), 1 M, pH 7.0-7.6, sterile-filtered, Bio-Reagent, suitable for cell

culture (Aldrich); Sodium Chloride, NaCl, extra pure, SLR (Fisher); Quartz slides 25.4 x 25.4 mm<sup>2</sup> (Science Outlet); PELTIER TEC1- 12710; Power Supply 30V- 5A D ZHAOXIN, 0.1 volt increment; Fluke 80BK-A Type K Multimeter Thermocouple, and Deionized water (18 μΩ, Nanopure Diamond, CRSL, AUB) for solution preparations and dilutions.

## *2.2.2 Methods*

### **2.2.3 Solution Preparations**

#### 2.2.3.1 PVP-VA Stock Samples

PVP-VA stock solution was prepared by dissolving the stock powder in 10 mM HEPES-150 mM NaCl (pH= 7.33) buffer yielding a final concentration of 100 mg/mL, denoted as 1X. A series of further dilutions were done yielding standard solutions of respective concentrations 0.5, 0.1, 0.05, and 0.01 X.

#### 2.2.3.2 PVP-PS Stock Samples

The concentration of the PVP-PS stock solution is 395.2 mg/mL, denoted as 1X. This stock solution was used to prepare a series of further dilutions in the same buffer yielding standard solutions of respective concentrations 0.5, 0.1, 0.05, and 0.01 X.

#### 2.2.3.3 Titration of PPE-CO<sub>2</sub>-7 with Different Polymer Ratios

To optimize the PPE-CO<sub>2</sub>-7/PVP-copolymer ratio, a CPE solution with a final polymer concentration of 5 μg/mL was prepared in 10 mM HEPES 150 mM NaCl

(pH=7.33) and maintained at 20.0 °C. Incremental amounts of the copolymers were subsequently added to the solution.

All the analyzed samples were prepared by dissolving PPE-CO<sub>2</sub>-7 (450 µg/mL) in 2 mL of 10 mM HEPES-150 mM NaCl (pH=7.33) before introducing different incremental amounts of the two polymers separately. Titration was done until reaching saturation in the emission intensity. The final concentration of the polymer in the cuvette was calculated as follows:

$$V_t = 2022 \mu\text{L} + V_i \text{ (polymer) in } \mu\text{L}.$$

$$[\text{Copolymer}] = \frac{\frac{\sum(C_1V_1 + C_2V_2 + \dots)}{V_i = \sum(V_1 + V_2 + \dots)}}{2022 + V_i}$$

$$[\text{PPE} - \text{CO}_2]_{\text{final}} = \frac{22 \mu\text{L} \times 450 \frac{\mu\text{g}}{\text{mL}}}{2022 \mu\text{L}} = 4.90 \mu\text{g/mL}$$

## 2.2.4 Characterization and Measurements

### 2.2.4.1 Absorption Measurements

Absorption spectra were measured using Jasco, V-570 UV/VIS/NIR Spectrophotometer in double beam mode and air as the baseline. Throughout the measurements the analyzed sample/reference/blank were placed in a 1 cm x 1 cm quartz cuvette, and the total volume was kept constant and equal to 2 mL. The blank sample contains 10 mM HEPES-150 mM NaCl and 4.90 µg/mL of PPE-CO<sub>2</sub>-7. The analyzed sample contains 10 mM HEPES-150 mM NaCl 4.90 µg/mL of PPE-CO<sub>2</sub>-7 and additionally different volumes of PVP-PS and PVP-VA.

#### 2.2.4.1 Steady State Fluorescent Spectroscopy Thermal Measurements

Steady-state fluorescent spectroscopy was acquired using a Thermo Fisher Lumina spectrometer equipped with a temperature controller unit (T3 Quantum Northwest).

The control solution consists of: 2 mL of 10 mM HEPES-150 mM NaCl (pH=7.3) mixture + 450 µg/mL PPE-CO<sub>2</sub>-7, while the analyzed one contains: 2 mL of 10 mM HEPES-150 mM NaCl mixture, 450 µg/mL PPE-CO<sub>2</sub>-7, in addition to variable volumes of either PVP-VA or PVP-PS.

In all measurements the total volume was kept constant and equal to 2 mL.

#### 2.2.4.2 Quartz Cleaning

Quartz slides were first wiped in acetone to remove any traces of the thin films, then they were placed in boiling absolute ethanol for 30 min. The quartz were removed from the hot ethanol and placed in NH<sub>3</sub>/H<sub>2</sub>O<sub>2</sub> solution (of ratio 7:3 (v/v) of 28% NH<sub>3</sub>-30% H<sub>2</sub>O<sub>2</sub>). Followed by washing them in deionized water multiple times, and then they were air dried

#### 2.2.4.3 PPE-CO<sub>2</sub>-7/ PVP-VA Film Assembly

PPE-CO<sub>2</sub>/Polymer mixtures were coated on the quartz slide using the WS-650MZ- 23NPP spin coater machine and via a static-6-steps process. The cleaned quartz slide was first placed on a vacuum chuck followed by activating the vacuum. Then the samples were deposited on the middle of the quartz and spread evenly. The first 3 steps were relatively low in speed, starting with 100 rpm and 200 rpm for the first two- 30 sec runs, followed by a one-minute 300 rpm-run. This speed was then increased

in the other half of the process to 1000 rpm and 1500 rpm for a 30-sec run each, reaching the maximum speed, 2000 rpm, in the final minute.

#### 2.2.4.4 Thermal Imaging of Thin Polymer Films

The quartz coated with the PPE-CO<sub>2</sub>-7/polymer mixtures were placed on a thermoelectric cooler (TECL) - Peltier (TEC1-12710) device- and imaged, under UV light exposure (365 nm), using a regular DSLR Canon 750D camera- 60 mm macro lens- (exposure time 1/5 s, f/5.6, ISO 100). The temperature was regulated using a DC power supply connected to the Peltier by ranging the applied voltage between 0 V and 6 V with 1 V increment. Before each imaging, and after setting the voltage, the quartz was kept for 5 min for the temperature to stabilize.

Temperature changes were measured using a Fluke 80BK-A Type K Multimeter thermocouple (-40 to 260°C) connected directly to the top of the quartz.

#### 2.2.4.5 Analysis of Images

Images taken by the DSLR Canon 750D camera- 60 mm macro lens, were first converted into jpeg using the lightroom software.

Followed by dissecting them into red-green-blue components, subsequently the integrated intensity was calculated using ImageJ software.

#### 2.2.4.6 Fourier-transform Infrared Spectroscopy (FTIR)

The FTIR spectroscopy was performed on a Nicolet™ 4700 FTIR spectrometer. The complex's powder was mixed with KBR. The measurements were

carried out using pellets of the complex's powder mixed with KBR, and the spectra were collected in the 3750–400  $\text{cm}^{-1}$  range.

#### 2.2.4.7 Thermogravimetric Analysis (TGA)

The rate of degradation of the polymer-polymer complexes as a function of time was measured using the thermogravimetric analysis instrument: Netzsch TG 209 F1 Libra. The samples were first dried overnight and then analyzed between 30 °C and 1100 °C at a heating rate of 10.0 °C/min. The analyzed samples had the same mole ratio as the samples used in thin films thermal imaging.

### **2.3 Magnetic Responsive Agarose nanoparticles as Potential Vehicles for Controlled Curcumin Release**

#### **2.3.1 Materials**

The following materials have been used for our curcumin release project: Curcumin (Fisher), Agarose (Fisher), Iron (II) chloride tetrahydrate,  $\text{FeCl}_2 \cdot 4\text{H}_2\text{O}$ , puriss. p.a.,  $\geq 99.0\%$  (Aldrich); Iron (III) chloride hexahydrate,  $\text{FeCl}_3 \cdot 6\text{H}_2\text{O}$ , reagent grade,  $\geq 98\%$ , chunks (Aldrich); Trisodium citrate dihydrate,  $\geq 99\%$ , FG (Aldrich); Ammonium hydroxide,  $\text{NH}_4\text{OH}$ , ACS reagent, 28-30 % solution in water (Acros); Ammonium hydroxide,  $\text{NH}_4\text{OH}$ , ACS reagent, 28-30 % solution in water (Acros); and Deionized water (18u $\Omega$ , Nanopure Diamond, CRSL, AUB) for solution preparations and dilutions

#### **2.3.2 Methods**

##### 2.3.2.1 Synthesis of Agarose micro particles

50 mg agarose was dissolved in 4 mL PBS and stirred mechanically for 10 min at 90 °C. then the solution was added to the precipitating solution and stirred at 200

rpm. After 15 min the mixture was placed in an ice bath and stirred. Followed by centrifugation and washing for 4 times with DIW and 4 times with ethanol. The precipitate was re-suspended in PBS.

#### 2.3.2.2 Synthesis of Agarose-Curcumin microparticles

50 mg agarose was dissolved in 4 mL PBS and stirred mechanically for 10 min at 90 °C. 10 mg curcumin were dissolved in 300 µL DMSO and was added to the agarose solution. The curcumin solution was added to the agarose solution and stirred for 30 min. The following steps are the same as above.

#### 2.3.2.3 Synthesis of Agarose-Curcumin-MNP nanoparticles

50 mg agarose was dissolved in 4 mL PBS and stirred mechanically for 10 min at 90 °C. 30 mg curcumin was dissolved in 300 µL DMSO and were added to the agarose solution. 2 mL or 4 mL MNP solution were added to the agarose-curcumin mixture and stirred for 30 min. The following steps are the same as above.

#### 2.3.2.4 Synthesis of Iron oxide magnetic nanoparticles (MNP)

Briefly, equimolar masses of Iron (II) chloride  $\text{FeCl}_2 \cdot 4\text{H}_2\text{O}$  (2.4g) and Iron (III) chloride  $\text{FeCl}_3 \cdot 6\text{H}_2\text{O}$  (6.5g) were dissolved were dissolved in 80 mL DIW and stirred mechanically for 3 min under nitrogen stream. Followed by the addition of 20 mL ammonium hydroxide solution (28% w/v). 10 min later 10 gr of trisodium citrate dihydrate powder was dissolved and the whole mixture was stirred while the temperature was raised and maintained at 90 °C for 30 min. After cooling down to room temperature, the magnetic nanoparticles produced were collected by an external magnet and re-

suspended and washed with ethanol and DIW several times the, then re-suspended in 20 mL deionized water

#### 2.3.2.5 Dynamic Light Scattering (DLS)

The hydrodynamic size, and polydispersity index (PDI), of the prepared samples, were evaluated by dynamic light scattering (DLS) analysis using Brookhaven particle size analyzer. Samples were diluted then suspended in cuvettes containing 2 mL deionized water.

#### 2.3.2.6 Steady State Fluorescent Spectroscopy

Steady-state fluorescent spectroscopy was acquired by exciting at 430 nm using a Thermo Fisher Lumina spectrometer.

The release of curcumin was done in a 2 mL-tube containing 0.115 gr/mL Agarose-MNP-Curcumin complex. All solutions were placed in a 1 cm x 1 cm quartz cuvettes containing 2 mL ethanol. Before each measurement, the solution was allowed to homogenize and stabilize for 5 mins.

#### 2.3.2.7 Thermal Heating of Magnetic Nanoparticles- MagneTherm

MagneTherm was used to generate an alternating magnetic field using a built-in-coil NAN201003 at a 109.6 KHz. The increase in temperature was tracked using a thermocouple, dipped in solution and connected a multimeter. Initially, the voltage was increased to its maximum value that is equal to 31 V. Once the solution temperature reached 40 °C, the voltage was adjusted manually and monitored down to approximately 14 V to keep the solution thermally constant.



#### 2.3.2.8 Thermogravimetric Analysis (TGA)

The rate of degradation of the Agarose-Curcumin-MNP complex as a function of time was measured using the thermogravimetric analysis instrument: Netzsch TG 209 F1 Libra. The samples were first freeze dried overnight and then analyzed between 30 °C and 1100 °C at a heating rate of 10.0 °C/min.

#### 2.3.2.9 Microscopy Imaging

Microwells were first washed using PBS buffer, followed by the addition of Curcumin loaded magnetic nanoparticles. Then the excess solution of the nanoparticles was wiped away after the addition of silicon oil. The filled microwells were imaged at room temperature using upright fluorescence microscope Leica DM6 B. Then the microwells were exposed to an alternating magnetic field for 1 hour at 40 °C. Subsequently they were imaged again under the same experimental conditions. (10x objective and 183 ms exposure). Fluorescent intensities were quantified using the ImageJ software.

## CHAPTER 3

# FLUORESCENT-BASED THERMAL SENSING IN LIPID MEMBRANES

### 3.1 Introduction

Temperature is a fundamental physical parameter that plays a pivotal role in many cellular functions, including gene expression, protein stabilization, enzyme-ligand interactions and enzyme activity[47]. Intracellular temperatures fluctuate depending on the chemical reactions occurring inside cells, which are concurrent by either heat release or heat absorption, as well as on changes in the ambient temperature[48].

On the intracellular level, any induced function requires the cellular biological reactions to release Gibbs free energy. Consequently, this will lead to the release of the excess energy in the form of heat which results in local temperature variations [49]. Due to this critical role of heat, obtaining a non-homogeneous temperature distribution within the cell will directly correlate to the former's activity affecting its biochemical processes and reactions.

An immense attention has been drawn to understand the processes and to monitor temperature at the nanoscale level. This resulted in huge necessity to develop new precise thermometers, where imitative ones have failed to give accurate measurements. Despite the advancement in thermal mapping, we still lack a robust tool to accurately measure it at the cellular scale. More specifically, understanding chemical and physical processes at such low level is still a challenge. For example, physical damages in biological lipid membrane at low temperature are still elusive[50]. For instance lipid membranes are heterogeneous components and undergo phase transitions from gel-phase to liquid-crystalline lamellae, and some to a non-lamellar, over a range of temperatures[51]. These

membranes contain lipid rafts that are ordered packed structure and rich in cholesterol. They serve as an assortment platforms and center for signal transduction proteins. Moreover, any heat shock would lead to constitutional modification in the lipid membrane, which in turn it'll affect cell signaling.

Membrane permeability is another property that is temperature-dependent since heat controls the opening of ionic channels as a result of the change in interaction of lipid domains as they approach their phase transition temperature[52].

An accurate method for directly measuring intracellular temperatures within lipid membranes could provide information regarding the status of a cell and unravel many biochemical mechanisms at the cellular level; thus, the development of novel cellular thermometers has been of great interest[12]. Biosensors are devices that transform chemical or physical information contained within a sample into an analytically useful output; this information can range from the concentration of a specific sample component to total composition analysis[53]. Mainly sensors consist of two moieties, a recognition element and a physicochemical transducer. Where the target analyte remains in direct contact with the receptor or the recognition element, upon the interaction between the receptor and the target system a response is sent to the transducer which itself converts it -the response- into an electrical signal, that we are able to visualize and quantify. Moreover the recognition element can sense and map changes in its surrounding, where it's also converted to a useful signal.[54] Research on biosensors is dramatically active nowadays, where this field has attracted scientists from diverse disciplines. From an analytical viewpoint, biosensors offer numerous advantages over the conventional sensors including but not limited to minimal sample preparation, real time detection, and rapid response times [54].

In this project we aim on developing FRET pair thermal sensor to map temperature in lipid membranes in which a conjugated polyelectrolyte acts as a donor while the acceptor is a lyophilic fluorescent dye.

Several groups recently have reported the synthesis of conjugated polyelectrolytes based on both poly(phenylene vinylene) (PPV) and poly(phenylene ethynylene) (PPE) there is a growing interest in the use of these materials in various applications (biosensing applications)[55]. Smith *et al.* and his coworkers reported that the choice of solvent, ionic strength and counter ion valence control the conformation and superquenching properties of the water soluble, PPV based conjugated polymer. The material chosen in this study was poly(2-methoxy-5-propyloxy sulfonate phenylene vinylene) (MPS-PPV). They reported that MPS-PPV showed quit different optoeletronic properties in different environments (water, DMSO) for example, the fluorescence quantum yield of MPS-PPV is nearly 100 times stronger in DMSO than in water. Dynamic light scattering suggests a physical agglomeration of the MPS-PPV chains in both solvents, and intensity-dependent photophysics experiments indicate that the MPS-PPV chromophores are aggregated in water but not in DMSO[56].

To illustrate further on how the photophysical properties can be altered, Karam *et al.* hasreported the effect of neutral and in negatively charged lipid vesicles on photophysical properties of negatively charged conjugated polyelectrolyte system, poly[5-methoxy-2-(3-sulfopropoxy)-1,4-phenylenevinylene] (MPS-PPV)) (Figure 3.1) upon there encapsulation in the lipid vesicles at the single-molecule level[57]. They showed that MPS-PPV exhibit an aggregated conformation within the negatively charged vesicles where it exists as freely diffusing polymer, whereas it possess an extending conformation within neutral vesicles. In the first case, stepwise photobleaching in

fluorescence intensity-time trajectories and emission from low-energy chromophores along the chain were observed. In the second case, exponential decay of the intensity over time and a broad blue-shifted emission spectrum were observed, because the emission arises from the chromophores within the same isolated polymer chain[57]. All of the results have important implications for the use of conjugated polyelectrolyte in sensing applications.

The remarkable properties of CPEs motivated us to further utilize them in our sensing system. Darwish *et al* has already developed a ratiometric fluorescent thermal sensor using conjugated polyelectrolytes, specifically, poly-(phenylene ethynylene) (PPE-CO<sub>2</sub>-7) in complexation with polyvinylpyrrolidone. Using this probe, they successfully measured temperature fluctuations in solution, soft gels, and thin films. However, PPE-CO<sub>2</sub>-7, a stiff polymer, was not a good candidate to be used in lipid membranes. Karam *et al.* has previously shown that it embeds itself in the hydrophobic core as a single polymer unit and would not lead to a good thermal response [58]. As such, we turned our attention to poly[5-methoxy-2-(3-sulfopropoxy)-1,4-phenylene-vinylene] MPS-PPV which has been previously developed into many sensing schemes, especially in complexation with lipid membranes. Its spectroscopic properties are greatly influenced by its interactions with the lipid membrane [59-61]. As such, they have been used in many sensing platforms to detect lipase activity, and differentiate between different cell lines and microorganisms [62-64].

We argued that the change in the membrane fluidity with temperature should influence the solubility of the polymer backbone leading to a change in the recorded fluorescent signal, and changes in temperature in the lipid membranes would change the

local micro-viscosity, which should, in return affect the fluorescent response of MPS-PPV.

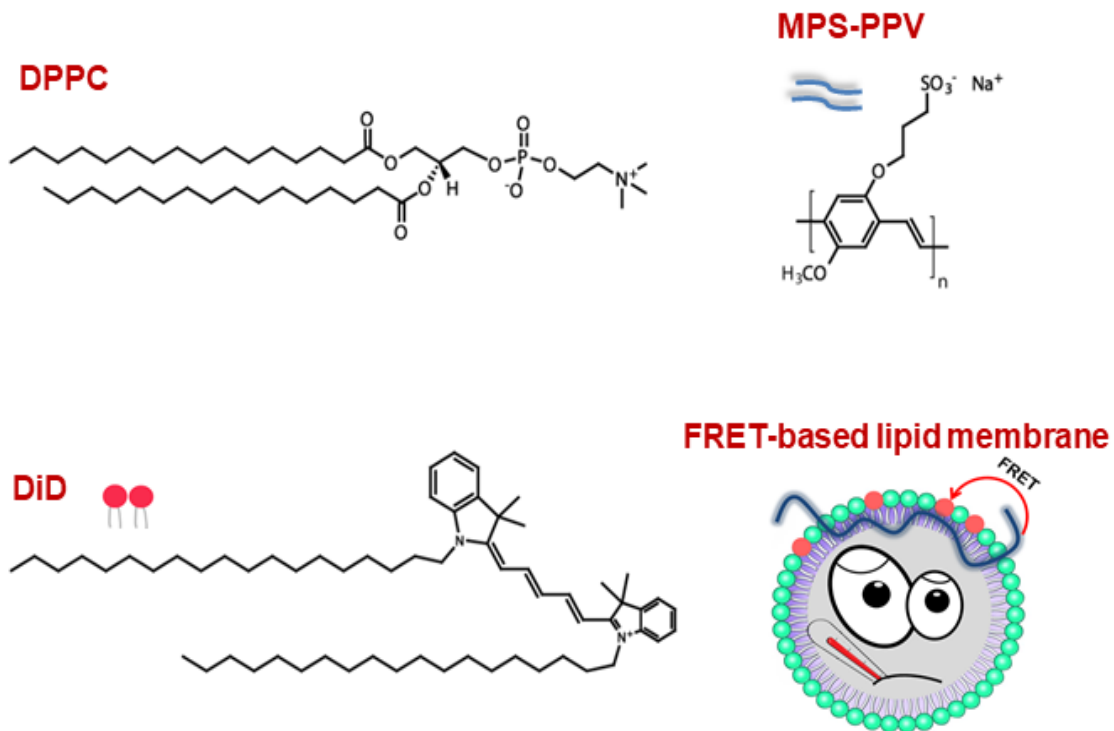


**Figure 3.1:** Chemical structures of Poly[5-methoxy-2-(3-sulfopropoxy)-1,4-phenylenevinylene] potassium salt solution (MPS-PPV), 1,1'-dioctadecyl-3,3,3',3'-tetramethylindocarbocyanine perchlorate (DiD), and schematic representation of the FRET-based thermal probe.

## 3.2 Results and Discussion

### 3.2.1 Thermal Sensing

To evaluate the thermal response of the CPE within the liposomes, the solution mixture was subjected to a gradual increase in temperature between 20.0 - 50.0 °C with a 5.0 °C increment.

Analyzed samples contain: 2 mL of 10 mM HEPES-150 mM NaCl mixture, DID-DPPC-MPS-PPV (1.71 nM) or, 10 % CHOL DID-DPPC-MPS-PPV, 20 % CHOL DID-DPPC-MPS-PPV, DID-DOPC/MPS-PPV, or DID-POPC/MPS-PPV.

### 3.2.2 *Reversibility and Cycling*

To check for the reversibility of our proposed system, the liposomes mixture was cycled 15 times between 20.0 and 50.0 °C. Analyzed samples contain: 2 mL of 10 mM HEPES-150 mM NaCl mixture, DID-DPPC-MPS-PPV (1.7 nM).

### 3.2.3 *pH stability*

To test for the stability of the probe at different pHs, the solution mixture was subjected to a gradual increase in temperature between 20.0 - 50.0 °C with a 5.0 °C increment in, basic, neutral and acidic mediums.

### 3.2.4 *Dynamic Light Scattering (DLS)*

To determine the size of our probe and to confirm the encapsulation we resorted to compare the hydrodynamic radius of the DID-DPPC/MPS-PPV liposomes to that of the bare DPPC liposomes. The increase in the cumulant diameter from 136.5 nm to 225 nm for bare DPPC and DPPC-DID/MPS-PPV liposomes respectively supports the suggested encapsulation (*Table 3.1*).

<b>Samples</b>	<b>Size (nm)</b>	<b>Polydispersity Index</b>
<b>DPPC</b>	<b>136.5</b>	<b>0.330</b>
<b>DID-DPPC/MPS-PPV</b>	<b>225</b>	<b>0.308</b>

**Table 3.1:** Hydrodynamic radius for the prepared Liposomes measured using NanoPlus HD.

### 3.2.5 Förster Resonance Energy Transfer Pair

To determine the spectral overlap between the donor emission (MPS-PPV) and acceptor absorption (DiD). We measured the free MPS-PPV emission and the free DiD absorbance (Figure 3.2).

DiD absorption overlaps with the emission of MPS-PPV allowing an efficient Förster resonance energy transfer (FRET) with a Förster radius ( $R_0$ ) of 4 nm.

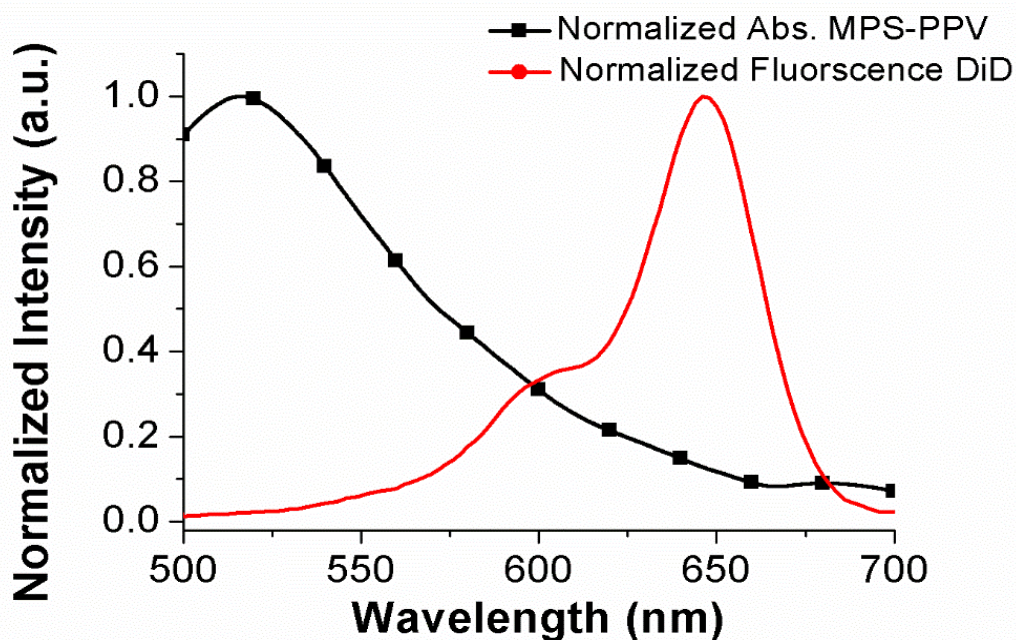


**Figure 3.2:** Normalized absorbance of MPS-PPV and normalized fluorescent emission of DiD when embedded in a DPPC liposomes. Measurements were done in 10 mM HEPES buffer pH=7.3 and 150 mM NaCl and emission spectra were acquired upon excitation at 457nm.



### 3.2.6 MPS-PPV thermal sensitivity

We first initiated our study by choosing a type of liposomes that mimics cellular membranes. DPPC appeared to be the best candidate, first it has high transition temperature ( $T_m = 41\text{ }^\circ\text{C}$ ) and second it is highly abundant in some cellular membranes[65]. At room temperature, the membrane is gel-like and would transition into a liquid state when heated.[66] Indeed, the Fresnel normalized reflectivity for DPPC shows a total bilayer thickness of 5.6 nm at 25 °C which decreases to 4.8 nm at higher temperatures (55 °C). Close to the transition temperature, the electron density reveals an increase in roughness at the lipid-water interface and the bilayer is in the liquid disordered state [67].

We prepared DPPC liposomes of nano size (ca.225 nm) through a 200 nm pore size polycarbonate membrane using a mini-extruder in the presence of MPS-PPV. Then we subjected the prepared liposomes to an increase in temperature to study thermal response of MPS-PPV when encapsulated in DPPC hydrophobic core between 20.0 and 50.0 °C in a 5.0 °C increments. The complex emission showed a steady decrease with the increase in temperature (Figure 3.3). We believe this thermal actuation is the response to the change in the polymer micro-viscosity. In fact, the quantum yield temperature-dependency on viscosity is approximated by  $\phi = b(\eta/T)^x$  where b is constant, and x is the viscosity sensitivity of the conjugated polymers. DPPC viscosity has been estimated to decrease from 92 cP at 20.0 °C to 25 cP at 47 °C which would explain the observed fluorescent signal change[68]. The enhancement in intensity was accompanied with a red shift which is unusual in such cases. We hypothesise that there is a different interaction mechanism than what was mentioned previously.

Intensity reduction results weren't meaningful and wouldn't allow accurate interpretation due to the minimal reduction in the intensity that might be mistaken with photobleaching but more importantly the response wasn't ratiometric which makes our system prone to any external factor.

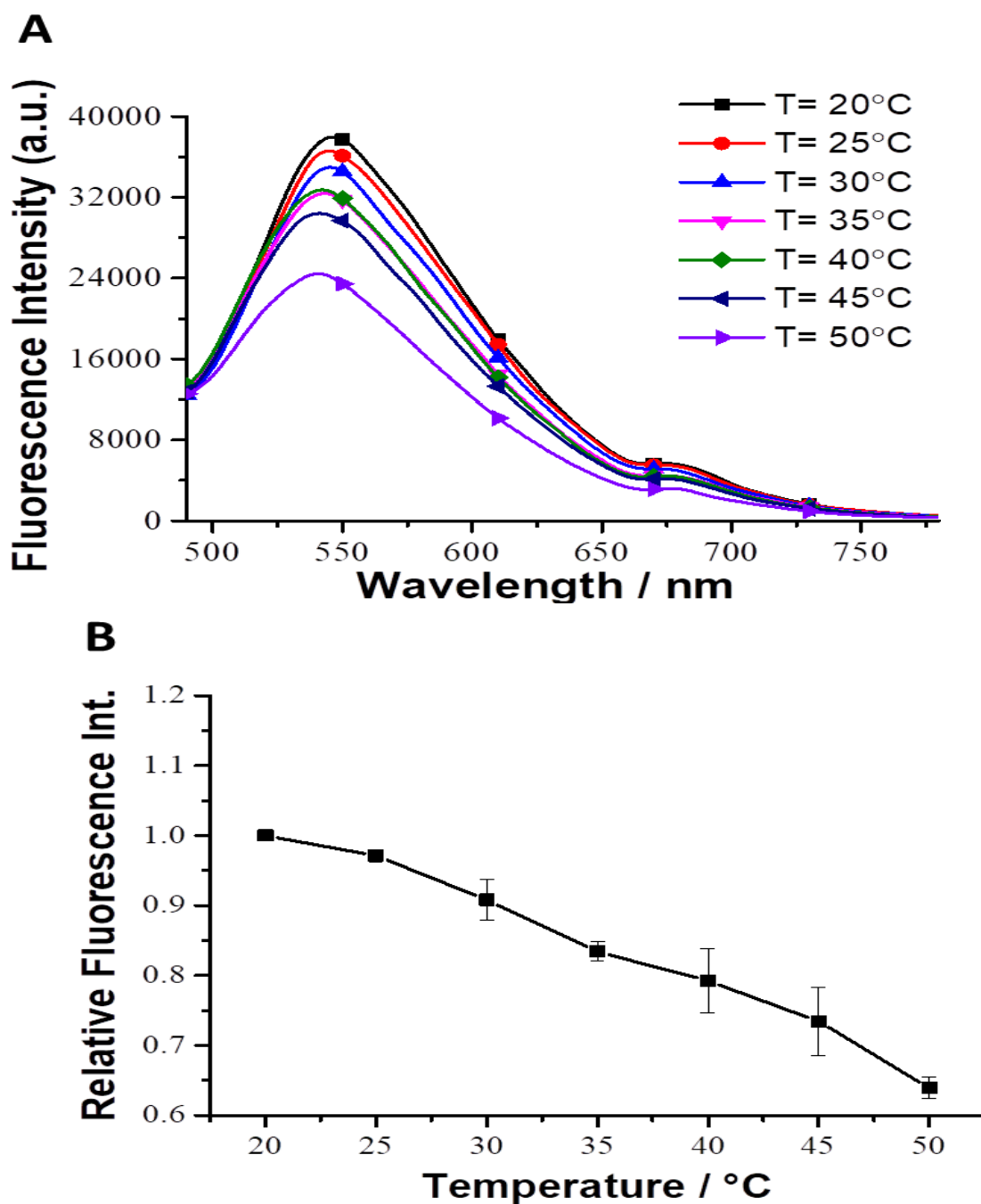


**Figure 3.3:** (A) Fluorescence emissions of DPPC/MPS-PPV measured between 20.0 °C and 50.0 °C at a 5.0 °C increments. (B) Normalized integrated fluorescent intensity extracted from A at different temperatures. The lines connecting the experimental p are for visual aid. Measurements were done in 10 mM HEPES buffer pH=7.3 and 150 mM NaCl and emission spectra were acquired upon excitation at 457 nm.

### 3.2.7 FRET-based Thermal Sensor

To overcome these two problems, we stained DPPC with DiD, a lipid-soluble dye. The utilization of guest induced-fluorescence resonance energy transfer (FRET) system having simplicity, sensitivity and dynamic range ought to be as a productive way to deal with ratiometric fluorescent probes[69]. DiD absorption overlaps with the emission of MPS-PPV allowing an efficient Förster resonance energy transfer (FRET) with a Förster radius ( $R_0$ ) of 4 nm. At room temperature, the calculated initial FRET was 0.55. As the temperature increases, the CPE emission increased concurrent with a decrease in the acceptor emission (Figure 3.4).

This resulted in a decrease in the calculated energy transfer, especially between 30 and 45 °C, before it stabilizes at a FRET value of 0.15 at high temperatures. At the highest temperature, the fluorescent intensity of the conjugated polyelectrolyte ( $2.2 \times 10^4$  a.u.) is comparable to that at the same temperature for DPPC/MPS-PPV alone ( $2.5 \times 10^4$  a.u.). We therefore, believe that the observed thermochromic change is not only due to the individual photophysical thermal response of the donor and acceptor (quenching of their signal) ( Figure 3.3 and 3.5) but also to structural changes.

As such, we speculate, as the temperature increases, the distance separating MPS-PPV and DiD changes as a result of the change in the DPPC viscosity, roughness and membrane thickness which might affect the position of the CPE within the membrane . To better understand and support our claims, we prepared liposomes with different viscosity and looked at the FRET-thermal response and how MPS-PPV embed itself in the membrane as the solution temperature changes.

To better understand and support our claims, we prepared liposomes with different viscosity and looked at the FRET-thermal response and how MPS-PPV embed itself in the membrane as the solution temperature changes.

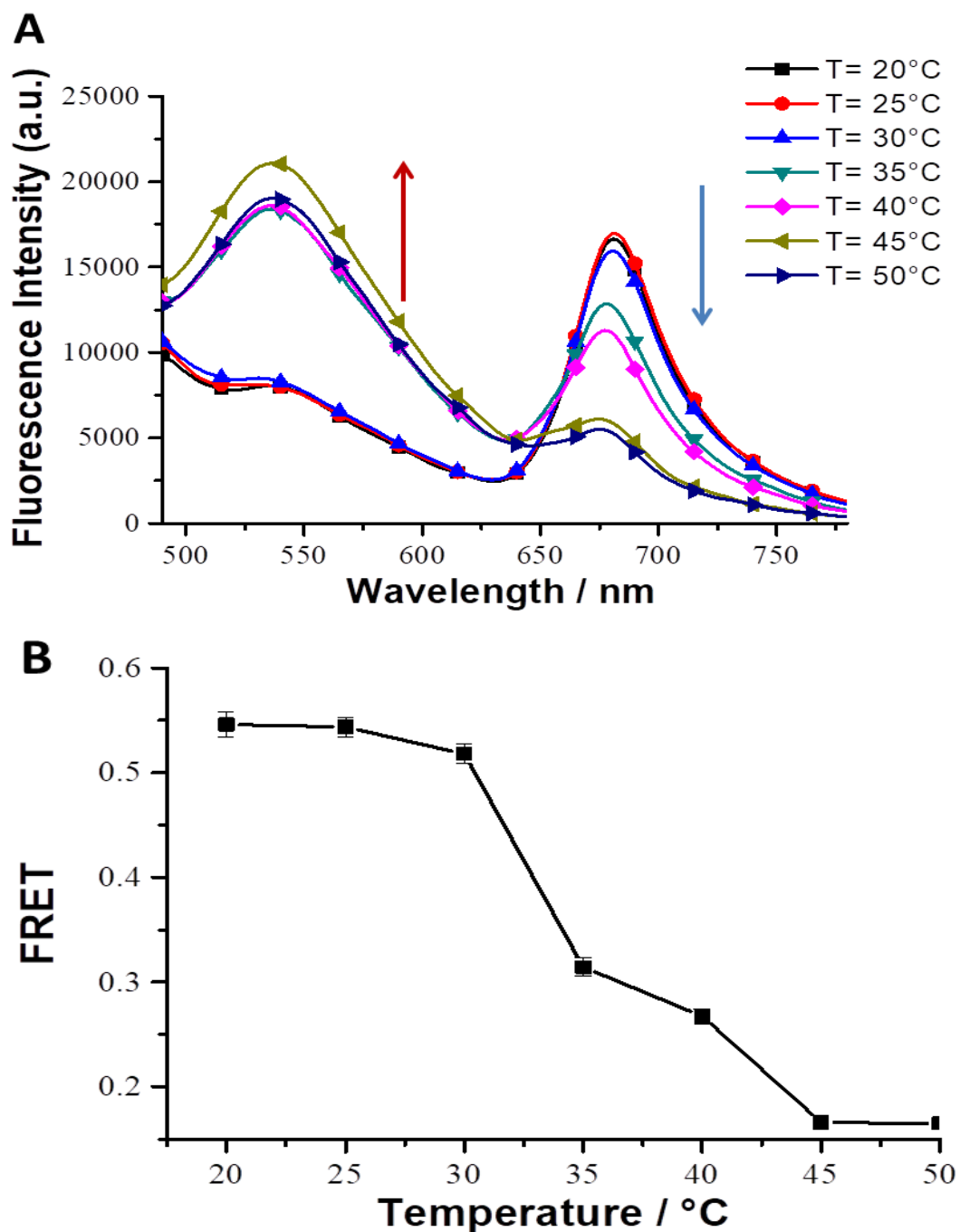


**Figure 3.4:** (A) Fluorescence emission of DPPC-DiD/MPS-PPV between 20.0 and 50.0 °C in a 5.0 °C increments. (B) Calculated FRET at different temperatures. The lines connecting the experimental points are for visual aid. Measurements were done in 10 mM HEPES buffer pH= 7.3 and 150 mM NaCl and emission spectra were acquired upon excitation at 457 nm.

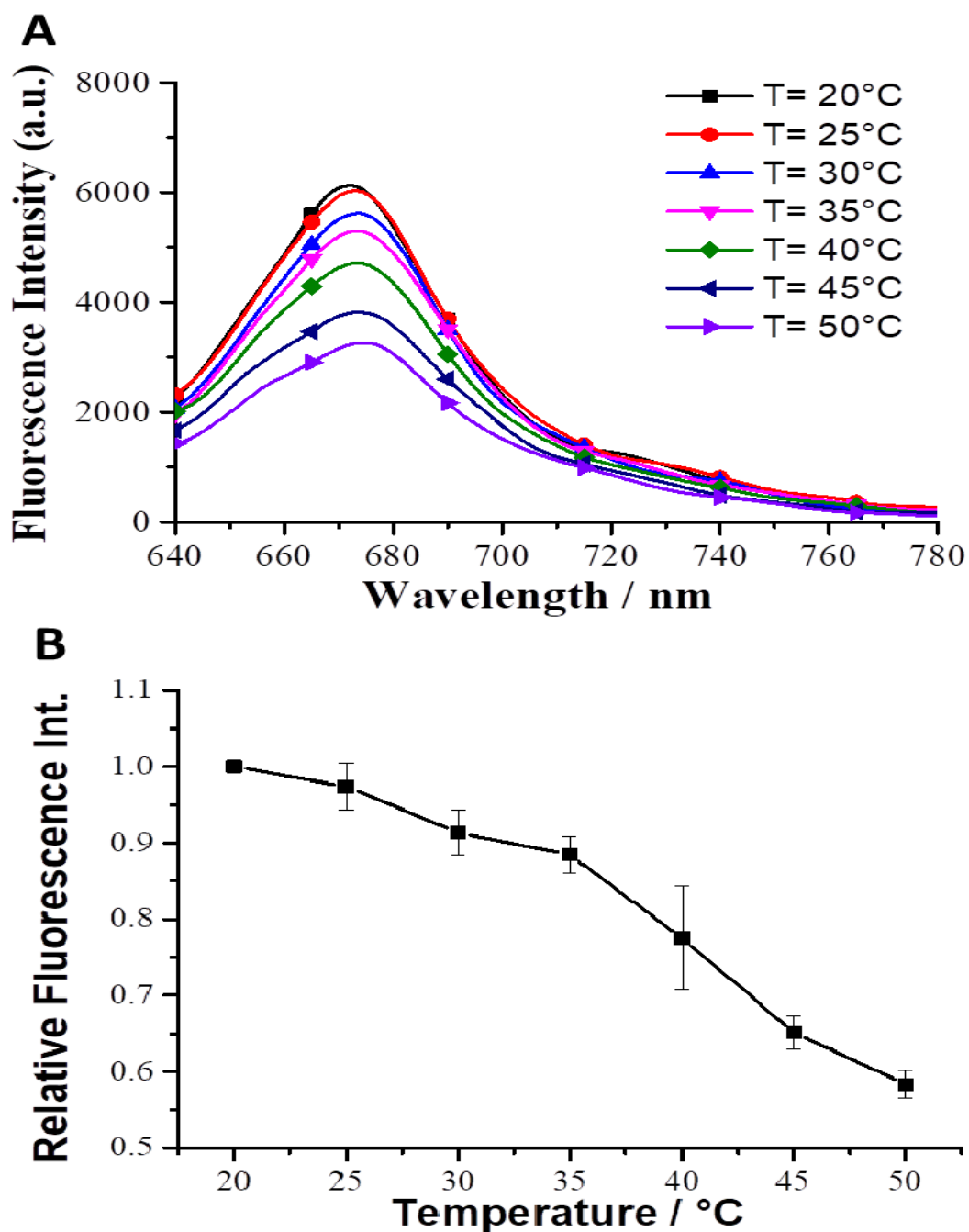


**Figure 3.5:** (A) Thermal response of DiD embedded in DPPC between 20 and 50 °C. (B) Relative change in fluorescent emission for three trials. Error bars are calculated from the standard deviations of three independent measurements. Lines connecting the experiment points are for visual aid only. Experiment was performed in 10 mM HEPES with 150 mM NaCl (pH= 7.3) buffer solution.

### ***3.2.8 Thermal Response at Different Lipid Viscosities***

Membrane fluidity is a physical property of cells, it's highly influenced by the membrane composition and whether the fatty acid is saturated or unsaturated. Viscosity which is another term for fluidity describes the movement and the of the proteins receptors, biomolecules within the membrane. Consequently, changes in membrane viscosity have been linked with alterations in physiological properties. Meaning that, any changes in the lipid membrane viscosity would lead to the CPE and lipophilic dye restructuring within the membrane which might result in changes in thermal fluctuations [70].

The effect of the membrane viscosity on the thermal fluctuation was tested by substituting DPPC with DOPC and introducing cholesterol to the DPPC bilayers. DOPC has a low transition temperature ( $T_m = -17\text{ }^\circ\text{C}$ ) which makes it liquid at room temperature and would mimic the DPPC viscosity at high temperature. As such, no viscosity-induced change in the MPS-PPV structure is expected with the increase in temperature. As seen in (Figure 3.6), with the increase in temperature, both the emission of MPS-PPV and DiD decrease. The result is consistent with the decrease in the fluorescent signal observed for both probes when individually prepared in DOPC and DPPC liposomes (Figure 3.7)



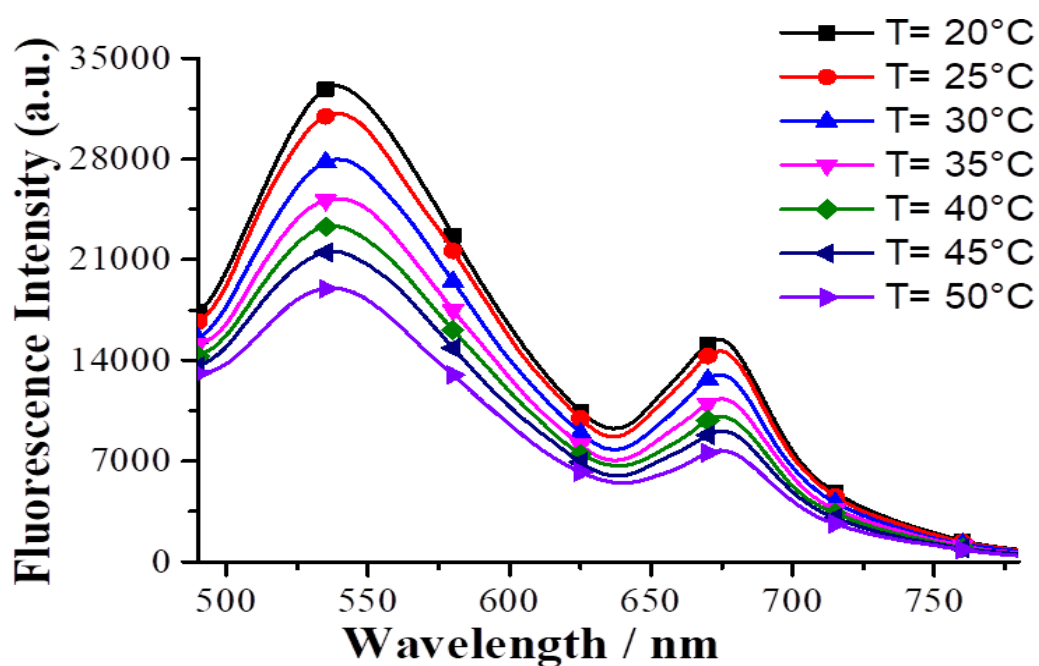


**Figure 3.6:** Fluorescence emissions of DOPC-DID/MPS-PPV between 20 and 50 °C in a 5 °C increments. Excited at 457 nm and collected between 490 and 780 nm. Lines connecting the experimental points are for visual aid only. Experiment was performed in 10 mM HEPES with 150 mM NaCl (pH= 7.3) buffer solution.

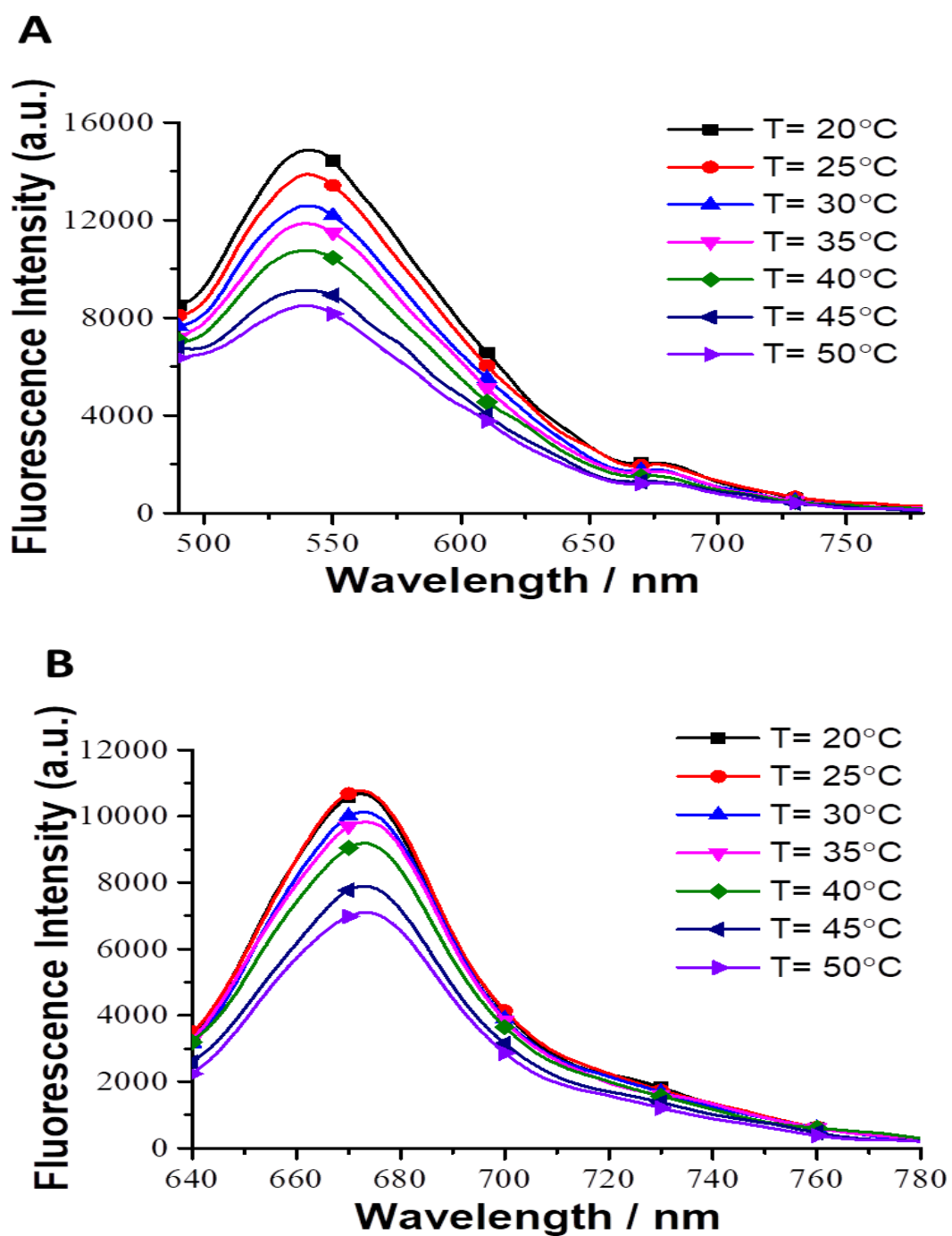


**Figure 3.7:** Fluorescence emission of (A) DOPC/MPS-PPV and (B) DOPC/DiD between 20 and 50 °C. Measurements were done in 10 mM HEPES buffer pH= 7.3 and 150 mM NaCl.

The effect of the membrane viscosity on the thermal fluctuation was also tested by introducing different amount of cholesterol to the DPPC bilayers. Cholesterol, in lipid membranes, regulates the membrane fluidity and its mechanical strength by controlling the lipid organization and phase behavior which result in decreasing its permeability. When Sanz *et al.* introduced Chol at a 10 % ratio to DPPC bilayer, they observed a phase separation of two domains with two distinct fluidity. Upon heating, the fluidity corresponding to each phase remained constant for the temperature range of 27–42 °C and merged at temperatures above 46 °C[71].

Herein, three DPPC lipid samples were prepared with increasing concentrations of cholesterol 0, 10 and 20 %. The liposomes were stained with MPS-PPV and DiD. The FRET was evaluated at room temperature and upon increasing the temperature at 5.0 °C increment. At room temperature, the initial FRET value decreased with increasing the cholesterol concentrations; For pristine DPPC liposomes, the original value was 0.55 and decreased to 0.45 and 0.40 with the increase in cholesterol concentrations from 0 to 10 and 20 % (Figure 3.8). In addition, the change in the thermal FRET response was much smoother with the increase in the % of cholesterol. These observations confirm the dependency of the FRET signal on the lipid membrane viscosity.

In addition to validating our hypothesis, the cholesterol plays an essential physiological role in thermal membrane response and its introduction could be extrapolated to future *in vivo* studies[72, 73].

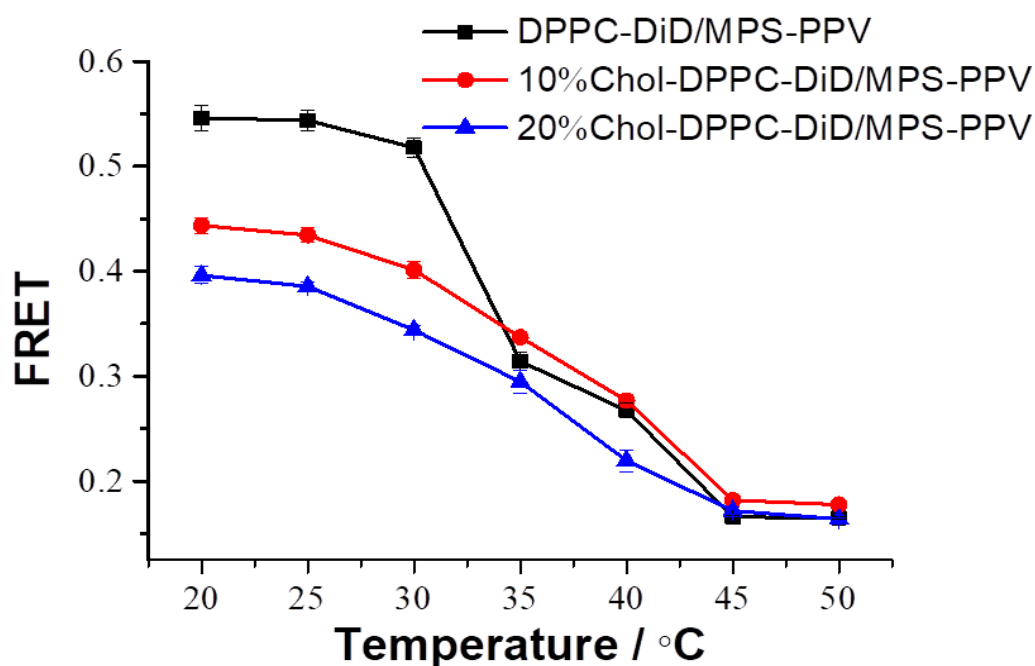


**Figure 3.8:** Calculated changes in FRET with increasing temperature as a function of cholesterol percentage in DPPC-DiD/MPS-PPV liposomes. Measurements were done in 10 mM HEPES buffer pH=7.3 and 150 mM NaCl and emission spectra were acquired upon excitation at 457nm. The lines connecting the experimental points are for visual aid.

To further validate our hypothesis, we compared measurements recorded in 1-palmitoyl 2-oleoyl phosphatidylcholine (POPC) and DOPC with 10% cholesterol. These lipid films are very close in molecular packing and organization. At room temperature, both lipid films had a low FRET value of around 0.24. With the increase in temperature, POPC and DOPC:Chol FRET values decreased similarly to approximately 0.20 (Figure 3.9). The experiments were performed under the same conditions as the previous experiments.

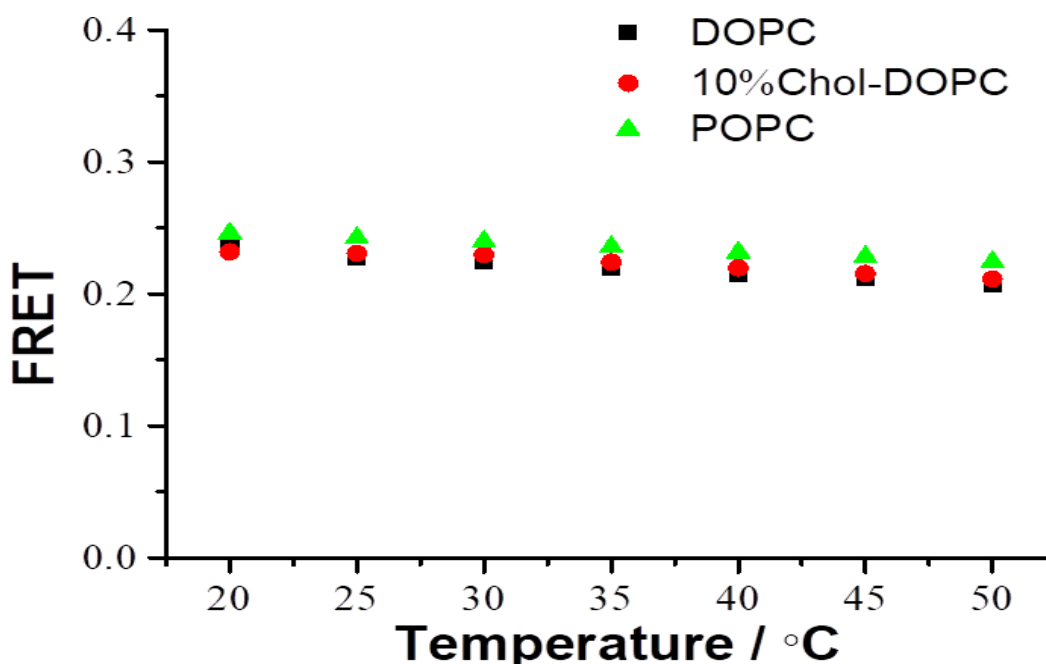


**Figure 3.9:** Calculated FRET 10 % Chol-DOPC and POPC and DOPC at different temperatures. Measurements were done in 10 mM HEPES buffer pH=7.3 and 150 mM NaCl and emission spectra were acquired upon excitation at 457nm.

### 3.2.9 MPS-PPV Signal Dependency on Membrane Positioning

To further validate the previous assumptions, MPS-PPV was added to either pre-formed DPPC or 20 % CHOLE-DPPC liposome solution. We argued that the cholesterol-containing liposomes will be less permeable to the addition of MPS-PPV given its effect on the lipid bilayers and would result in a lower fluorescent signal.

The initial measured intensity of the CPE, when added to pristine DPPC, was significantly higher than the less permeable liposome (Figure 3.10). In both cases, the fluorescence emission increased over time and was more pronounced in case of DPPC which might be due to easier diffusion of MPS-PPV into the hydrophobic core. When both mixtures were heated above the transition temperature, a higher fluorescent intensity was recorded in both samples. The cholesterol-containing liposomes signal, however, was significantly less than that of DPPC.

As such, we believe the actuating thermal response is based on the restructuring of the conjugated polyelectrolytes inside the hydrophobic core with the increase in temperature.

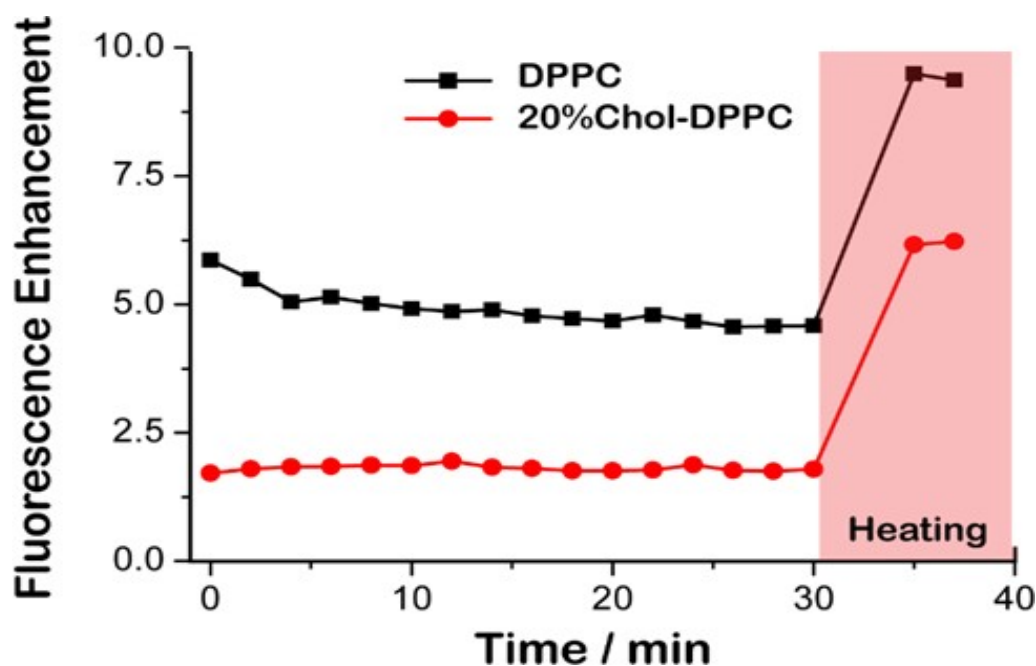


**Figure 3.10:** Fluorescence enhancement of MPS-PPV upon the addition of preformed liposomes of DPPC and 20 % Chol-DPPC over time. At the 30 min mark, the solution was heated to 50.0 °C above the DPPC transition temperature.

### 3.2.10 Thermal Response Reversibility

One of the limitations in polymer-based thermal probes that adversely affect their performance is hysteresis. To make sure our system doesn't suffer from such a drawback we recorded, different output signals for the same temperature value during a cycle of heating and cooling.[74]

In our case, the ratiometric response was independent of the cycling direction with signal repeatability 95% at 20.0 °C and 98.8 % at 50.0 °C. A careful look reveals that the emission intensity slightly change during the cooling run possibly due to polymer-CPE restructuring, but the ratiometric nature of the probe minimize the adversity of this effect.

We next investigated the probe stability by performing multiple testing runs. We recorded spectra at 20.0 °C and 50.0 °C (Figure 3.11). Over the 8 cycles, the probe ratiometric response showed high reversibility with revealing the lack of hysteresis and a great stability.

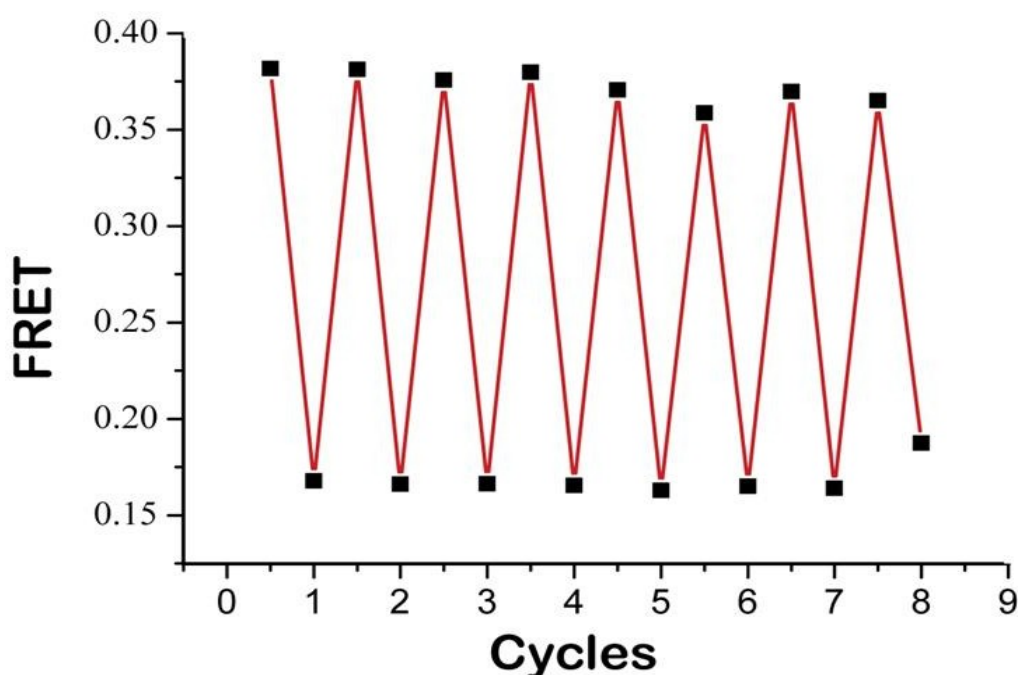


**Figure 3.11:** Reversibility of the calculated FRET signal upon heating DPPC-DiD/MPS-PPV liposomes between 20.0 °C and 50.0 °C. Measurements were done in 10 mM HEPES buffer pH= 7.3 and 150 mM NaCl and emission spectra were acquired upon excitation at 457 nm. The lines connecting the experimental points are for visual aid.

### 3.2.11 pH stability of the Thermal Probe

A major limitation that we encountered in our previously reported thermal probes prepared by complexing (poly(phenylene ethynylene) carboxylate) PPE-CO<sub>2</sub>-7 and PVP was its pH sensitivity which limited its applications to experiments under only controlled conditions.[75] In the current reported thermal probe, we argued that the lipid membrane would shield the conjugated polyelectrolytes from external solution conditions. As such,

the thermal response of DPPC-DiD/MPS-PPV was tested and compared under acidic, neutral and basic conditions (pH 5.2, 7.3 and 9.3). No change in the sensor thermal response was detected (Figure 3.12A). When a solution of only MPS-PPV was tested a 13.5 % in signal difference was detected between the 7.3 pH and that of 5.2 (Figure 3.12B) which indicate that the CPE is fully shielded by the lipid membrane. These results could aid in developing thermal sensors that could be used in vitro and in vivo studies where the experimental conditions are seldom well controlled.



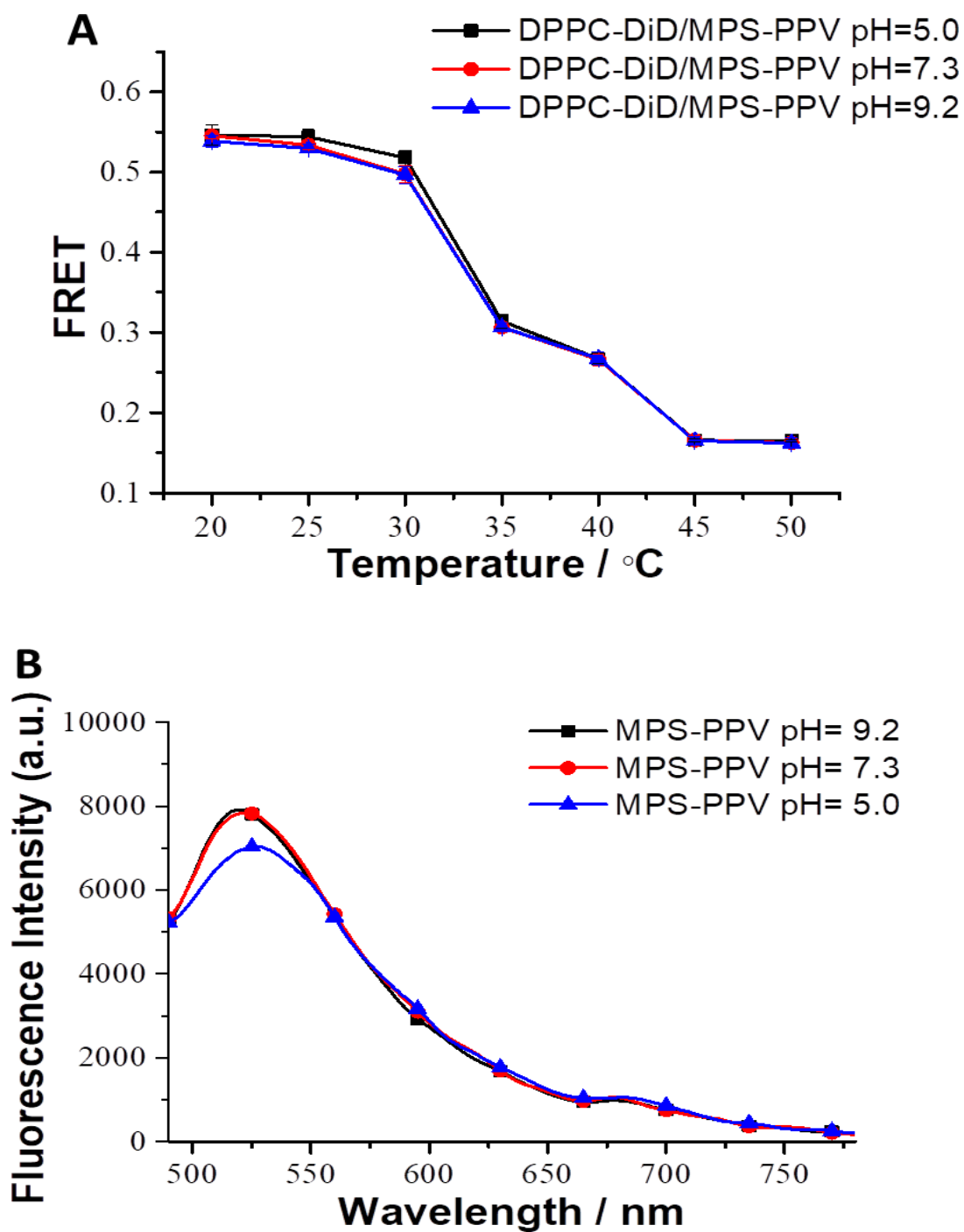


**Figure 3.12:** (A) Thermal response of DPPC-DiD/MPS-PPV at pHs 5.2, 7.3 and 9.0. (B) Emissions of MPS-PPV in basic (9.2), neutral (7.3) and acidic (5.0) mediums. Measurements were done in 10 mM HEPES buffer pH=7.3 and 150 mM NaCl and emission spectra were acquired upon excitation at 457 nm. The lines connecting the experimental points are for visual aid.

### **3.3 Conclusion**

In this chapter, we report on the thermal response of conjugated polyelectrolytes when embedded in a lipid membrane stained with an acceptor dye. The change in temperature restructured the polymer within the lipid membrane resulting in change in the measured FRET. The probe was also sensitive to the membrane fluidity with little effect from the external pH. This fluidity-dependent signal response might prove useful to assess lipid viscosity and to estimate transition temperatures of lipid mixtures. In addition, lipid membranes have been formulated into microscopic structures such silica beads and supported bilayers. The integration of our probes into such structures would allow probing local thermal changes at the meso- and macro-scale.

## CHAPTER 4

# FLUORESCENT THERMAL SENSING USING CONJUGATED POLYELECTROLYTES IN THIN POLYMER FILMS

### 4.1 Introduction

In recent years, many fluorescent based thermal sensors were developed to probe temperature fluctuations in solution and for sub-cellular applications [12, 49, 76]. However, very few reports have focused on measuring thermal variations in thin polymer films despite their use in subminiature micro-sensors such as gas sensors[77], wind sensors[78] and in many processed micro -materials such as micro-electro mechanical systems (MEMS); where thermal fluctuations play a pivotal role in their operation. Several researchers have conducted various studies on micro-heaters that use SiC [79], Pt [80-82], poly-Si [83] [79], single crystal silicon [83], and TiN [84] as the heating layer but these studies were fairly limited and didn't provide any information on the uniformity of temperature distribution and heat dissipation. Despite the fact that temperature is considered a significant component in their operation.

Thin polymer films are not only useful to measure temperature variations produced within those films but certainly to map heat generated in other solid substrates and at the interface between solids and liquids. Examples for such applications include but not limited to, microfluidic devices, microheaters, and microwell arrays where many chemical, physical and biological processes are currently being explored without accurately controlling the heat generated at the microscale[85]. Subsequently, few approaches have been invented such as traditional embedded thermocouples however; measurements are limited to single locations unless complex fabrication and data

acquisition is implemented for several thermocouples [86, 87]. Furthermore, on-chip micromachined sensor arrays made in glass[88] and nuclear magnetic resonance[89] have also been used, these methods are more efficient than the previous one. For instance, they provide noninvasive temperature measurement abilities however; they suffer from high equipment costs, complex fabrication processes, and implementation difficulties. A more advanced approach was introduced by McLennan *et al* by correlating metal resistance to temperature measurements. For instance, he has developed thin film thermistor consisting of a tin-selenide sensing material[90]. Similarly, Urban *et al.* used a thin film of amorphous germanium which yielded a high temperature sensitivity ( 2% per degree) and a fast response-time of 3 ms[91].

In spite of this progress but this field still fairly limited especially with advancement in nanotechnology and the need to use probes with high spatial resolution and high temperature sensitivity. The prompt development in fluorescent based sensing methodology made it an appealing approach to map thermal fluctuations within thin films. Where Aizawa *et al.* reported an effective sensor in thin films by measuring the fluorescence lifetime of Cr doped  $\text{Al}_2\text{O}_3$ [92]. In another example, a silica sol-gel matrix was embedded with the temperature sensitive probe rhodamine B and used to measure the surface temperature of MEMS micro hotplates[93]. Utilizing fluorescent polymers in the sensing scheme is an attractive methodology, due to the high spatial resolution, contactless measurement and the need for minimal signal calibration over time.

At this stage the unique set of photophysical properties that CPE exhibit including high conductivity,  $\pi$ -electron polarization, excitation and charge transport, variable band gap for light absorption and emission, and chemical sensitivity[94] made them ideal candidates for sensing applications. The interest in these Conjugated polyelectrolyte stems from

there sensitivity to their microenvironment and the effect of their structural conformation on their unique set of photophysical properties. Extensive research has been done to study and understand such properties. There are two types of energy transfer mechanisms that are controlled by the CPE degree of aggregation. Where a collapsed chain would be dominated by the through space energy transfer, that is characterized by low quantum yield and a red shifted emission, while the extended conformation is dominated by through bond energy transfer[95, 96]. As mentioned above presence of a surfactant would lead to dramatic changes in the spectroscopic properties of the CPE by affecting the CPE degree of aggregation [97]. For instance a surfactant would lead to a significant enhancement in the quantum yield mediated by the electrostatic and hydrophobic interactions between the surfactants and CPEs. Moreover the surfactant can diminish the interchain quenching energy transfer, and prevent the CPE polymer chain folding which will reduce the number of kink defects that serve as non-emissive recombination sites; hence there will be enhancement in the quantum yield[97].

Herein we aim to exploit PPE-CO<sub>2</sub>-7 (Figure 4.1) which is a short short phenylene-based CPE to build our thermal probe.

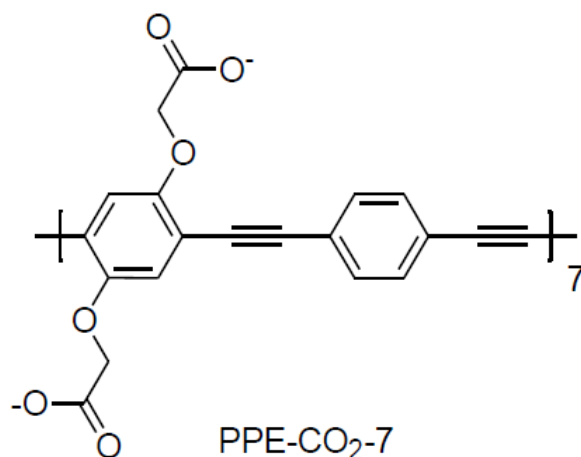


**Figure 4.1:** Schematic representation of the chemical structure referring to the short anionic conjugated polyelectrolyte poly (phenylene ethynylene) carboxylate with 7 repeating monomer-units (PPE-CO<sub>2</sub>-7)

Despite their exceptional characteristics, CPEs, such as PPE-CO<sub>2</sub>-7, still suffer from low photostability, photodegradation, blinking, and fast irreversible photobleaching. Therefore, their usages in sensing applications where the above drawbacks are essential limit their efficiency[98].

#### 4.1.1 Polyvinylpyrrolidone (PVP)

To overcome the above mentioned limitations we decided to complex the CPE with another polymer of desired properties. Our laboratory has previously reported on the thermal sensitivity of short conjugated polyelectrolytes (CPEs), specifically poly(phenylene ethynylene) (PPE-CO<sub>2</sub>-7) when complexed to an amphiphilic polymer, polyvinylpyrrolidone (PVP)[88]. When PVP was used as a scaffold for the CPE, it tends to extend the latter's backbone and prevent photodegradation. This polymer also led to a 23-fold increase in the quantum efficiency of the CPE. The probe showed excellent sensitivity between 10 °C and 90 °C and a high relative sensitivity of 2.7% at 35 °C. A suggested speculation is that in the presence of PVP, the PPE-CO<sub>2</sub>-7 aggregates are destabilized and the change in the solution temperature disaggregates the CPE chains in the excited

state[99]. As a result, the emission spectra shifted between 520 nm and a brighter peak at 450 nm. The nanothermometer ratiometric signal was reversible with fast response time. The probe also showed an excellent thermal response in hydrogel materials specifically agarose and agar resulting in a respective maximum relative sensitivity of 2.0% and 1.9% at 45.0 °C[100].

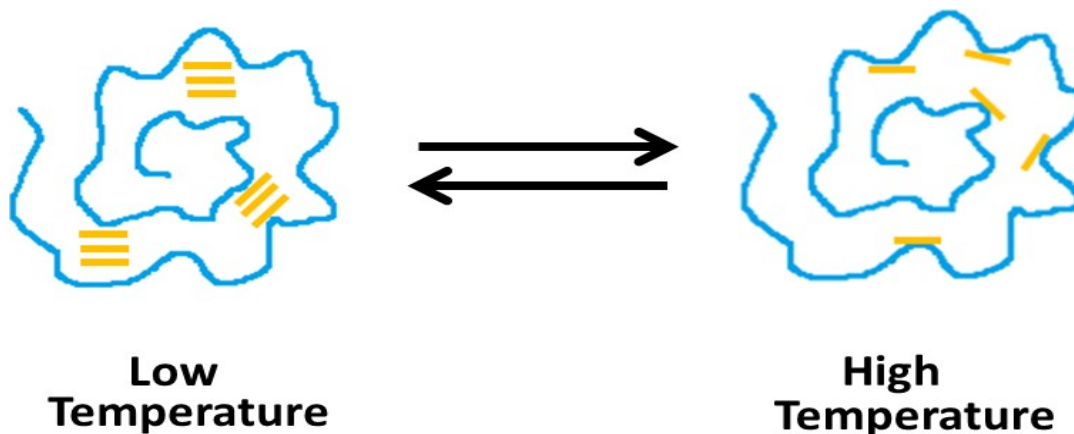


**Figure 4.2:** Schematic representation of the complexation between PVP and PPE-CO<sub>2</sub>-7 (—) at low and high temperature. (Reprinted with permission from *Ghenwa et al.*) [100]

After revealing the importance of the PVP backbone in the thermal response of PPE-CO<sub>2</sub>-7 we decided to expand our probe through introducing two PVP derivatives poly(vinylpyrrolidone)-co-vinyl acetate (PVP-VA) and polyvinylpyrrolidone polystyrene (PVP-PS) (Figure 4.3). Various reasons were behind choosing those two derivatives. The main reason was the PVP backbone they possess which appeared to be an important factor in the sensing response of the CPE, and (2) both could be prepared into thin films by a simple spin-coating technique[101]. Particularly, PVP-VA is known for its high binding affinity and film formation on both hydrophobic and hydrophilic surfaces. PVP-VA is also a good insulator which would be excellent for thermal sensing application in electronic devices[33]



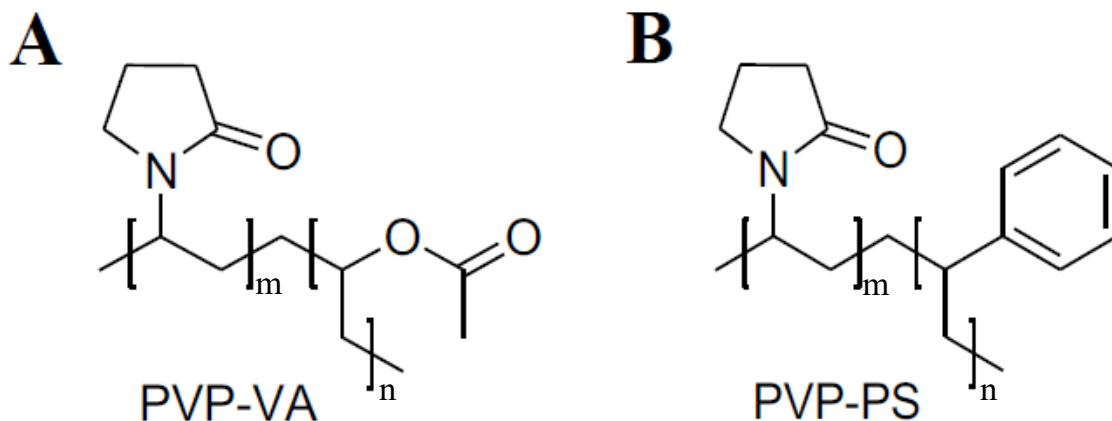


**Figure 4.3:** Schematic and chemical structure of the amphiphilic polymers (A) poly(vinylpyrrolidone)-co-vinyl acetate (PVP-VA) and (B) polyvinylpyrrolidone polystyrene (PVP-PS)

Herein we aim in this chapter to monitor the thermal variations within polymer thin films by building a ratiometric thermal probe based on a conjugated polyelectrolyte molecule poly-(phenylene ethynylene) (PPE-CO<sub>2</sub>-7). This nanothermometer was first optimized in solution by testing two polyvinylpyrrolidone (PVP) copolymers (co-vinyl acetate (VA) and co-polystyrene (PS)). It was then spun cast onto quartz slides and mixed with Rhodamine B. The fluorescence signal was quantified with the change in temperature using a DSLR camera.

## 4.2 Thermal Sensing

To evaluate the thermal response of the polymer complex, the solution mixture was subjected to a gradual increase in temperature between 15.0 - 70.0 °C with a 5.0 °C increment.

Analyzed PVP-VA sample contains: 10 mM HEPES-150 mM NaCl mixture, 22 μL PPE-CO<sub>2</sub>-7 (450 μg/mL), and PVP-VA yielding a final concentration = 6.17 μg/mL of PVP-VA

Analyzed PVP-PS sample contains: 10 mM HEPES-150 mM NaCl mixture, 22  $\mu$ L PPE-CO<sub>2</sub>-7 (450  $\mu$ g/mL), and PVP-PS yielding a final concentration in cuvette = 19.45  $\mu$ g/mL of PVP-PS.

### 4.3 Reversibility and Cycling

To check for the reversibility of our proposed system, the PPE- CO<sub>2</sub>-7/polymer mixture was cycled 10 times between 20.0 and 70.0 °C.

Analyzed PVP-VA sample contains: 10 mM HEPES-150 mM NaCl mixture, 22  $\mu$ L PPE-CO<sub>2</sub>-7 (450  $\mu$ g/mL), and 6.17  $\mu$ g/mL PVP-VA.

Analyzed PVP-PS sample contains: 10 mM HEPES-150 mM NaCl mixture, 22  $\mu$ L PPE-CO<sub>2</sub>-7 (450  $\mu$ g/mL), and 19.45  $\mu$ g/mL PVP-PS.

## 4.4 Results and Discussion

### 4.4.1 Absorbance Spectra

We initiated our study by exploring the spectroscopic properties of PPE-CO<sub>2</sub>-7 in solution upon its complexation with the PVP copolymers. When PPE-CO<sub>2</sub>-7 was mixed with either PVP-VA or PVP-PS, a slight red shift in the absorbance was observed (Figure 4.4). This is due to an extension in the CPE conjugation upon favorable complexation with the copolymers. The addition of PVP-PS particle lead to the appearance of a scattering tail which was also apparent when fluorescent measurements were later acquired.

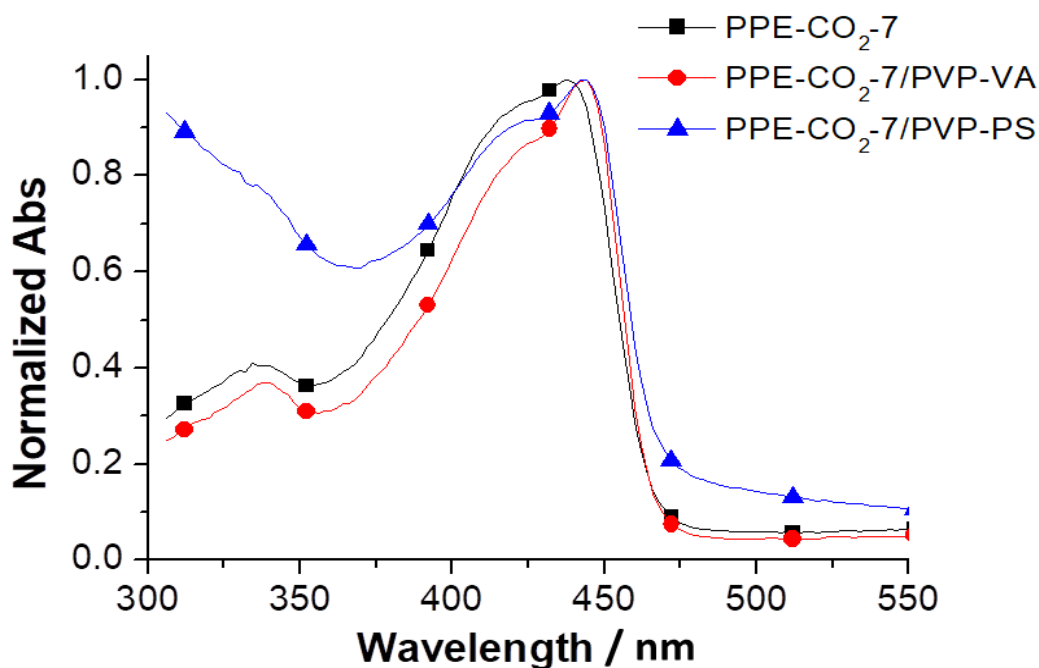


**Figure 4.4:** (A) Chemical Structures of poly (phenylene ethynylene) with 7 repeating units on average (PPE-CO<sub>2</sub>-7), poly(vinylpyrrolidone)-co-vinyl acetate (PVP-VA) and poly(1-vinylpyrrolidone-co-styrene) (PVP-PS). (B) Absorbance spectra of PPE-CO<sub>2</sub>-7 (■), PPE-CO<sub>2</sub>-7/PVP-VA (●) and PPE-CO<sub>2</sub>-7/PVP-PS (▲).

#### 4.4.2 Titrations

We then aimed to identify the concentration at which the copolymers would destabilize the PPE-CO<sub>2</sub>-7 aggregates at room temperature. As such, when the complex is heated and the CPE chains are fully disaggregated, a new peak at 490 nm should appear and increases in intensity as copolymers concentration increases. To a solution of PPE-CO<sub>2</sub>-7, an incremental amount of PVP-VA or PVP-PS was added at a constant temperature of 20 °C and continuously excited at 420 nm.

Upon the addition of PVP-VA the fluorescent emission shifted to a lower wavelength (blue shift) with a slight increase in intensity. Moreover, as the amount of the copolymer increases the non-aggregated emission peak at 450 nm became more apparent concomitant with the decrease in the aggregated intensity at 550 nm (Figure 4.5A).

This behavior was similar to what we have previously observed and reported for PVP polymers when added to PPE-CO<sub>2</sub>-7. PVP-PS addition did induce a blue shift in the fluorescent signal however a decrease in the signal was observed with the increase in the added polymer concentration (Figure 4.5B). We speculate that this might be due to the scattering of the PVP-PS suspension. To assess the thermal sensitivity of the PPE-CO<sub>2</sub>-7/copolymers, we chose the concentration at which the emission of the CPE is blue shifted, and the 450 nm peak is barely apparent; that corresponded to 6.17 µg/mL and 19.45 µg/mL for PVP-VA and PVP-PS respectively.

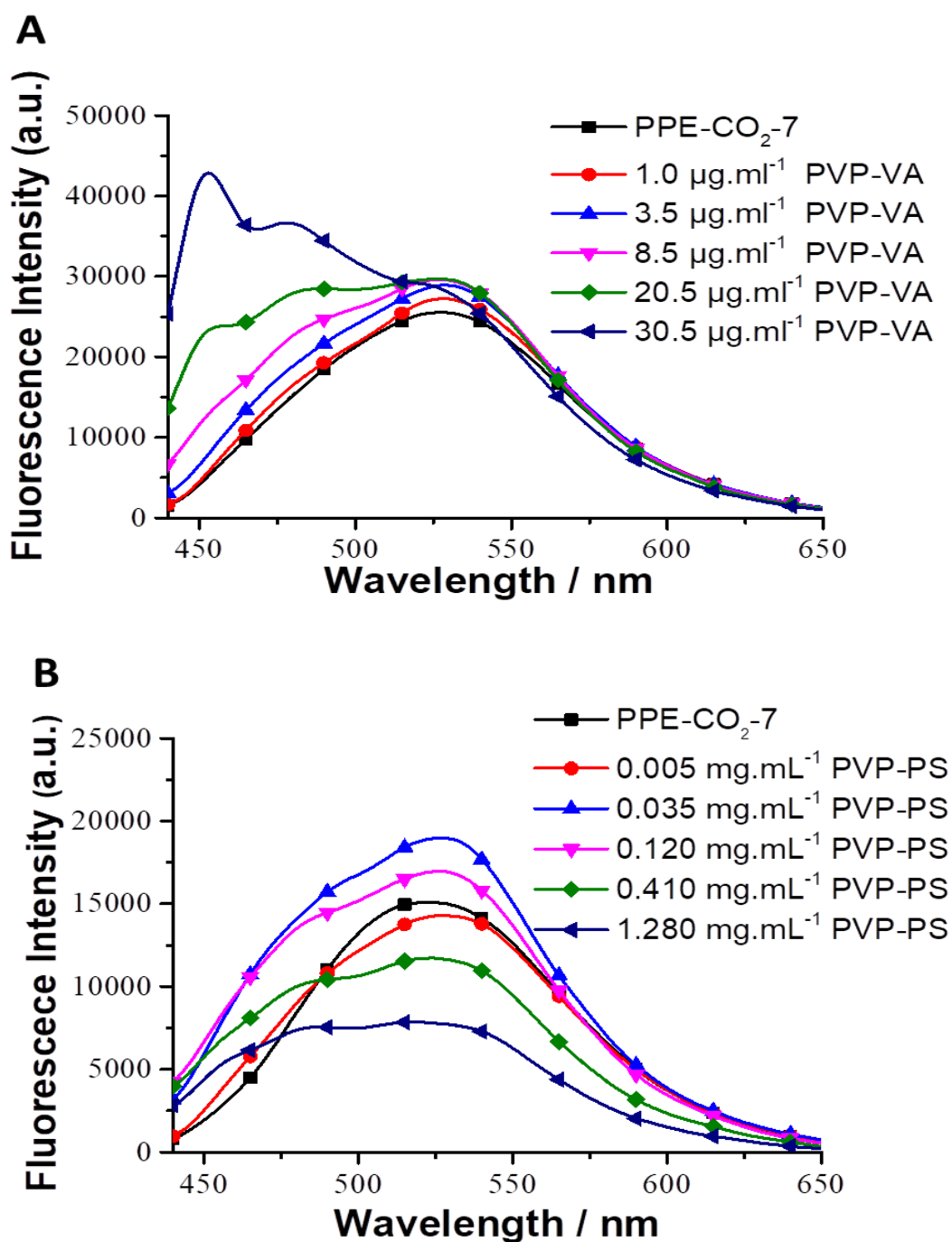


**Figure 4.5** : Fluorescent Emission Spectra of PPE-CO<sub>2</sub>-7 (5 µg/mL) upon addition of incremental amounts of (A) PVP-VA and (B) PVP-PS acquired at 20.0 °C in 10 mM HEPES and 150 mM NaCl when excited at 420 nm

#### 4.4.3 Thermal Sensing

After obtaining the critical concentration from the titration experiment, the thermal sensitivity of the probe was assessed. Therefore, the PPE- CO<sub>2</sub>-7/PVP-VA or PPE-CO<sub>2</sub>-7/PVP-PS to an incremental temperature increase between 15 °C and 70 °C at 5 °C steps and tracking the emission shift from the green to the blue emission region. The emission spectra were recorded after 5 minutes of stabilization.

For PVP-VA, a clear shift in the fluorescent emission was recorded from the destabilized state to the single chain peak at 450 nm with the increase in temperature (Figure 4.6A). PVP-PS, on the other hand, did not show a clear shift nor an increase at the 450 nm peak (Figure 4.7A).

To evaluate the probe's thermal sensitivity, the ratiometric signal was calculated by first integrating the intensity between 435 nm and 500 nm (*I*<sub>Blue</sub>) and from 500 nm to 650 nm (*I*<sub>Green</sub>) and then plotting the ratio  $Q = \frac{I_{Blue}}{I_{Green}}$  versus the temperature changes. The reported graphs correspond to the average of the integrated ratios of the three independent measurements (Figure 4.6B and 4.7B).

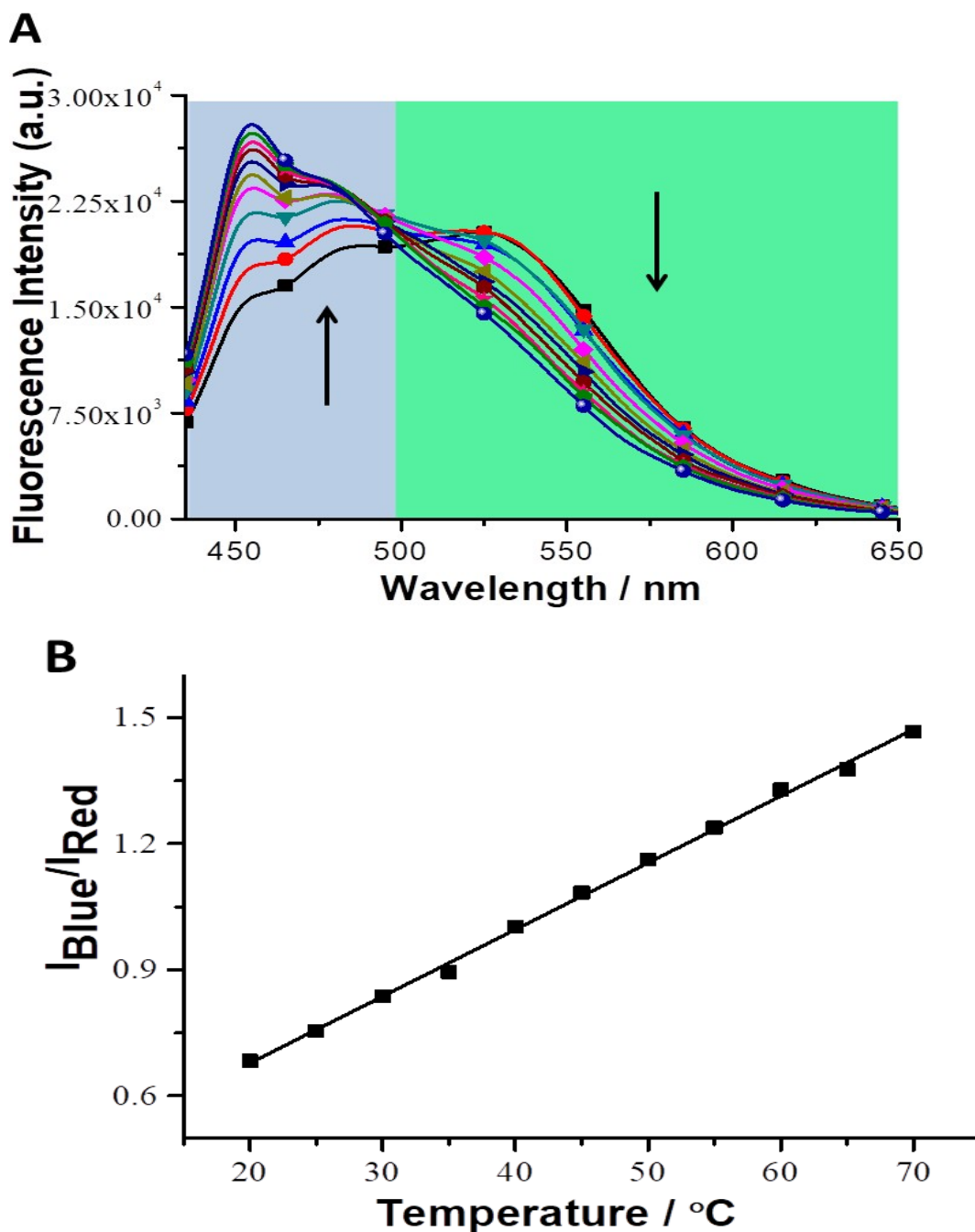


**Figure 4.6:** (A) Thermal response of PPE-CO<sub>2</sub>-7 (5  $\mu\text{g}/\text{mL}$ ) in complexation with PVP-VA (6.17  $\mu\text{g}/\text{mL}$ ) prepared in 10mM HEPES with 150 mM NaCl (pH=7.3) buffer solution, upon exciting at 420nm acquired between 15.0°C and 70.0°C, with 5°C increment (B) Average Integrated Fluorescent ratio, Q, of the blue region before ( $I_{blue}$ ), to the green region ( $I_{green}$ ) after the iso-emission point at 500 nm versus the temperature acquired between 20.0 °C and 70.0 °C- 5.0 °C increment.

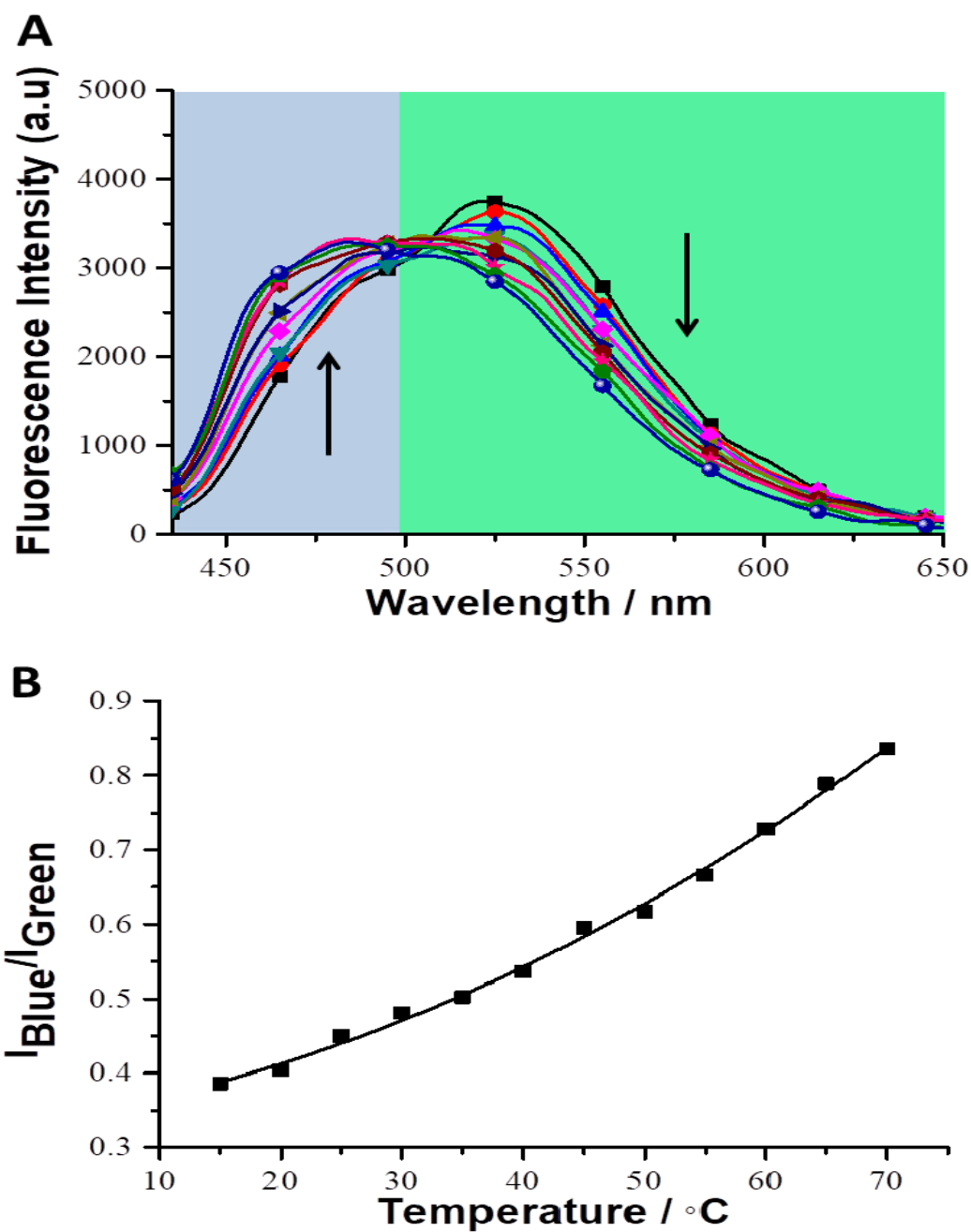


**Figure 4.7:** (A) Thermal response of PPE-CO<sub>2</sub> (5 μg/mL) in complexation with PVP-PS (19.45μg/mL) prepared in 10mM HEPES with 150 mM NaCl (pH=7.3) buffer solution, upon exciting at 420nm acquired between 15.0°C and 70.0°C, with 5°C increment. (B) Average Integrated Fluorescent ratio, Q, of the blue region before (I<sub>blue</sub>), to the green region (I<sub>green</sub>) after the iso-emission point at 500 nm versus the temperature acquired between 20.0 °C and 70.0 °C - 5.0 °C increment.



#### 4.4.4 *Relative Sensitivity*

The relative sensitivity in the solution for PPE-CO<sub>2</sub>-7/PVP-VA (Figure 4.8A) and PPE-CO<sub>2</sub>-7/PVP-PS (Figure 4.7B) were calculated using the equation below:

$$\left( \%S = \frac{dQ}{\partial T} \times 100 \right)$$

The respectively calculated sensitivities for PVP-VA and PVP-PS were 2.35% and 1.455% (Figures 4.8A and 4.8B). The PVP-VA sensitivity is comparable to our reported value for PVP alone in solution while that of PVP-PS is relatively low. The lower sensitivity led us to focus only on the PVP-VA.

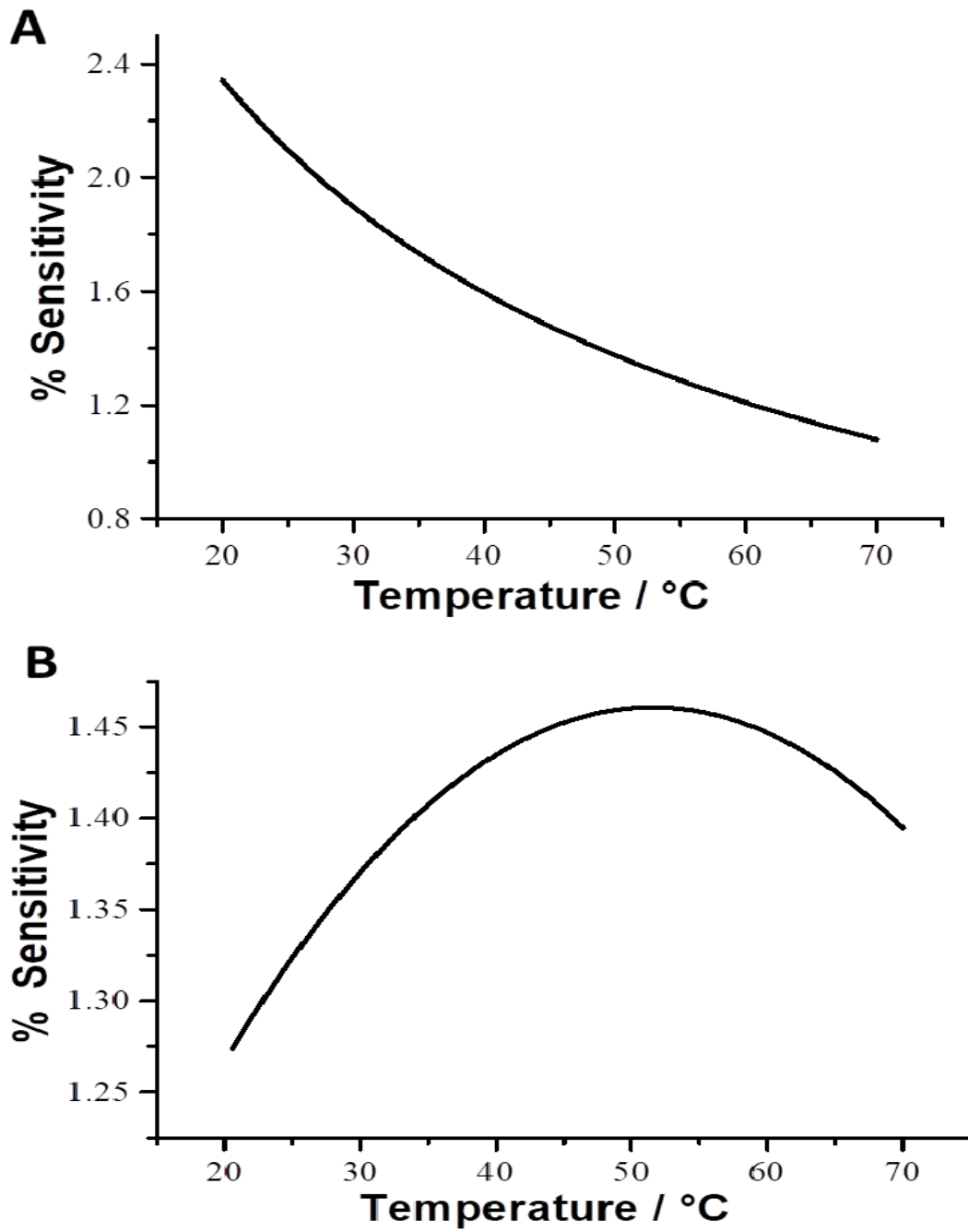


**Figure 4.8:** The relative sensitivity (% S) calculated from the thermal response ratio  $I_{\text{blue}}/I_{\text{green}}$  of (A) PPE-CO<sub>2</sub>-7/PVP-VA and (B) PPE-CO<sub>2</sub>-7/PVP-PS.

#### 4.4.5 Reversibility and Cycling

Polymeric probes tend to suffer from hysteresis, which leads to irreversibility in their fluorescent signal. To make sure that our probe is not limited by such a drawback, we tested for its reversibility upon cycling between low and high temperature 15 °C and 70 °C for 3-4 hours.

A solution of PPE-CO<sub>2</sub>-7/PVP-VA was cycled multiple times between 20 °C and 70 °C and then the ratio  $I_{\text{blue}}/I_{\text{green}}$  was calculated and plotted (Figure 4.9). Over the 10 cycles, the thermal probe response was reversible with no observed hysteresis and a small signal deviation of 2.5 % reflecting its stability over the 3-4 hours experimental window. PVP-PS has shown similar results (Figure 4.10).

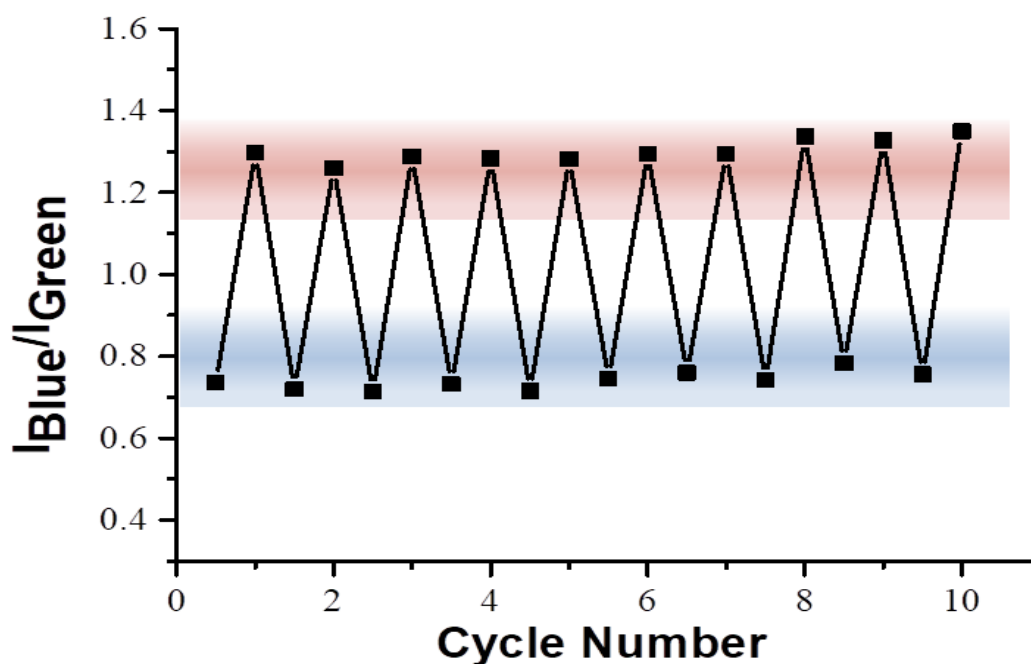


**Figure 4.9:** Cycling PPE-CO<sub>2</sub>-7 (5 µg/mL)/PVP-VA (6.17 µg/mL) between 20.0 °C (blue shade/Bottom) and 70.0 °C (red shade/Top). Lines connecting the experimental points are for visual aid only. The experiment was performed in 10 mM HEPES with 150 mM NaCl (pH=7.3) buffer solution, and the solution was kept to stabilize for 5 min before each measurement .

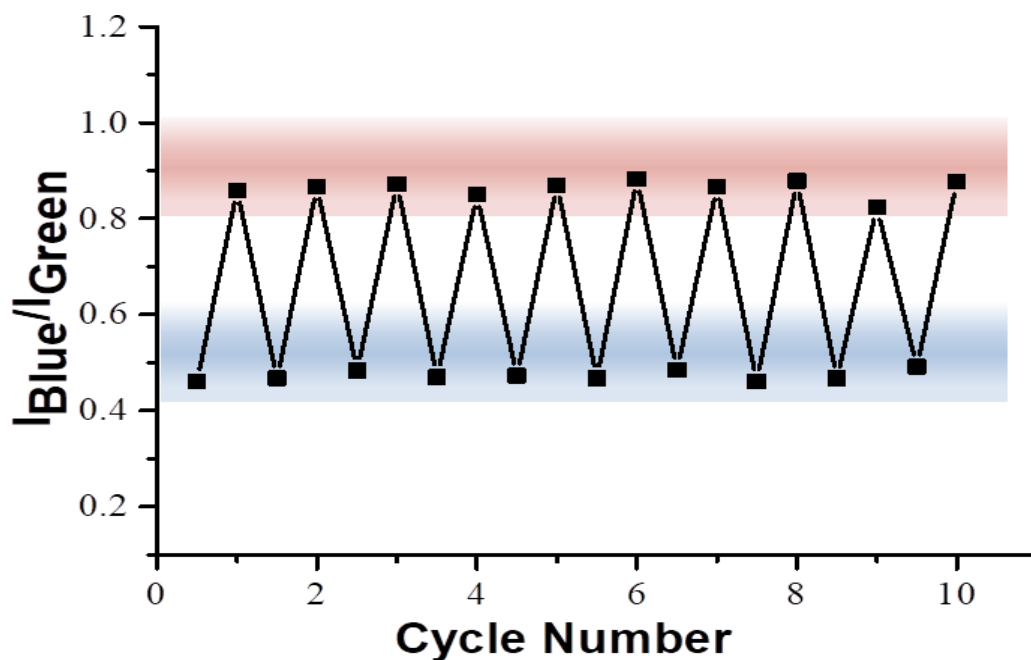


**Figure 4.10:** Cycling of PPE-CO<sub>2</sub>-7 (5  $\mu\text{g}/\text{mL}$ )/PVP-PS (19.45  $\mu\text{g}/\text{mL}$ ) between 20.0°C and 70.0 °C, with its respective fluorescent emission spectra. Lines connecting the experimental points are for visual aid only. The experiment was performed in 10 mM HEPES with 150 mM NaCl (pH=7.3) buffer solution, and the solution was kept to stabilize for 5 min before each measurement.

#### 4.4.6 *Thin Polymer Film Assembly*

##### 4.4.6.1 Thermal Imaging of PPE-CO<sub>2</sub>/PVP-VA Films

After optimizing our system and tracking its thermal response in solution, we moved to explore the thermal response of our nanothermometer in thin films. The CPE and PVP-VA mixture was spun cast onto quartz. The ratio of the two polymers was kept equal to that optimized in solution. In this experiment we adopted the same experimental setup used by Darwish *et al* [100].

The excitation was done using a UV-lamp (365 nm), and the detection was recorded with a regular DSLR Canon 750D camera- 60mm macro lens- (exposure time 1/5 s, f/5.6, ISO 100). (Figure 4.10) summarizes the collected images between 20 °C and 50 °C. To the naked eye, a slight change in the fluorescent emission is observed. The region of interest was selected and further analyzed using ImageJ to extract the average green and blue intensity channel since the ratiometric windows overlap those channels of the DSLR CMOS detector. Upon increasing the temperature, an increase in intensity was observed in both channels with a slightly more pronounced increase in the green window (Figure 4.11)

This behavior has been observed in solution at high PVP-VA concentration, where the PPE-CO<sub>2</sub>-7 has been fully disaggregated by the polymer and an increase in temperature results in an overall increase in fluorescent intensity. We believe in the film preparation process; the drying step is disaggregating the CPE chains and the viscosity of its microenvironment increased significantly after the drying process, which will hinder the aggregation of the CPE as the temperature increase.

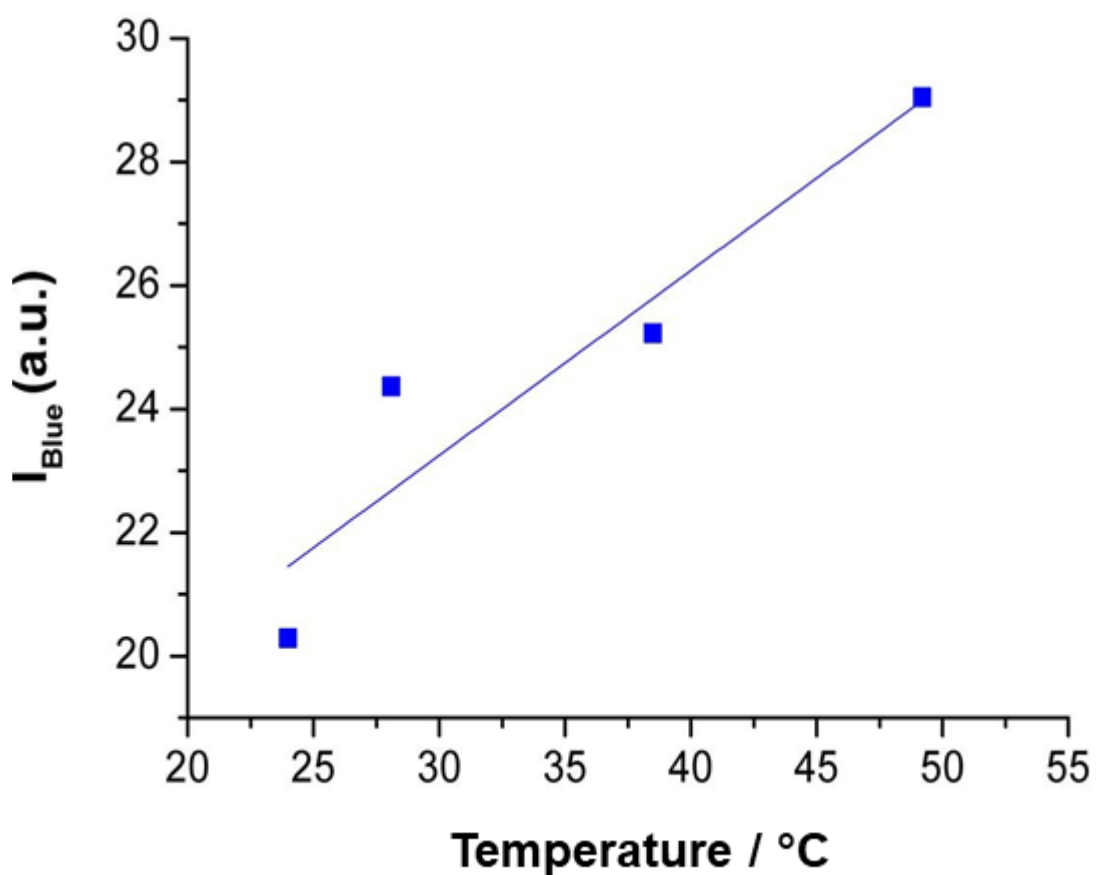
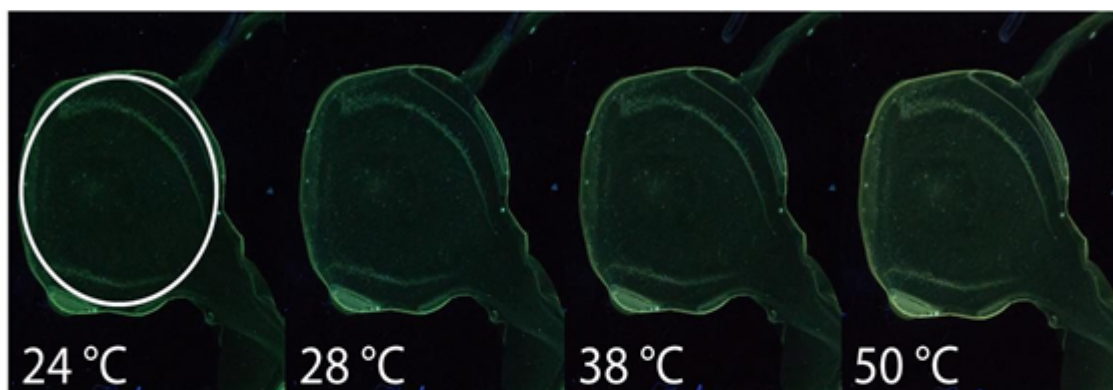


**Figure 4.11:** (A) Sequential images acquired using a DSLR camera upon exciting a film of PPE-CO<sub>2</sub>-7/PVP-VA using a UV lamp when placed on a Peltier heater. The circle highlights the analyzed region of interest. (B) Average fluorescent intensity obtained by dissecting the images in (A) into their RGB components and plotting the blue channel intensity versus the measured temperature.

#### 4.4.6.2 Thermal Imaging of Rh/PPE-CO<sub>2</sub>-7/PVP-VA

While the ratiometric signal was not attainable in the prepared films, the increase in signal is still advantageous compared to the traditional fluorescent dye thermal response which decreases with the temperature increase making it difficult to decouple it from photobleaching. The fluorescent-based method can be expanded to three-dimensional imaging and spatial resolutions down to a few nms.

To add a second layer of certainty to our thermal measurements in thin films, we introduced a temperature sensitive dye Rhodamine B. The same procedure was followed, and a mixture of PPE-CO<sub>2</sub>-7/PVP-VA and Rhodamine B was spun cast onto a quartz glass. Images were acquired upon excitation with a UV lamp (365 nm) and later analyzed with ImageJ (Figure 4.12). When the intensity in the three channels (green, blue and red) was deconvoluted, we observed an increase in the blue channel consistent with the previous result of PPE-CO<sub>2</sub>-7 alone. The red channel which captures photon between ca. 600 nm and 850 nm and overlaps Rhodamine B emission, revealed a decrease in fluorescent intensity over the same tested temperature window. The ratio of the average intensity of the two channels gave a linear thermal response with a slope of 0.010. The addition of Rhodamine B has allowed us to obtain a ratiometric thermal response in thin polymer films when imaged with a regular DSLR camera.

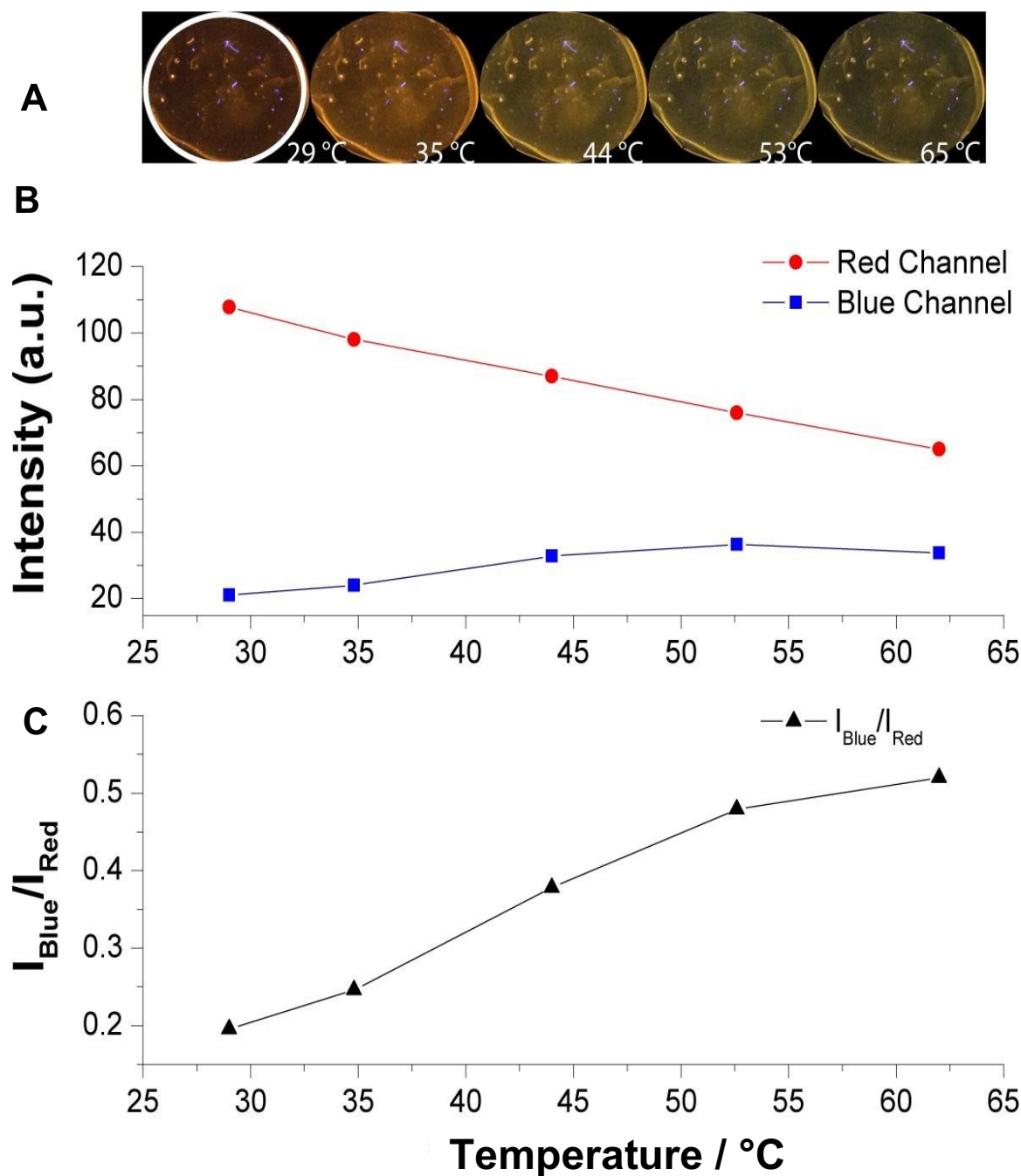


**Figure 4.12:** Sequential images acquired using a DSLR camera upon exciting a film of PPE-CO<sub>2</sub>-7/PVP-VA + Rhodamine B using a UV lamp when placed on a Peltier heater. The circle highlights the analyzed region of interest. (B) Average fluorescent intensity obtained by dissecting the images in (A) into their RGB components and plotting the red and blue channel intensities versus the measured temperature. (C) The ratio of the average intensities of the two channels plotted in (B) versus the measured temperature.



#### 4.4.6.3 Thermogravimetric Analysis (TGA)

For the thermogravimetric analysis, a Netzsch TG 209 F1 Libra instrument was used. The samples were first dried overnight and then analyzed between 30 °C and 1100 °C (but only reported until 600 °C) at a heating rate of 10.0 °C/min. PVP-VA/ PPE-CO<sub>2</sub>-7, and PVP-VA/ PPE-CO<sub>2</sub>-7/Rhodamine B. The results show that both co-polymers are stable up to temperatures around 300 °C. PPE-CO<sub>2</sub>-7 polymers are stable up to 800 °C. Rhodamine B seems to degrade at temperature above 100.0 °C

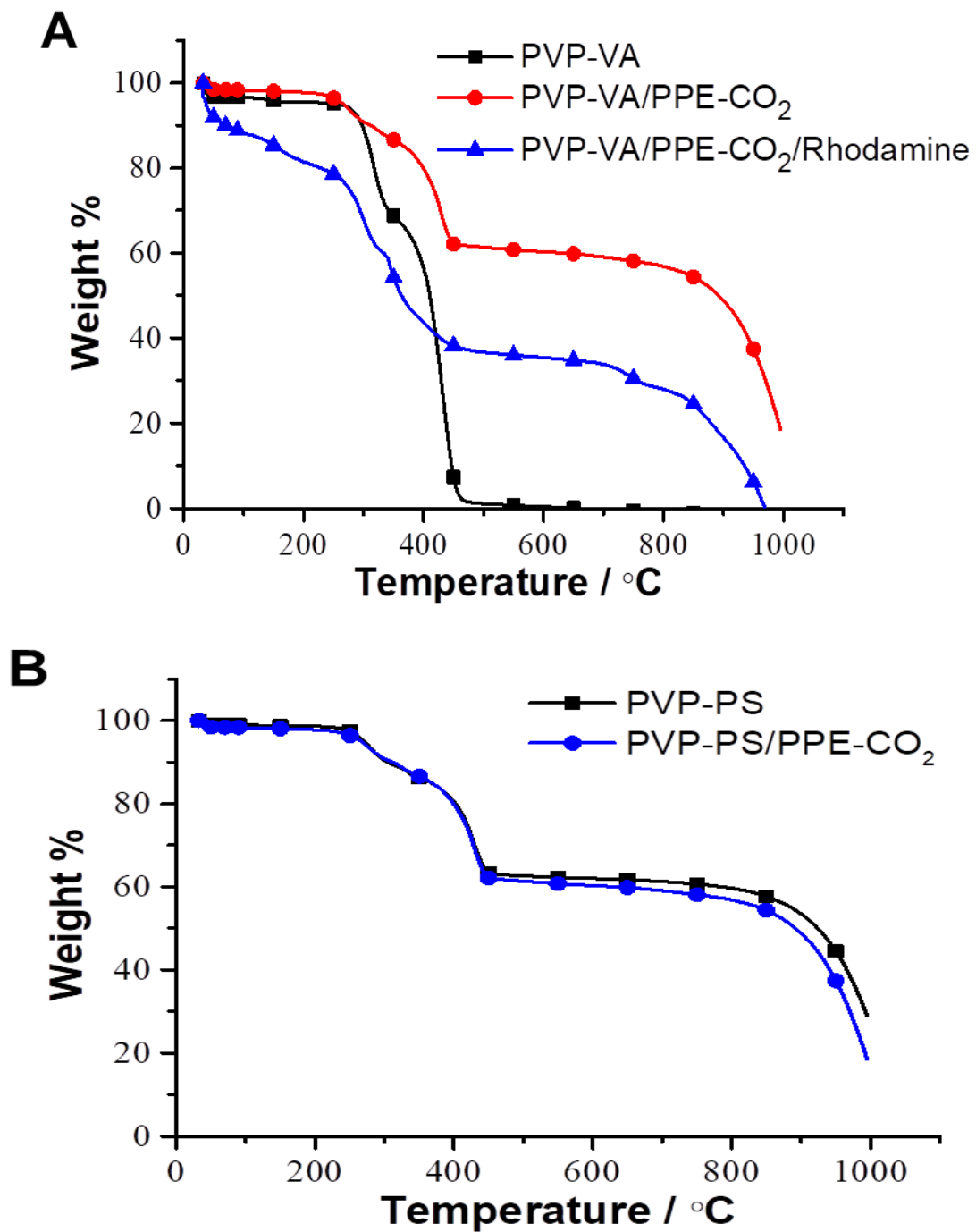


**Figure 4.13:** Thermogravimetric analysis for (A) PVP-VA, PVP-VA/ PPE-CO<sub>2</sub>-7, and PVP-VA/ PPE-CO<sub>2</sub>-7/Rhodamine B and (B) PVP-PS, PS/PPE-CO<sub>2</sub>-7

## 4.5 Conclusion

The thermal sensing challenge in thin films was approached mostly by developing optical films that change colors in response to external temperature stimulation. While these methods provide a great way to estimate the temperature of the film, they are limited to the depth of information they can provide. In this work, we show that thermochromic response of PPE-CO<sub>2</sub>-7 conjugated polyelectrolytes in solution is not restricted to PVP but is also observed with PVP co-polymers with a measured relative sensitivity of 2.35 % and 1.455 % for PVP-VA and PVP-PS, respectively. The thermal response was preserved in films but with no detectable ratiometric change in their signal, yet when mixed with Rhodamine B, the desired ratiometric signal was detected and was measured using a DSLR camera. This work has the potential to allow the measurements of thermal fluctuations in microelectronic devices such as MEMS, hence leading to the optimization of their performance.

## CHAPTER 5

### MAGNETIC RESPONSIVE AGAROSE NANOPARTICLES AS POTENTIAL VEHICLES FOR CONTROLLED CURCUMIN RELEASE

#### 5.1 Introduction

Employing effective treatment for diseases has been a major interest and an active field, during this period researchers have worked on developing greatly their understanding of human body nature and the role of its various components[39, 102]. The interest in having controlled systems that would release its cargo under specific stimuli and on a specific area was first proposed a century ago by Paul Ehrlich calling them magic bullets[103]. Since then a lot of efforts and progress have been made to develop this field and to broaden the scope of targeted delivery. Where seeking a drug delivery system for proper targeting specific sites in the body with minimizing delivery to off-target tissues is of extreme importance for successful therapy[104]. The demand for more efficient therapeutics and medication became an insisting need. Consequently, considerable attention is driven towards the development, design, and synthesis of controlled drug delivery systems.

Various nanocarriers have been used to increase the preferential accumulation of drug in tumors and control over drug bio-distribution and release [105]. These include polymer-drug conjugates, dendrimers nanogels[106] metal nanoparticles[107], mesoporous silica nanoparticles[108], virus-like particles[107], lipid nanoparticles[109], and polymeric nanoparticles[110].

Hydrogels in particular appeared to be an appealing vehicle for drug delivery. Mainly they are composed of 70-99% of water which makes them physically similar to tissues and gives them excellent biocompatibility[111]. Furthermore, their tunable mechanical stiffness made them an interesting candidate for drug delivery[112]. Their cross-linked network hinders the penetration of various proteins, and protect bioactive therapeutics from enzymatic degradation. These hydrogels appeared in the literature for the first time in 1894 and were first introduced to the biological field by Wichterle and Lim in 1960[113]. Since then further development has been implemented and smart hydrogels have been introduced and utilized in different fields of biological science, such as drug delivery[111], and tissue engineering[114].

Recently, injectable magnetic hydrogels have been introduced, this type of smart hydrogels, respond directly to any external magnetic field. Magnetic hydrogels have been reported with different magnetic nanoparticles (MNPs) such as -  $\gamma$ - $\text{Fe}_2\text{O}_3$ ,  $\text{Fe}_3\text{O}_4$ , cobalt ferrite ( $\text{CoFe}_2\text{O}_4$ ), strontium ferrite ( $\text{SrFeO}_{19}$ ) [115, 116]and so on. However,  $\text{Fe}_3\text{O}_4$  stands out of the crowd and is considered a robust candidate used in controlled drug delivery due to their abundance, super-paramagnetic and responsive properties.

The magnetic behavior of the magnetic hydrogels allows them to be used in magnetic resonance imaging (MRI), which is currently one of the most popular and widely used medical imaging techniques. It also allows them to be guided and held in a desired location by magnetic fields and to induce local heating in tumor regions by magnetic fluid hyperthermia[117]. This can be used to trigger the release of a loaded drug or to cause cell death by temperature-induced apoptosis and provide magnetic resonance imaging at the same time. Consequently, this represents a breakthrough in disease therapy and makes magnetic hydrogels excellent candidates for several biomedical applications

Herein, we report the successful development of a novel temperature-triggered curcumin release nanosystem.

Below we report our preliminary results on the topic.

## 5.2 Results and Discussion

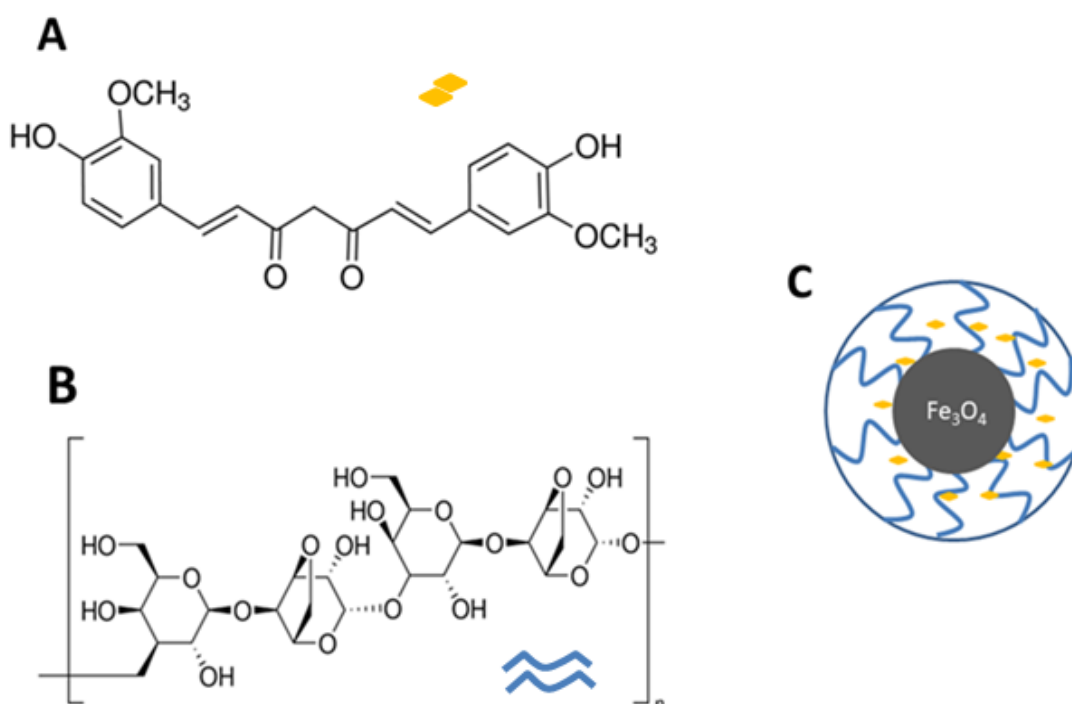


**Figure 5.1:** Chemical structures of (A) Curcumin, (B) Agarose, and (C) schematic representation of Curcumin-Agarose-MNP complex

### 5.2.1 Dynamic Light Scattering (DLS)

Drug Carriers with appropriate size plays a crucial role in the field of drug delivery. Several studies have reported that the cellular uptake efficiency of NPs decreases when increasing the particle size due to the reduction in surface area. It is stated that NPs in the range of nanometers have the highest potential to extend circulation time in the bloodstream.

The DLS results show that the drug carries are in the nano size (Table 5.1) with narrow polydispersity index which indicate the uniformity of the nanocarriers.

<b>Sample</b>	<b>Size (nm)</b>	<b>Polydispersity Index</b>
Agarose-Curcumin-MNP	764	0.389

**Table 5.1:** Hydrodynamic radius for the prepared particles Agarose-Curcumin-MNP measured using NanoPlus HD.

### 5.2.2 *Thermogravimetric Analysis (TGA)*

TGA was carried out to confirm the coating on the surface of the IONPs and estimate the relative composition of the agarose and curcumin, using the thermogravimetric analysis instrument: Netzsch TG 209 F1 Libra. The samples were first dried overnight and then analyzed between 30 °C and 1100 °C at a heating rate of 10.0 °C/ min. Figure 5.2 shows TGA thermal curves of agarose, curcumin-agarose, and curcumin-agarose-MNP. In which the mass of a substance is monitored as a function of temperature.

The results of the iron oxide-curcumin coated agarose nanoparticles sample revealed a one-step weight loss between 200 °C and 400 °C. This weight loss is attributed to the decomposition of agarose and curcumin. At 400 °C the ~70 % of the sample is decomposed which indicate that 70 % of agarose and curcumin is on the MNP surface. After 400 °C there was no weight change, implying the presence of iron oxide only. Thus, it could be concluded that the thermo-responsive polymer-curcumin-coated iron oxide nanoparticles consist of ~30 % MNPs.

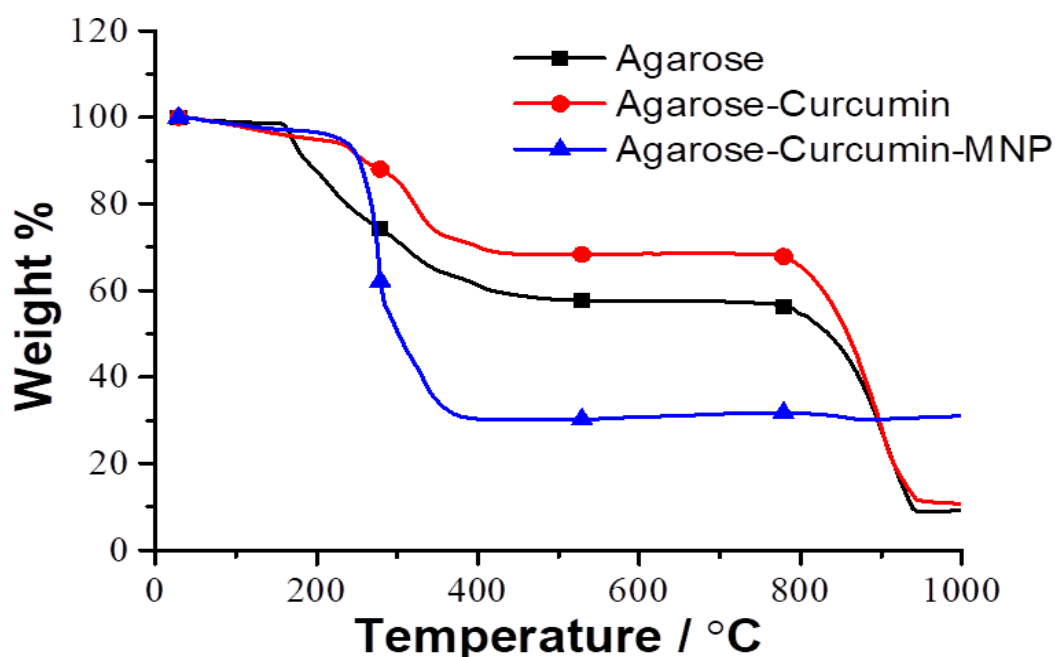


**Figure 5.2.:** Thermogravimetric analysis for Agarose, Agarose-Curcumin, and Agarose-Curcumin-MNP.

### 5.2.3 Curcumin loading and release evaluation

Curcumin was directly added to the agarose solution for the formation of drug-loaded agarose nanoparticles followed by the addition of MNP. Encapsulation efficiency (99 %) is calculated indirectly by measuring the amount of drug in the supernatant by a Steady State Fluorescent Spectroscopy (Figure 5.3A).

Curcumin drug released from the 1.5 mL of sample was determined in ethanol at RT and 45 °C. Released Curcumin was determined using a Steady State Fluorescent Spectroscopy at a wavelength of 420 nm. A standard calibration curve of known amounts of Curcumin was used to quantify the amounts of loaded and released (Figure 5.3B).



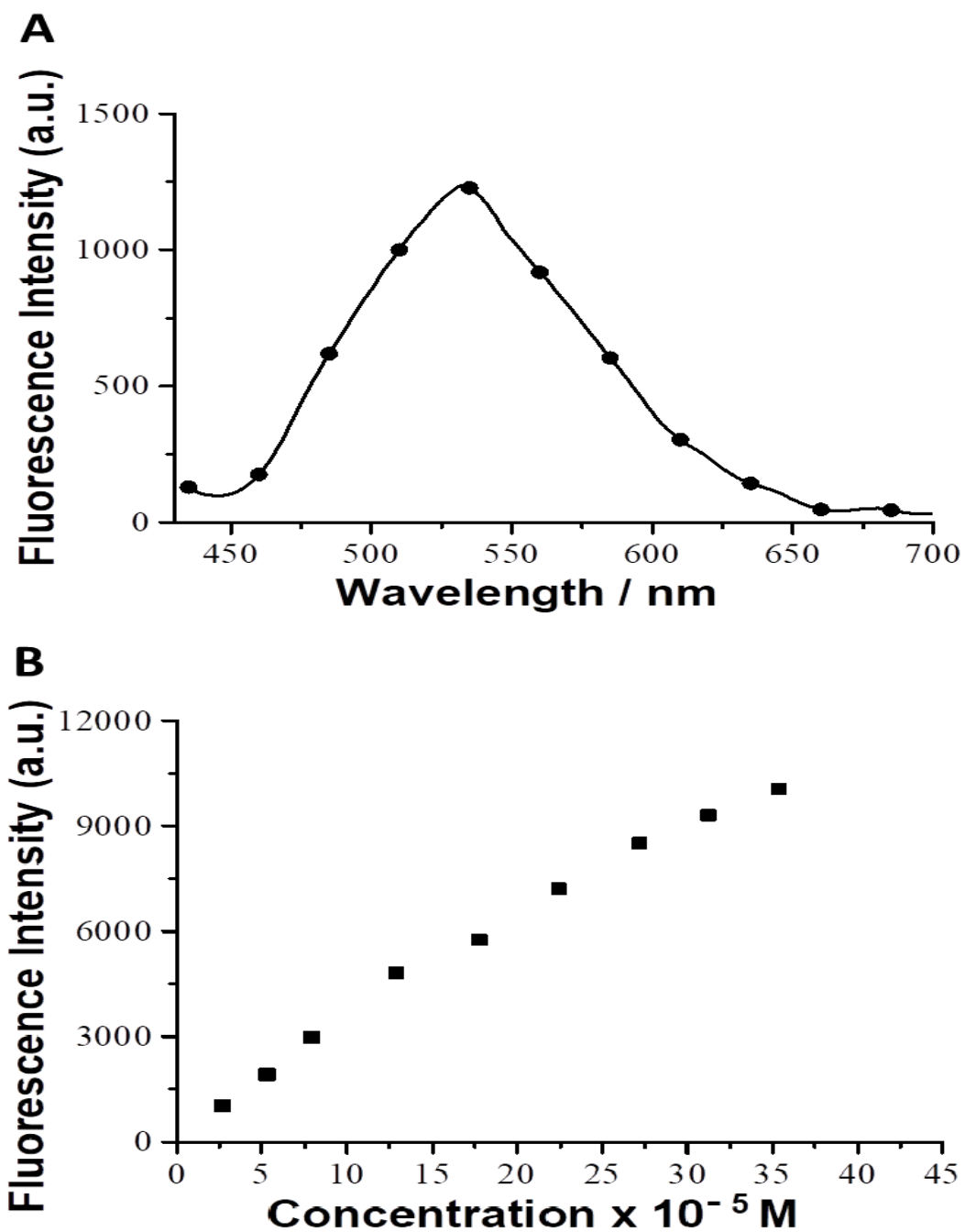


**Figure 5.3:** (A) Fluorescent emission spectra of free curcumin remained in supernatant at 20.0 °C. (B) Calibration curve obtained for calculating the amount of Curcumin loaded and released With  $R^2 = 0.982$  and  $y = 265.35x + 848$ . The emission spectra were acquired in ethanol after excitation at 420 nm. The lines connecting the experimental points are for visual aid.

#### **5.2.4 *Heating by induction versus heating in waterbath***

Drug release from biodegradable polymeric particles occurs through a combination of several mechanisms. It generally occurs through desorption of surface-bound drug, diffusion of the drug through the polymer matrix, and erosion of the polymer particles.

We found that the release was about 4.4 % for curcumin-loaded nanoparticles, which occurred within the first hour after increasing the temperature to 45 °C. No initial burst release suggests low drug density at the surface of the carriers. The rate of drug release increased steeply after temperature increased to 70 °C (Figure 5.4), which is close to the agarose melting temperature. The temperature was monitored and tracked using a thermocouple dipped inside the solution and connected to a Multi-meter.

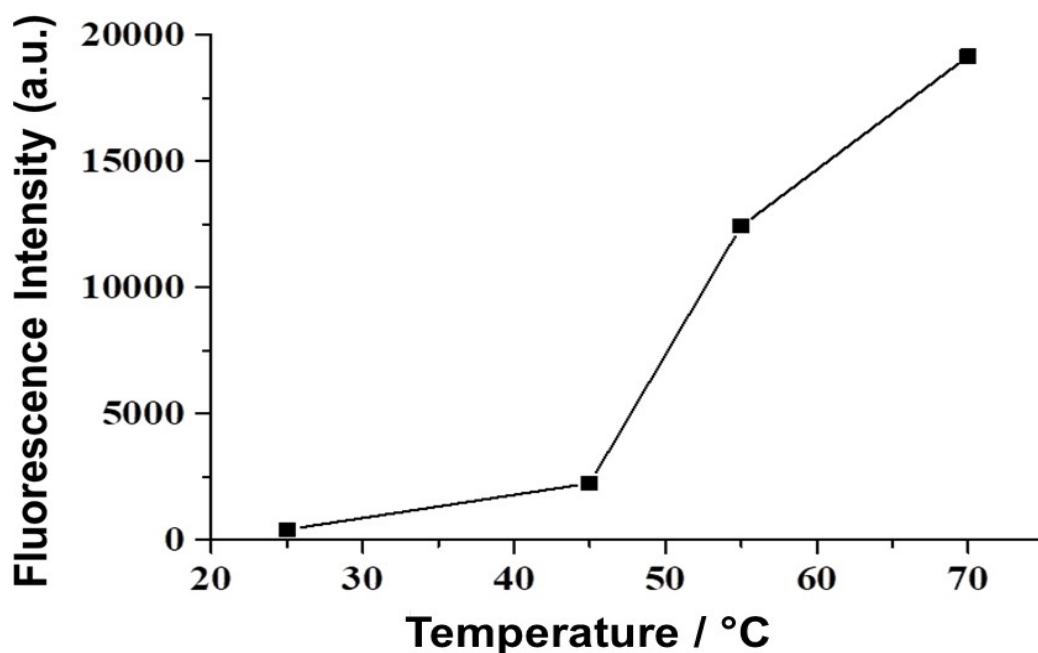


**Figure 5.4:** The release of curcumin form magnetic agarose after being exposed to an external magnetic field. The emission spectra were acquired in ethanol after excitation at 420 nm. The lines connecting the experimental points are for visual aid.

The efficiency of drug release when heated using induction was determined by the enhancement of fluorescence intensity of curcumin this experiment was repeated in triplicates for consistency.

To determine the efficiency of heating by induction we performed control experiments, where we heat the sample in a water bath under the same experimental conditions (figure 5.5). The fluorescence intensity of the optimized solution in both heating methods was measured at RT and 45 °C (Figure 5.5)

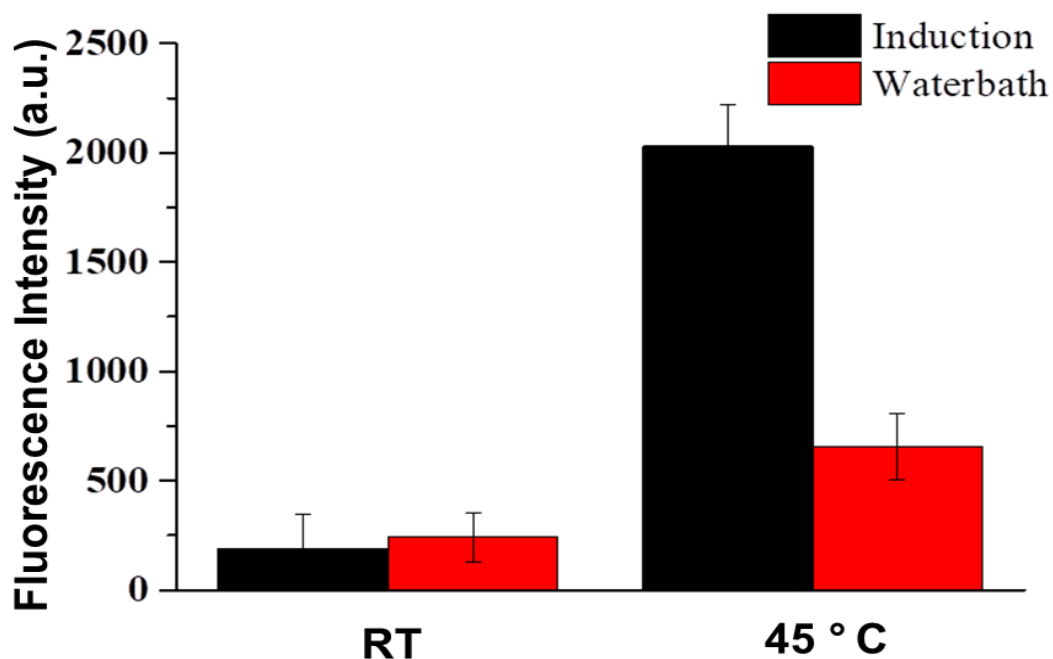


**Figure 5.5:** Comparison between the fluorescence intensities of curcumin released when heated by induction and in waterbath. The histograms represent the average fluorescent value of 3 independent trials at RT and 45 °C. Error bars were calculated from the standard deviations of the 3 independent measurements. The emission spectra were acquired in ethanol after excitation at 420 nm.

The control sample results allowed us to speculate that the local surface temperature of the MNP is higher than the solution temperature, allowing a more efficient curcumin release in case of heating by induction.

It is generally assumed that significant heating occurs only in the very close vicinity of the MNP surface. Several works have reported that, even if no macroscopic temperature changes under AMF are recorded, the local temperature at the nanoparticle surface is much higher from that of the macroenvironment, which in turn will help in degrading the drug carrier network without affecting the surrounding cells, tissues, and organs. This hypothesis is supported by a previously reported study; Pellegrino *et al.* probed the distance-dependent temperature as generated by magnetic nanoparticles using

a thermos-sensitive molecule. The local temperature surrounding the MNPs was found to be approximately 45 °C greater than the solution temperature [118], also the MNP vibrations might play a role in curcumin release. We also speculate that the release of curcumin from the magnetic agarose polymeric network is not only governed by the conversion of the dissipated magnetic energy into thermal energy but also the MNPs movements within the network might affect the release. The MNPs tend to vibrate and flip back and forth under the influence of AM, thus they might be mechanically deforming the polymeric network. As a result the mesh size might be increasing, which facilitates the curcumin diffusion within the network.

#### **5.2.5 *Curcumin release using Higher MNP concentration***

To validate our hypothesis and study the effect of MNP vibrations we performed different set of experiments. In the first set, we increased the amount of magnetic nanoparticles (Figure 5.6). After increasing the amount of MNP the drug release increased which suggest that MNPs are affecting the release of the encapsulated curcumin.

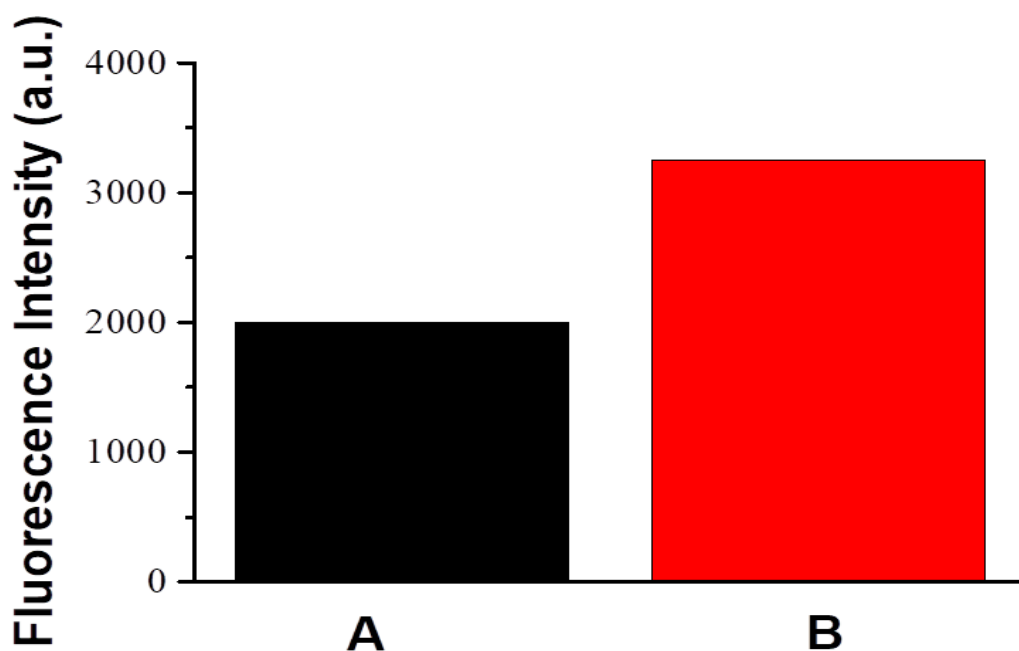


**Figure 5.6:** Comparison between the fluorescence intensities of curcumin released when different amount of MNPs (A) 0.2778 g/ mL and (B) 0.5556 g/ mL, upon heating by induction..The emission spectra were acquired in ethanol after excitation at 420 nm.

In the second set we run control experiments in water bath as such no MNPs vibrations induced change in the solution temperature .This experiment was done with a magnetic bar to mimic MNPs vibrations another control experiment was done without stirring. We assume that the magnetic bar stirring mimics the MNP vibrations. As such we believe that higher fluorescence intensity should be observed from the sample that is being stirred in case mechanical deformation is truly playing a role in the release.

The results show higher fluorescent intensity when the sample is being stirred compared to the sample without stirring (Figure 5.7). These observations indicate that the vibrations of MNPs under the influence of alternating magnetic field is indeed affecting the release.

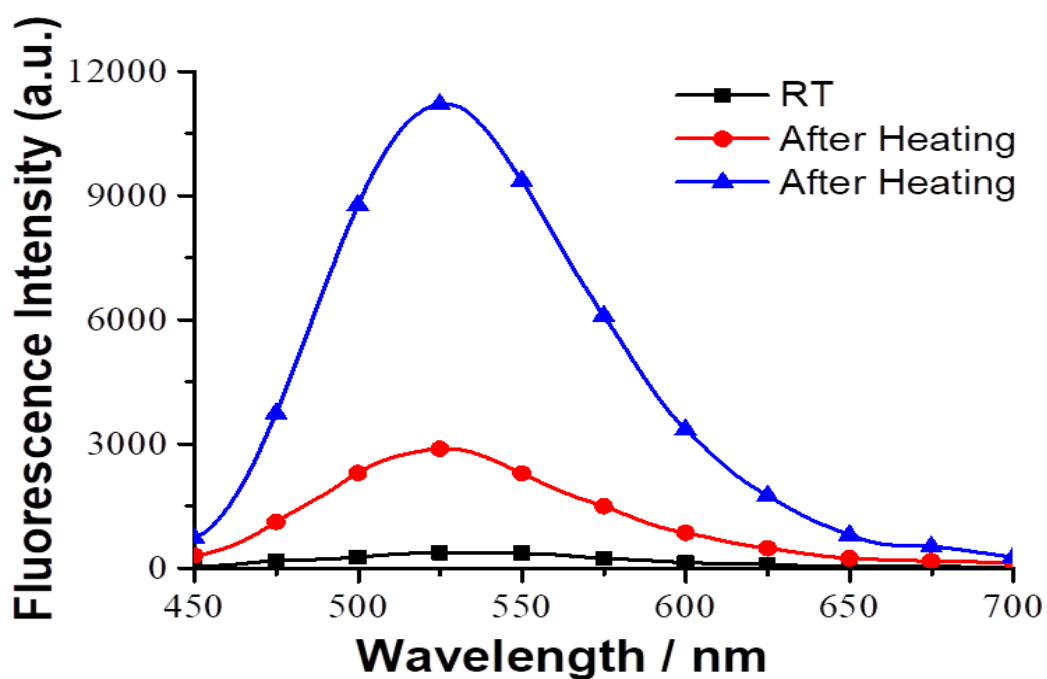


**Figure 5.7:** Emission spectra of maximum fluorescence intensities of curcumin released with stirring at 1150 rpm ( $\blacktriangle$ ) and without stirring ( $\bullet$ ). Measurements were done at room temperature and after heating in waterbath. Emission spectra were acquired upon excitation at 420 nm in ethanol.

### 5.2.6 *Microscopy Imaging*

Recent studies have reported that microscale devices can be used as a model of microcirculation to study and explore the targeting efficacy of polymeric nanoparticle and microparticle delivery vehicles in vitro [119]. Moreover, studying the release in microscale devices would achieve some level of spatial and temporal control over drug release.

These platforms have the ability to create local cellular microenvironment to closely mimic the physiological and pathological environments [120]. In addition, multiple cell types can be used inside them to create microscale platforms mimicking various-organ interactions, in which these systems allow the observation of a whole body response to drugs rather than the response of single cell lineages[121]. As a proof of concept and to visualize the release at the microscale level we decided to perform the below experiment. Thus, the magnetic curcumin nanocarriers were loaded to the 6  $\mu\text{M}$  microwell arrays, fluorescent images were then acquired before and after exposure to an alternating magnetic field, under the same conditions, and quantified based on their intensities (Figure 5.8A and 5.8B). The integrated intensity was obtained using ImageJ software. An enhancement in fluorescent intensity was obtained after exposing the microwells to an alternating magnetic field (Figure 5.8C), which indicates the release of the encapsulated curcumin.



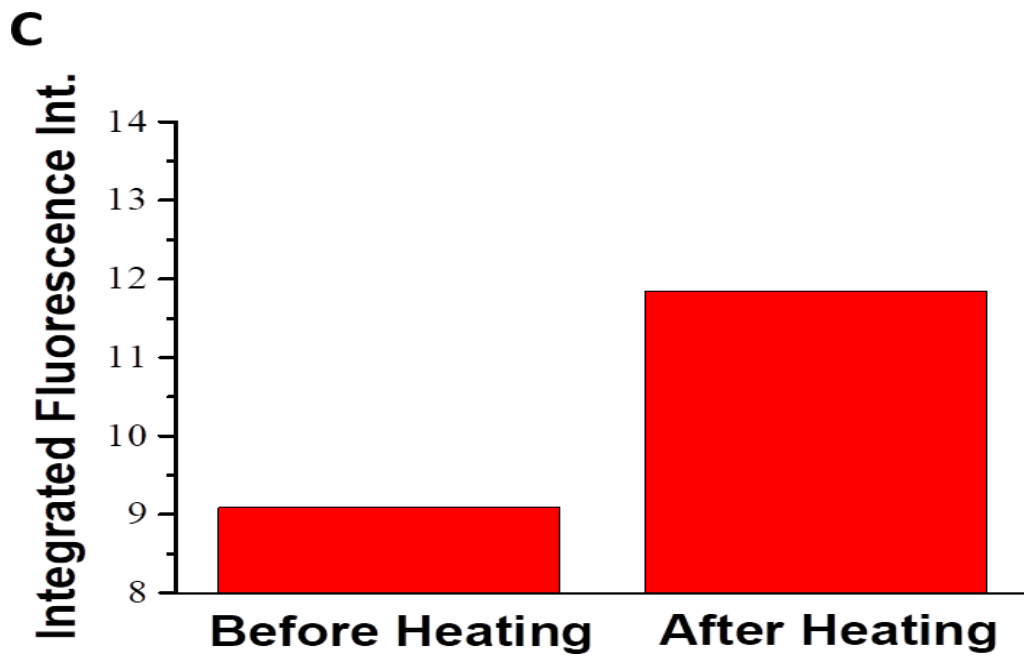
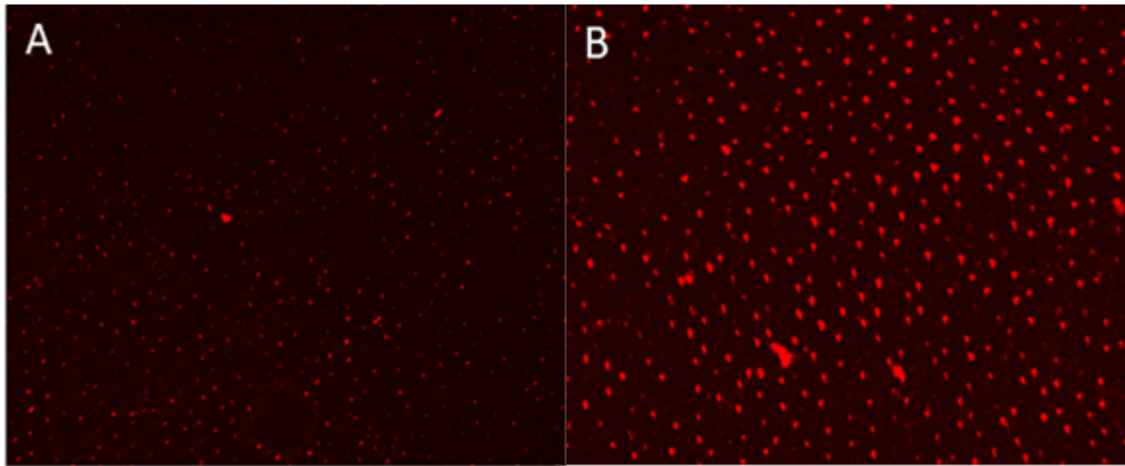


**Figure 5.8:** Fluorescent microscopy images of agarose gel before (A) and after (B) exposure to an alternating magnetic field (C) Integrated fluorescence intensity using ImageJ software before and after exposure to an alternating magnetic field.

### **5.3 Conclusion**

A controlled drug delivery system aids in releasing the correct dose of a therapeutic directly in the desired location and in a specific period of time. This allows maximizing the efficacy of the therapeutic and minimizing the possible side effects. Herein, we have developed a novel controlled nanoparticles-based drug delivery system for curcumin release, which enables high drug loading and regulated drug release. This approach shows clear advantages over conventional methods.

## CHAPTER 6

### CONCLUSION AND FUTURE WORK

In chapter 3, we report the development of a ratiometric thermal fluorescent probe based on the Förster resonance energy transfer between a lipid-embedded conjugated polyelectrolyte and a lyophilic acceptor dye. We showed that the Förster resonance energy transfer (FRET) pair is sensitive within the relevant physiological temperature window (20.0–50.0 °C). The signal was also shielded from an external pH and stable when cycled multiple times. The probe was also sensitive to the membrane composition and could, therefore, be further developed to probe the membrane composition and viscosity. Thermal mapping in biological membranes could unlock and help us understand many chemical and physical processes that do not only pertain to localized membrane phenomena but also extend to many other intra- and extracellular pathways.

In chapter 4, we report on poly (phenylene ethynylene) fluorescent-based conjugated polyelectrolyte capable of detecting thermal fluctuations in polymer films prepared from polyvinylpyrrolidone-co-vinyl acetate. The sensor was first optimized in solution by testing two polyvinylpyrrolidone (PVP) copolymers (co-vinyl acetate (VA) and co-polystyrene (PS)) before it was spun cast onto quartz slides and imaged using a DSLR camera at different temperatures. The images were analyzed and showed a change in color with the increase in temperature. When not illuminated, the polymer thin film is clear and transparent. Thermal sensing in thin films polymers has been a significant limitation towards optimizing the heat dissipation in micro- and nano-electronic devices as well as many other thin film-based technologies.

In chapter 5, a controlled drug delivery nanocarriers that would aid in releasing the correct dose of a therapeutic directly in the desired location and in a specific period of time was developed. In our system, we speculate that the drug is embedded in polymeric matrix and the local heating that happens after exposing the matrix to alternating magnetic field will loosen the polymeric matrix, with the aid of MNP vibrations.

For future prospective, we aim to optimize and characterize many important parameters, such as its size and shape, chemical structure; surface charge and biocompatibility. These features are among the key parameters that need to be determined and controlled to achieve the desired therapeutic behavior. Moreover, the experimental conditions in in vivo and in vitro studies are rarely controlled, thus it's crucial to study the release under the influence of different pHs. In addition the tumors microenvironment is significantly different from that in normal tissues, mainly it's acidic, and as such we aim to study the release at different pH to determine the carriers' stability and selectivity toward the targeted cells, tissues and organs. Consequently, we are going investigate the efficiency of cellular uptake of these nanoparticles and assess whether this delivery system can enhance the drug potency in impeding the growth of cancer cells compared to its free form.

## REFERENCES

1. Lucia, U., et al., *Constructal thermodynamics combined with infrared experiments to evaluate temperature differences in cells*. Sci Rep, 2015. **5**: p. 11587.
2. Stoward, P.J., *Thermodynamics of Biological Growth*. Nature, 1962. **194**(4832): p. 977-978.
3. Daniel, R., et al., *The effect of temperature on enzyme activity: New insights and their implications*. Extremophiles : life under extreme conditions, 2008. **12**: p. 51-9.
4. Podrabsky, J.E. and G.N. Somero, *Changes in gene expression associated with acclimation to constant temperatures and fluctuating daily temperatures in an annual killifish <i>Austrofundulus limnaeus</i>*. Journal of Experimental Biology, 2004. **207**(13): p. 2237.
5. Francis, D. and P.W. Barlow, *Temperature and the cell cycle*. Symp Soc Exp Biol, 1988. **42**: p. 181-201.
6. Ducommun, P., et al., *Monitoring temperature effects on cell metabolism in a packed bed process*. Biotechnology and bioengineering, 2002. **77**: p. 838-42.
7. Sokolov, K., *Nanotechnology: Tiny thermometers used in living cells*. Nature, 2013. **500**(7460): p. 36-7.
8. Homma, M., et al., *A ratiometric fluorescent molecular probe for visualization of mitochondrial temperature in living cells*. Chemical Communications, 2015. **51**(28): p. 6194-6197.
9. Jang, M., S.S. Kim, and J. Lee, *Cancer cell metabolism: implications for therapeutic targets*. Experimental & Molecular Medicine, 2013. **45**(10): p. e45-e45.
10. Arai, S., et al., *Mitochondria-targeted fluorescent thermometer monitors intracellular temperature gradient*. Chemical Communications, 2015. **51**(38): p. 8044-8047.
11. Xu, W., et al., *Discerning the Chemistry in Individual Organelles with Small-Molecule Fluorescent Probes*. Angewandte Chemie International Edition, 2016. **55**(44): p. 13658-13699.
12. Okabe, K., et al., *Intracellular temperature mapping with a fluorescent polymeric thermometer and fluorescence lifetime imaging microscopy*. Nature Communications, 2012. **3**(1): p. 705.
13. Zhao, Y. and Y. Qu, *Impact of Self-Heating Effect on Transistor Characterization and Reliability Issues in Sub-10 nm Technology Nodes*. IEEE Journal of the Electron Devices Society, 2019. **PP**: p. 1-1.
14. Cahill, D.G., et al., *Nanoscale thermal transport*. Journal of Applied Physics, 2002. **93**(2): p. 793-818.
15. Menges, F., et al., *Quantitative Thermometry of Nanoscale Hot Spots*. Nano Letters, 2012. **12**(2): p. 596-601.
16. Wang, X.-d., O.S. Wolfbeis, and R.J. Meier, *Luminescent probes and sensors for temperature*. Chemical Society Reviews, 2013. **42**(19): p. 7834-7869.
17. Brites, C.D.S., et al., *Thermometry at the nanoscale*. Nanoscale, 2012. **4**(16): p. 4799-4829.
18. Wu, Y., et al., *Ratiometric Nanothermometer Based on Rhodamine Dye-Incorporated F127-Melamine-Formaldehyde Polymer Nanoparticle: Preparation, Characterization, Wide-Range Temperature Sensing, and Precise Intracellular Thermometry*. ACS Appl Mater Interfaces, 2016. **8**(23): p. 14396-405.
19. Kiyonaka, S., et al., *Genetically encoded fluorescent thermosensors visualize subcellular thermoregulation in living cells*. Nat Methods, 2013. **10**(12): p. 1232-8.

20. Oyama, K., et al., *Walking nanothermometers: Spatiotemporal temperature measurement of transported acidic organelles in single living cells*. Lab on a chip, 2012. **12**: p. 1591-3.
21. Albers, A.E., et al., *Dual-emitting quantum dot/quantum rod-based nanothermometers with enhanced response and sensitivity in live cells*. J Am Chem Soc, 2012. **134**(23): p. 9565-8.
22. Unnikrishnan, B., et al., *Fluorescent Carbon Dots for Selective Labeling of Subcellular Organelles*. ACS omega, 2020. **5**(20): p. 11248-11261.
23. Balabhadra, S., et al., *Boosting the sensitivity of Nd<sup>3+</sup>-based luminescent nanothermometers*. Nanoscale, 2015. **7**(41): p. 17261-17267.
24. Takei, Y., et al., *A nanoparticle-based ratiometric and self-calibrated fluorescent thermometer for single living cells*. ACS Nano, 2014. **8**(1): p. 198-206.
25. Gota, C., et al., *Hydrophilic fluorescent nanogel thermometer for intracellular thermometry*. J Am Chem Soc, 2009. **131**(8): p. 2766-7.
26. Hayden, S. and T. Munro, *Fluorescent scanning thermal microscope based on a Blu-ray optical head to measure thermal diffusivity of radioactive samples*. Review of Scientific Instruments, 2019. **90**(2): p. 024903.
27. Vetrone, F., et al., *Temperature Sensing Using Fluorescent Nanothermometers*. ACS Nano, 2010. **4**(6): p. 3254-3258.
28. Benayas, A., E. Escuder, and D. Jaque, *High-resolution confocal fluorescence thermal imaging of tightly pumped microchip Nd:YAG laser ceramics*. Applied Physics B, 2012. **107**(3): p. 697-701.
29. Baffou, G., et al., *Temperature mapping near plasmonic nanostructures using fluorescence polarization anisotropy*. Opt Express, 2009. **17**(5): p. 3291-8.
30. Pelosse, M., et al., *Genetically Encoded Fluorescent Biosensors to Explore AMPK Signaling and Energy Metabolism*. Exp Suppl, 2016. **107**: p. 491-523.
31. Kolossov, V.L., et al., *Development of a high-dynamic range, GFP-based FRET probe sensitive to oxidative microenvironments*. Exp Biol Med (Maywood), 2011. **236**(6): p. 681-91.
32. Chen, C.-Y. and C.-T. Chen, *A PNIPAM-based fluorescent nanothermometer with ratiometric readout*. Chemical Communications, 2011. **47**(3): p. 994-996.
33. Ye, F., et al., *Ratiometric Temperature Sensing with Semiconducting Polymer Dots*. Journal of the American Chemical Society, 2011. **133**(21): p. 8146-8149.
34. Sakaguchi, R., S. Kiyonaka, and Y. Mori, *Fluorescent sensors reveal subcellular thermal changes*. Curr Opin Biotechnol, 2015. **31**: p. 57-64.
35. Jaque, D., et al., *Fluorescent nanothermometers for intracellular thermal sensing*. Nanomedicine (Lond), 2014. **9**(7): p. 1047-62.
36. Lee, W., J.H. Seo, and H.Y. Woo, *Conjugated polyelectrolytes: A new class of semiconducting material for organic electronic devices*. Polymer, 2013. **54**(19): p. 5104-5121.
37. Ding, D., et al., *Hyperbranched conjugated polyelectrolyte for dual-modality fluorescence and magnetic resonance cancer imaging*. Small, 2012. **8**(22): p. 3523-30.
38. Wu, C., et al., *Multicolor Conjugated Polymer Dots for Biological Fluorescence Imaging*. ACS Nano, 2008. **2**(11): p. 2415-2423.
39. Abou Matar, T. and P. Karam, *The Role of Hydrophobicity in the Cellular Uptake of Negatively Charged Macromolecules*. Macromolecular Bioscience, 2018. **18**(2): p. 1700309.
40. Liu, Y., K. Ogawa, and K.S. Schanze, *Conjugated polyelectrolytes as fluorescent sensors*. Journal of Photochemistry and Photobiology C: Photochemistry Reviews, 2009. **10**(4): p. 173-190.

41. Kumpumbu-Kalembe, L. and M. Leclerc, *Electrochemical characterization of monolayers of a biotinylated polythiophene: towards the development of polymeric biosensors*. Chemical Communications, 2000(19): p. 1847-1848.
42. Okabe, K., et al., *Intracellular thermometry with fluorescent sensors for thermal biology*. Pflugers Archiv : European journal of physiology, 2018. **470**(5): p. 717-731.
43. Hegyi, G., G.P. Szigeti, and A. Szász, *Hyperthermia versus Oncothermia: Cellular Effects in Complementary Cancer Therapy*. Evid Based Complement Alternat Med, 2013. **2013**: p. 672873.
44. Karimi, M., et al., *Smart micro/nanoparticles in stimulus-responsive drug/gene delivery systems*. Chemical Society reviews, 2016. **45**(5): p. 1457-1501.
45. Jeong, B., S.W. Kim, and Y.H. Bae, *Thermosensitive sol-gel reversible hydrogels*. Adv Drug Deliv Rev, 2002. **54**(1): p. 37-51.
46. Zhao, X., H. Jiang, and K.S. Schanze, *Polymer Chain Length Dependence of Amplified Fluorescence Quenching in Conjugated Polyelectrolytes*. Macromolecules, 2008. **41**(10): p. 3422-3428.
47. Somero, G.N., *Proteins and temperature*. Annu Rev Physiol, 1995. **57**: p. 43-68.
48. Uchiyama, S., et al., *Intracellular temperature measurements with fluorescent polymeric thermometers*. Chemical Communications, 2017. **53**(80): p. 10976-10992.
49. Tanimoto, R., et al., *Detection of Temperature Difference in Neuronal Cells*. Scientific Reports, 2016. **6**(1): p. 22071.
50. Murata, N. and D.A. Los, *Membrane Fluidity and Temperature Perception*. Plant physiology, 1997. **115**(3): p. 875-879.
51. Quinn, P.J., *A lipid-phase separation model of low-temperature damage to biological membranes*. Cryobiology, 1985. **22**(2): p. 128-46.
52. Antonov, V.F., et al., *The appearance of single-ion channels in unmodified lipid bilayer membranes at the phase transition temperature*. Nature, 1980. **283**(5747): p. 585-586.
53. Wolfbeis, O.S., *Fiber-optic chemical sensors and biosensors*. Anal Chem, 2008. **80**(12): p. 4269-83.
54. Nikoleli, G.-P., et al., *Lipid Membrane Nanosensors for Environmental Monitoring: The Art, the Opportunities, and the Challenges*. Sensors (Basel, Switzerland), 2018. **18**(1): p. 284.
55. McQuade, D.T., A.E. Pullen, and T.M. Swager, *Conjugated Polymer-Based Chemical Sensors*. Chemical Reviews, 2000. **100**(7): p. 2537-2574.
56. Smith, A., et al., *Ionic strength and solvent control over the physical structure, electronic properties and superquenching of conjugated polyelectrolytes*. Research on Chemical Intermediates, 2007. **33**: p. 125-142.
57. Karam, P., et al., *Unraveling electronic energy transfer in single conjugated polyelectrolytes encapsulated in lipid vesicles*. Proc Natl Acad Sci U S A, 2010. **107**(41): p. 17480-5.
58. Karam, P., et al., *Interaction of Anionic Phenylene Ethynylene Polymers with Lipids: From Membrane Embedding to Liposome Fusion*. Langmuir, 2014. **30**(35): p. 10704-10711.
59. Ding, L., et al., *Insight into the Mechanism of Antimicrobial Conjugated Polyelectrolytes: Lipid Headgroup Charge and Membrane Fluidity Effects*. Langmuir, 2010. **26**(8): p. 5544-5550.
60. Ngo, A.T. and G. Cosa, *Assembly of Zwitterionic Phospholipid/Conjugated Polyelectrolyte Complexes: Structure and Photophysical Properties*. Langmuir, 2010. **26**(9): p. 6746-6754.
61. Chen, L., et al., *Tuning the Properties of Conjugated Polyelectrolytes through Surfactant Complexation*. Journal of the American Chemical Society, 2000. **122**(38): p. 9302-9303.
62. Wang, Y., et al., *Direct Visualization of Bactericidal Action of Cationic Conjugated Polyelectrolytes and Oligomers*. Langmuir, 2012. **28**(1): p. 65-70.

63. Wang, Y., et al., *Understanding the Dark and Light-Enhanced Bactericidal Action of Cationic Conjugated Polyelectrolytes and Oligomers*. Langmuir : the ACS journal of surfaces and colloids, 2012. **29**.
64. Corbitt, T.S., et al., *Conjugated polyelectrolyte capsules: light-activated antimicrobial micro "Roach Motels"*. ACS Appl Mater Interfaces, 2009. **1**(1): p. 48-52.
65. González, C.M., et al., *Artificial biomembrane based on DPPC — Investigation into phase transition and thermal behavior through ellipsometric techniques*. Biochimica et Biophysica Acta (BBA) - Biomembranes, 2015. **1848**(10, Part A): p. 2295-2307.
66. Leonenko, Z., et al., *Investigation of temperature-induced phase transitions in DOPC and DPPC phospholipid bilayers using temperature-controlled scanning force microscopy*. Biophysical journal, 2004. **86**(6): p. 3783-3793.
67. Wang, M., et al., *The effect of temperature on supported dipalmitoylphosphatidylcholine (DPPC) bilayers: structure and lubrication performance*. J Colloid Interface Sci, 2015. **445**: p. 84-92.
68. Wu, Y., et al., *Molecular rheometry: direct determination of viscosity in Lo and Ld lipid phases via fluorescence lifetime imaging*. Physical Chemistry Chemical Physics, 2013. **15**(36): p. 14986-14993.
69. Zadrán, S., et al., *Fluorescence resonance energy transfer (FRET)-based biosensors: visualizing cellular dynamics and bioenergetics*. Appl Microbiol Biotechnol, 2012. **96**(4): p. 895-902.
70. Casares, D., P.V. Escribá, and C.A. Rosselló, *Membrane Lipid Composition: Effect on Membrane and Organelle Structure, Function and Compartmentalization and Therapeutic Avenues*. International journal of molecular sciences, 2019. **20**(9): p. 2167.
71. Redondo-Morata, L., M.I. Giannotti, and F. Sanz, *Influence of cholesterol on the phase transition of lipid bilayers: a temperature-controlled force spectroscopy study*. Langmuir : the ACS journal of surfaces and colloids, 2012. **28**(35): p. 12851-12860.
72. Kuzu, O.F., M.A. Noory, and G.P. Robertson, *The Role of Cholesterol in Cancer*. Cancer research, 2016. **76**(8): p. 2063-2070.
73. Yang, S.-T., et al., *The role of cholesterol in membrane fusion*. Chemistry and physics of lipids, 2016. **199**: p. 136-143.
74. Jeong, W., et al., *Accurate, hysteresis-free temperature sensor for health monitoring using a magnetic sensor and pristine polymer*. RSC Advances, 2019. **9**(14): p. 7885-7889.
75. Darwish, G.H., et al., *Turning the heat on conjugated polyelectrolytes: an off-on ratiometric nanothermometer*. Chemical Communications, 2016. **52**(4): p. 823-826.
76. Donner, J.S., et al., *Mapping Intracellular Temperature Using Green Fluorescent Protein*. Nano Letters, 2012. **12**(4): p. 2107-2111.
77. Mailly, F., et al., *Anemometer with hot platinum thin film*. Sensors and Actuators A: Physical, 2001. **94**(1): p. 32-38.
78. Dai, C.-L., *A Capacitive Humidity Sensor Integrated with Micro Heater and Ring Oscillator Circuit Fabricated by CMOS-MEMS Technique*. Sensors and Actuators B: Chemical, 2007. **122**: p. 375-380.
79. Hwang, W.-J., et al., *Development of micro-heaters with optimized temperature compensation design for gas sensors*. Sensors (Basel, Switzerland), 2011. **11**(3): p. 2580-2591.
80. Donner, J.S., et al., *Mapping intracellular temperature using green fluorescent protein*. Nano Lett, 2012. **12**(4): p. 2107-11.
81. Aslam, M., C. Gregory, and J.V. Hatfield, *Polyimide Membrane for Micro-heated Gas Sensor Array*. Sensors and Actuators B: Chemical, 2004. **103**: p. 153-157.
82. Tao, C., et al., *Thermal analysis and design of a micro-hotplate for Si-substrated micro-structural gas sensor*. 2008 3rd IEEE International Conference on Nano/Micro Engineered and Molecular Systems, 2008: p. 284-287.



83. Fürjes, P., et al., *Thermal investigation of micro-filament heaters*. Sensors and Actuators A: Physical, 2002. **99**(1): p. 98-103.
84. Creemer, J.F., et al., *Microhotplates with TiN heaters*. Sensors and Actuators A: Physical, 2008. **148**(2): p. 416-421.
85. Verhoeven, H., et al., *Thermal resistance and electrical insulation of thin low-temperature-deposited diamond films*. Diamond and Related Materials, 1997. **6**(2): p. 298-302.
86. Khandurina, J., et al., *Integrated system for rapid PCR-based DNA analysis in microfluidic devices*. Anal Chem, 2000. **72**(13): p. 2995-3000.
87. Lagally, E.T., I. Medintz, and R.A. Mathies, *Single-Molecule DNA Amplification and Analysis in an Integrated Microfluidic Device*. Analytical Chemistry, 2001. **73**(3): p. 565-570.
88. Darwish, G.H., et al., *Turning the heat on conjugated polyelectrolytes: an off-on ratiometric nanothermometer*. Chemical Communications, 2016. **52**(4): p. 823-826.
89. Schirhagl, R., K. Ren, and R.N. Zare, *Surface-imprinted polymers in microfluidic devices*. Science China Chemistry, 2012. **55**(4): p. 469-483.
90. Sarma, S., S. Kar, and N. Sahoo, *THIN FILM TEMPERATURE SENSORS FOR TRANSIENT MEASUREMENT*. 2013.
91. He, S., M.M. Mench, and S. Tadigadapa, *Thin film temperature sensor for real-time measurement of electrolyte temperature in a polymer electrolyte fuel cell*. Sensors and Actuators A: Physical, 2006. **125**(2): p. 170-177.
92. Kano, Y., et al., *Fluorescence Thermo-Sensor Sheet Using Cr Doped YAlO<sub>3</sub> Crystals*. 2006. 1660-1663.
93. Gui, L. and C. Ren, *Temperature Measurement in Microfluidic Systems Using Photobleaching of a Fluorescent Slab*. Applied Physics Letters, 2008. **92**: p. 024102-024102.
94. Jiang, H., et al., *Conjugated polyelectrolytes: synthesis, photophysics, and applications*. Angew Chem Int Ed Engl, 2009. **48**(24): p. 4300-16.
95. Beljonne, D., et al., *Interchain vs. intrachain energy transfer in acceptor-capped conjugated polymers*. Proceedings of the National Academy of Sciences, 2002. **99**(17): p. 10982.
96. Hennebicq, E., et al., *Exciton migration in rigid-rod conjugated polymers: an improved Förster model*. J Am Chem Soc, 2005. **127**(13): p. 4744-62.
97. Al Attar, H.A. and A.P. Monkman, *Effect of Surfactant on Water-Soluble Conjugated Polymer Used in Biosensor*. The Journal of Physical Chemistry B, 2007. **111**(43): p. 12418-12426.
98. Darwish, G.H. and P. Karam, *Nanohybrid conjugated polyelectrolytes: highly photostable and ultrabright nanoparticles*. Nanoscale, 2015. **7**(37): p. 15149-15158.
99. Darwish, G.H., J. Abouzeid, and P. Karam, *Tunable nanothermometer based on short poly(phenylene ethynylene)*. RSC Advances, 2016. **6**(71): p. 67002-67010.
100. Darwish, G.H., H.H. Fakhri, and P. Karam, *Temperature Mapping in Hydrogel Matrices Using Unmodified Digital Camera*. J PhysChem B, 2017. **121**(5): p. 1033-1040.
101. Hell, S.W. and J. Wichmann, *Breaking the diffraction resolution limit by stimulated emission: stimulated-emission-depletion fluorescence microscopy*. Opt Lett, 1994. **19**(11): p. 780-2.
102. How, C.W., et al., *Tamoxifen-loaded nanostructured lipid carrier as a drug delivery system: characterization, stability assessment and cytotoxicity*. Colloids Surf B Biointerfaces, 2013. **112**: p. 393-9.
103. Hsu, H.J., et al., *Dendrimer-based nanocarriers: a versatile platform for drug delivery*. Wiley Interdiscip Rev Nanomed Nanobiotechnol, 2017. **9**(1).
104. sharma, H., et al., *Metal nanoparticles: a theranostic nanotool against cancer*. Drug Discov Today, 2015. **20**(9): p. 1143-51

105. Chang, D., et al., *Biologically Targeted Magnetic Hyperthermia: Potential and Limitations*. *Frontiers in pharmacology*, 2018. **9**: p. 831-831.
106. Hörmann, K. and A. Zimmer, *Drug delivery and drug targeting with parenteral lipid nanoemulsions - A review*. *J Control Release*, 2016. **223**: p. 85-98.
107. Merino, S., et al., *Nanocomposite Hydrogels: 3D Polymer-Nanoparticle Synergies for On-Demand Drug Delivery*. *ACS Nano*, 2015. **9**(5): p. 4686-97.
108. Li, J. and D.J. Mooney, *Designing hydrogels for controlled drug delivery*. *Nature reviews. Materials*, 2016. **1**(12): p. 16071.
109. Calvert, P., *Hydrogels for Soft Machines*. *Advanced Materials*, 2009. **21**: p. 743-756.
110. Lee, S., I.K. Kwon, and K. Park, *Hydrogels for Delivery of Bioactive Agents: A Historical Perspective*. *Advanced drug delivery reviews*, 2012. **65**.
111. Lee, K.Y. and D.J. Mooney, *Hydrogels for tissue engineering*. *Chem Rev*, 2001. **101**(7): p. 1869-79.
112. Patwa, R., N. Saha, and P. Saha, *Magnetic hydrogel based shoe insoles for prevention of diabetic foot*. *Journal of Magnetism and Magnetic Materials*, 2020. **514**: p. 167153.
113. Li, D.-q., et al., *An injectable, self-healing hydrogel system from oxidized pectin/chitosan/ $\gamma$ -Fe<sub>2</sub>O<sub>3</sub>*. *International Journal of Biological Macromolecules*, 2020. **164**: p. 4566-4574.
114. Stephen, Z.R., F.M. Kievit, and M. Zhang, *Magnetite Nanoparticles for Medical MR Imaging*. *Materials today (Kidlington, England)*, 2011. **14**(7-8): p. 330-338.
115. Riedinger, A., et al., *Subnanometer local temperature probing and remotely controlled drug release based on azo-functionalized iron oxide nanoparticles*. *Nano Lett*, 2013. **13**(6): p. 2399-406.
116. Farokhzad, O.C., et al., *Microfluidic System for Studying the Interaction of Nanoparticles and Microparticles with Cells*. *Analytical Chemistry*, 2005. **77**(17): p. 5453-5459.
117. Qian, T. and Y. Wang, *Micro/nano-fabrication technologies for cell biology*. *Med Biol Eng Comput*, 2010. **48**(10): p. 1023-32.
118. Khamsi, R., *Labs on a chip: meet the stripped down rat*. *Nature*, 2005. **435**(7038): p. 12-3.

